UNIVERSITY OF ROCHESTER
LABORATORY FOR LASER ENERGETICS

Volume 169
October–December 2021
DOE/NA/3856-1700

LLE Review

Quarterly Report

About the Cover:

The high school students and teachers who participated in the 2021 Broad Exposure to Science and Technology (BEST) Research Program are shown engaging in various aspects of science and technology that support LLE's laser research program. They explored microscopy, spectroscopy, electronic technology, lasers, optical design, liquid crystals, and holography. The importance of continued STEM education in research, was emphasized by former LLE director, Mike Campbell, to highlight the extensive teamwork required to make advancements in laser development and scientific applications.

The BEST program was carried out at East High School within the Rochester City School District during the summer of 2021. The participants of the BEST program (shown left to right) include East High teachers Trent Russell and Gavin Jenkins, East High students Yusuf Gazali, Reganae Walters, Taiasia Gibson, and Ramir Wearen, and program coordinator Terry Kessler, LLE Diversity Manager.

LLE mentors exposed the BEST students and teachers to the key technologies that are central to the construction and operation of the OMEGA Laser System. Electronic circuits were explored by dissecting computer systems and practicing the microsoldering techniques. Lasers were brought into the classroom for demonstration and exhibition. Both interferometry and holography were experimentally explored to manufacture diffraction gratings and holographic 3-D images. In addition, liquid crystal materials were used to manufacture polarization optics and color-tuned paints. The philosophy that underpins the BEST program is that multiple early exposures help guide students in their pursuits of STEM fields and encourages them to explore the next generation of related jobs and careers.

I3113JR

The work described in this volume includes current research at the Laboratory for Laser Energetics, which is supported by New York State Energy Research and Development Authority, the University of Rochester, the U.S. Department of Energy Office of Inertial Confinement Fusion under Cooperative Agreement No. DE-NA0003856, and other agencies.

For questions or comments, contact Nickolaos Savidis, Editor, Laboratory for Laser Energetics, 250 East River Road, Rochester, NY 14623-1299, (585) 275-3413.

www.lle.rochester.edu

Printed in the United States of America
Available from
National Technical Information Services
U.S. Department of Commerce
5285 Port Royal Road
Springfield, VA 22161
www.ntis.gov

UNIVERSITY OF ROCHESTER
LABORATORY FOR LASER ENERGETICS

Volume 169
October–December 2021
DOE/NA/3856-1700

LLE Review

Quarterly Report

Contents

In Brief iii

Inertial Confinement Fusion

Bound on Hot-Spot Mix in High-Velocity, High-Adiabat Direct-Drive Cryogenic Implosions Based on Comparison of Absolute X-Ray and Neturon Yields 1

Mitigation of Deceleration-Phase Rayleigh–Taylor Growth in Inertial Confinement Fusion Implosions 5

Emission Phases of Implosion X-Ray Sources for Absorption Spectroscopy 9

Plasma and Ultrafast Physics

Underdense Relativistically Thermal Plasma Produced by Magnetically Assisted Direct Laser Acceleration 12

An Independent-Hot-Spot Approach to Multibeam Laser–Plasma Instabilities 16

High-Energy-Density Physics

Density Reconstruction in Convergent High-Energy-Density Systems Using X-Ray Radiography and Bayesian Inference 20

Diamond Formation in Double-Shocked Epoxy to 150 GPa 23

Meta-GGA Exchange-Correlation Free Energy Density Functional to Increase the Accuracy of Warm-Dense-Matter Simulations 26

Unveiling the Nature of the Bonded-to-Atomic Transition in Liquid SiO_2 to TPa Pressures 29

Diagnostic Science and Detectors

A Case Study of Using X-Ray Thomson Scattering to Diagnose the In-Flight Plasma Conditions of DT Cryogenic Implosions 31

Interdigitated Electrode Geometry Variation and External Quantum Efficiency of GaN/AlGaN-Based Metal–Semiconductor–Metal Ultraviolet Photodetectors 34

Laser Technology and Development

Impact of the Optical Parametric Amplification Phase on Laser Pulse Compression 37

Simultaneous Contrast Improvement and Temporal Compression Using Divided-Pulse Nonlinear Compression 40

Analysis of Pump-to-Signal Noise Transfer in Two-Stage Ultra-Broadband Optical Parametric Chirped-Pulse Amplification 43

Spectral and Temporal Shaping of Spectrally Incoherent Pulses in the Infrared and Ultraviolet 46

Effect of the Pump-Beam Profile and Wavefront on the Amplified Signal Wavefront in Optical Parametric Amplifiers 50

Materials Science

Evaluation of Transverse Raman Scattering in KDP and DKDP in Geometries Suitable for Beam Polarization Control 56

Education and Outreach

LLE BEST Student and Teacher Research Program: Broad Exposure to Science and Technology 58

Laser Facility

FY22 Q1 Laser Facility Report 63

Publications and Conference Presentations 65

In Brief

This volume of LLE Review 169 covers the period from October–December 2021. Articles appearing in this volume are the principal summarized results for long-form research articles. Readers seeking a more-detailed account of research activities are invited to seek out the primary materials appearing in print, detailed in the publications and presentations section at the end of this volume.

Highlights of research presented in this volume include:

- R. C. Shah *et al.* report on a new continuum x-ray measurement to characterize hot-spot x-ray yield and hot-spot electron temperature of a series of implosions typical of current best cryogenic designs, comparing x-ray production relative to neutron production and assessing the ratio of hot-spot mix (p. 1).
- Y. Lawrence *et al.* show lowering the central density by a factor of 5 or more compared to the vapor density of deuterium–tritium (DT) at triple point can aid in achieving small hot-spot size without excessive amplification of deceleration-phase Rayleigh–Taylor instability, possibly enabling ignition and high gains in laser-direct-drive designs using lower energies (p. 5).
- D. A. Chin *et al.* experimentally identify three x-ray phases consisting of the corona, core stagnation, and afterflow using temporal, spatial, and spectral x-ray emission of implosion glow-discharge polymerization shells on OMEGA EP (p. 9).
- K. Weichman *et al.* demonstrate that the generation of underdense, relativisitically thermal plasma can be realized with currently available laser and magnetic-field–generation capabilities by leveraging two regimes of magnetically assisted direct laser acceleration (p. 12).
- R. K. Follett *et al.* create an independent-hot-spot model to predict multibeam instability behavior (p. 16). The model is applied to the absolute two-plasmon–decay instability and is shown to provide an improved description of laser–plasma instability behavior over the common-wave approach.
- S. Ressel *et al.* present the full uncertainty distributions inferred from radiography analysis in high-energy-density systems (p. 20). They demonstrate the importance of a full treatment of uncertainties, done here through Bayesian analysis, which is critical to avoid overconfidence in parameter estimates in this system due to the correlations between parameters and multiple maxima in the likelihood function introduced by typical experimantal noise sources.
- M. C. Marshall *et al.* use data from two OMEGA EP experiments to demonstrate that the chemical and thermodynamic conditions inside ice giant planets, which have inner ice layers dominated by CH_4, NH_3, and H_2O, are suitable for diamond formation (p. 23).
- V. V. Karasiev, D. I. Mihaylov, and S. X. Hu address exchange-correlation (XC) dependence thermal modeling in density-functional-theory simulations of warm dense matter and high-energy-density plasma effects by developing a thermalization framework for XC functionals and XC additive correction at the GGA level, improving simulation accuracy and agreement to experimental results (p. 26).
- S. Zhang *et al.* perform simulations from first principles and analyzed the structure, electron density, and thermodynamic properties of liquid SiO_2 at high-energy conditions to gain insights into the nature of the bonded-to-atomic transition (p. 29).
- H. Poole *et al.* conduct a feasibility study of using spatially integrated, spectrally resolved, x-ray Thomson-scattering measurements to diagnose the temperature, density, and ionization of the compressed DT shell of a cryogenic DT implosion at two-thirds convergence for both low- and high-adiabat implosions (p. 31).

- S. F. Nwabunwanne and W. R. Donaldson discuss the design and fabrication of $Al_xGa_{1-x}N$-based photodetectors with rectangular and circular asymmetric, interdigitated electrode geometries GaN/AlGaN semiconductors with an interest in high-efficiency detectors targeting semiconductor-driven ultrafast laser pulse characterization and plasma diagnostics (p. 34).
- J. Musgrave and J. Bromage investigate signal phase accumulation from pump wavefront errors and the potential impact on signal pulse compression, offering an approach to determine the suitability of a given pump laser to ensure there are no spatiotemporal pulse-broadening effects that degrade the laser's peak intensity (p. 37).
- G. W. Jenkins, C. Feng, and J. Bromage demonstrate a new method of contrast improvement that allows both contrast improvement and temporal compression in a single step—divided-pulse nonlinear compression (p. 40).
- C. Feng *et al*. develop a simple and cost-effective tool to reduce pump-induced temporal contrast degradation up to 15 dB by applying a pump-seed delay optimization and pump-to-signal noise transfer of a two-stage ultra-broadband optical parametric chirped-pulse amplifier (p. 43).
- C. Dorrer and M. Spilatro demonstrate broadband, spectrally incoherent nanosecond pulses with closed-loop pulse shaping, inspired by laser–plasma instability mitigation and improving target to high-energy laser pulse interactions (p. 46).
- S.-W. Bahk *et al*. analyze the effect of the pump beam wavefront phase and amplitude transferred to the idler and signal beam phase and amplitude using the analytic optical parametric amplifier (OPA) phase solution, wave-vector picture, and experimentally measured OPA phase using the MTW-OPAL laser (p. 50).
- T. Z. Kosc *et al*. develop and experimentally validate a modeling capability to evaluate large-aperture optics, applicable for minimizing transverse stimulated Raman scattering gain during crystal-cut optimization, predicting maximum operational fluence, and helping to develop novel designs with complex polarization control (p. 56).
- T. J. Kessler reports on the BEST Program, designed to engage underrepresented high school students and their teachers in various aspects of science and technology that support LLE's laser science and applications research (p. 58).
- J. Puth *et al*. summarize operations of the Omega Laser Facility during the first quarter of FY22 (p. 63).

Nickolaos Savidis
Editor

Bound on Hot-Spot Mix in High-Velocity, High-Adiabat Direct-Drive Cryogenic Implosions Based on Comparison of Absolute X-Ray and Neutron Yields

R. C. Shah,[1] D. Cao,[1] L. Aghaian,[2] B. Bachmann,[2] R. Betti,[1] E. M. Campbell,[1] R. Epstein,[1] C. J. Forrest,[1] A. Forsman,[2] V. Yu. Glebov,[1] V. N. Goncharov,[1] V. Gopalaswamy,[1] D. R. Harding,[1] S. X. Hu,[1] I. V. Igumenshchev,[1] R. T. Janezic,[1] L. Keaty,[2] J. P. Knauer,[1] D. Kobs,[2] A. Lees,[1] O. M. Mannion,[1] Z. L. Mohamed,[1] D. Patel,[1] M. J. Rosenberg,[1] C. Stoeckl,[1] W. Theobald,[1] C. A. Thomas,[1] P. Volegov,[3] K. M. Woo,[1] and S. P. Regan[1]

[1]Laboratory for Laser Energetics, University of Rochester
[2]Lawrence Livermore National Laboratory
[3]Los Alamos National Laboratory

Here we report on new continuum x-ray measurements to characterize hot-spot x-ray yield and hot-spot electron temperature of a series of implosions typical of current best cryogenic designs.[1] The objective of these measurements is to consider the consistency of x-ray production relative to neutron production and assess if this ratio implies hot-spot mix. Because of the insufficient time for equilibration given plasma parameters in these high-velocity implosions, there are significant differences between the hot-spot electron and ion temperature, which can influence the comparison of the x-ray and neutron yields. Based on the measured neutron yield and both hot-spot temperatures, the expected x-ray yield (assuming a pure-DT hot spot) is determined for each implosion and then compared to the measured x-ray yield. The x-ray and neutron yields are found to be consistent without invoking hot-spot mix within an estimated sensitivity corresponding to ~2% by atom, fully ionized carbon–deuterium plastic.

The x-ray yield and electron-temperature measurements were newly developed for this experiment. Approximately 30 images of each implosion were generated using an array of differentially filtered circular apertures and recorded on an absolutely calibrated image plate (IP).[2] The imaging apertures make it possible to distinguish the hot-spot x rays from a background of neutrons and coronal x rays (the spatial identification of hot spot as compared to coronal x rays was corroborated with simulation data). The x rays were filtered with Al foils in order to have four data channels. After accounting for IP response, the mean recorded energies of the channels ranged from 10 to 18 keV. In this range, the dense fuel was optically thin, and the signal level was within the dynamic range of a single scan read of the IP (consistent with the calibration). The channel measurements were used to constrain an isobaric hot-spot model, and the hot spot (assumed static) was used to calculate the volume integrated bremsstrahlung x-ray continuum using the free–free emissivity for hydrogen. [Figures 1(a)–1(c) show examples of the data, measured and modeled channel signals, and inferred spectrum for shot 96806.] Finally, a neutron-weighted electron temperature (T_e) was calculated to parameterize the hot-spot electron temperature on similar footing as the ion temperature. For the simulations, post-processed x rays were spatially and temporally selected to isolate the hot-spot contribution. The hot-spot x rays from the simulations were then filtered by the experimentally used channel responses and analyzed using the same procedure as for the data.

The measured hot-spot electron and ion temperatures for five cryogenic implosions of 25 February 2020 that are typical of current best performing designs, as well as the values from 1-D simulation, are shown in the bar plot of Fig. 2. In contrast to the x-ray yield and electron temperature, neutron yield and ion temperature are routinely measured in inertial confinement fusion experiments on OMEGA. The hot-spot ion temperature (T_i) is inferred based on the temporal width of the neutron time of flight (nTOF), which, under ideal circumstances, characterizes a neutron-weighted ion temperature. This inferred T_i will be inflated by flows, which, if anisotropic, will result in variations of the inferred value as observed from different lines of sight.[3] In our experiments, there were five independent nTOF's and shown are the maximum and minimum values of T_i for each shot. The range between the extremes was large for only the first shot, for which a target defect was observed and believed to cause a large

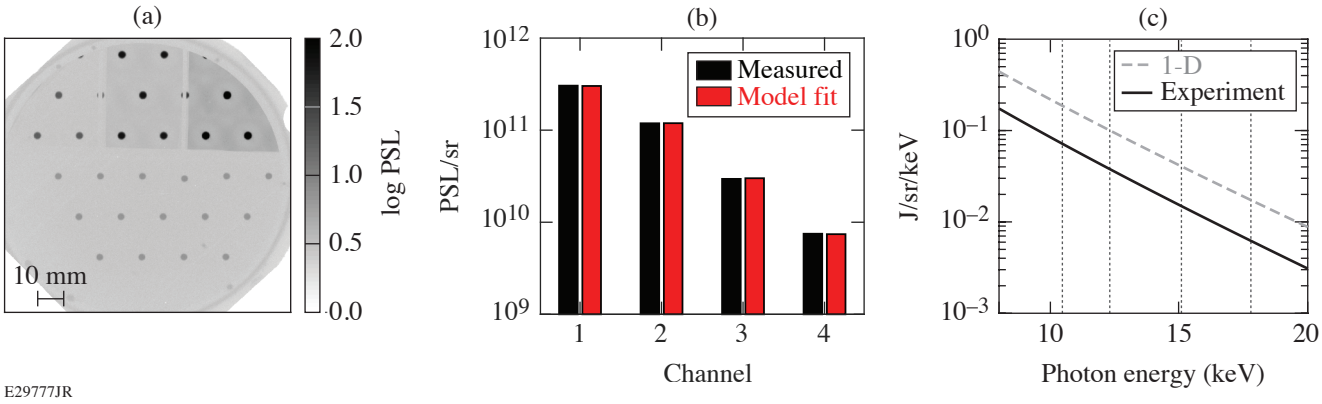

Figure 1
(a) Image-plate data for shot 96806 with image intensity reported in units of photostimulated luminescence (PSL). (b) Measured and fit channel signals. (c) The hot-spot model x-ray spectrum determined from the channel data. Dotted vertical lines indicate the mean recorded energy of each of the four imaging channels. For reference, the hot-spot model x-ray spectrum obtained from the identical analysis of the 1-D simulation is also plotted.

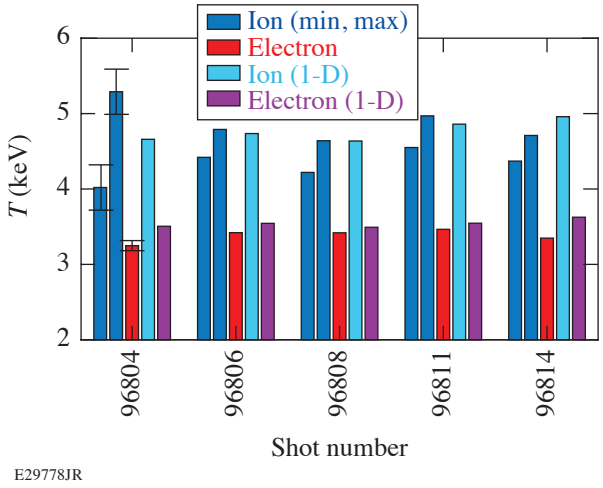

Figure 2
The measured hot-spot T_e is typically ~75% of the minimum T_i obtained from five independent lines of sight. The result is similar to what is obtained from 1-D simulations.

flow. In that case, the minimum T_i takes its lowest value. We have used the minimum nTOF T_i as the value best representative of the ion thermal conditions. Note that for the x-ray and neutron yield ratio comparison, an inflated value of T_i will increase the estimated hot-spot mix; therefore, in this sense the inferred mix quantification will be an upper bound estimate. Figure 2 also shows that the measured T_e value is typically ~75% of the minimum T_i. This degree of equilibration is similar to what is obtained in the 1-D simulation.

The predicted x-ray yield (Y_x) for a hot spot in the absence of mix is calculated using these temperatures as well as the measured neutron yield (Y_n). This result, along with the measured Y_x, is plotted in Fig. 3(a). There is a generally positive correlation of the measured x-ray and neutron yields contrasting what was reported by Ma *et al.*[4] in indirect-drive implosions of the National Ignition Campaign and for which mix was identified as a prominent issue. Additionally, since the measured and mapped values of Y_x do not significantly deviate, there is no measurable indication that mix is consistently present across these implosions. This is more explicitly shown in Fig. 3(b) as the ratio of the measured to mapped values, or x-ray enhancement. In this plot, the variability observed in the application of the model to a set of test simulations is indicated by the shaded region, and we interpret it as an estimate of the sensitivity by which we can measure an enhancement due to mix. The dashed lines in Fig. 3(b) indicate the value of the x-ray enhancement estimated for specified fractions of mix in the hot spot, accounting for the increase in both bremsstrahlung and recombination emission due to the carbon atoms. The measurement sensitivity is compromised by both the

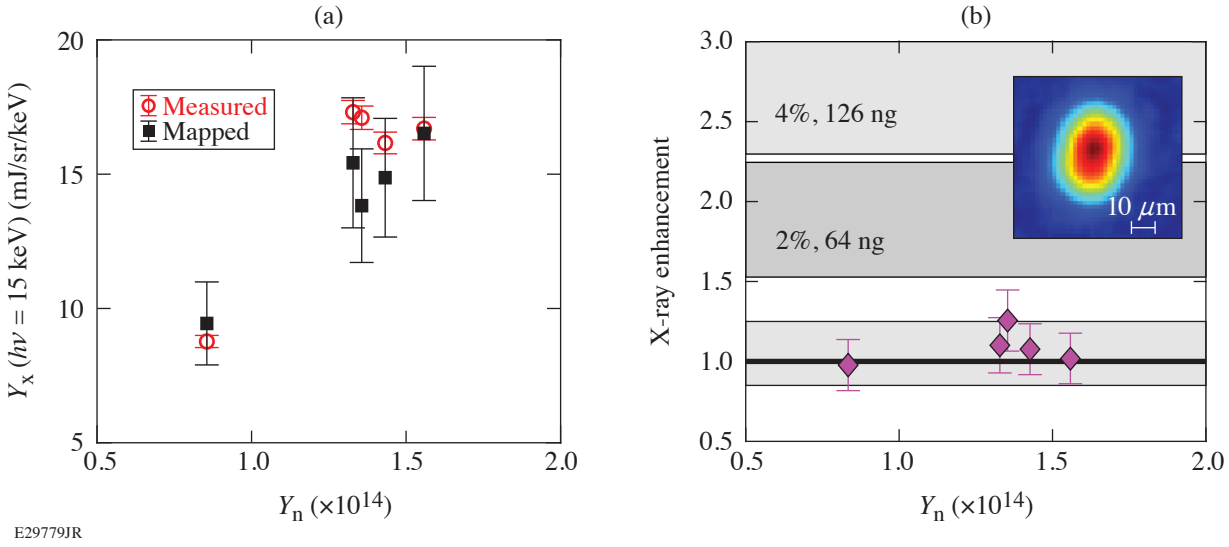

Figure 3
For each implosion, the measured Y_n, T_i, and T_e are used to calculate a mapped x-ray yield that is compared to the measured x-ray yield. (b) The x-ray enhancements fall within the systematic errors observed for the mapping (as determined by tests on a simulation database) indicated by the shaded gray region of the plot. The percentage values refer to percent-by-atom levels of CD mix required to cause the indicated level of x-ray enhancement. The inset shows the recovered hot-spot image from channel 1 for shot 96806.

error propagation (dominated by the hot-spot temperatures and indicated with error bars) as well as the model errors (indicated by the shaded region). We find no indication of hot-spot mix within the combined effect of these errors or an approximate sensitivity limited to ~2% by atom carbon–deuterium (64 ng, assuming a typical 1.2-μg hot spot). We have also extracted the hot-spot images from image-plate data using an established approximation to tomographic analysis,[5,6] applicable to the precisely machined circular apertures (General Atomics, San Diego). The inset of Fig. 3(b) shows the image with an estimated 8-μm resolution obtained from channel 1 for shot 96806. Typical of all the implosion and other channels, we do not identify the sorts of bright features which have been associated with mix in other experiments[7] in hot-spot images of these and similar implosions. It is plausible that decompression, peripheral bubbles, and residual motions, observed in multidimensional simulations[8] and also previously proposed based on experimental signatures,[9] dominate the hydrodynamic degradations without creating hot-spot mix.

In summary, measurements were presented of the x-ray yield and hot-spot electron temperature for direct-drive cryogenic implosion experiments. The comparison of the electron temperature with the ion temperature routinely characterized in the experiments was consistent with the prediction that ions and electrons remain substantially unequilibrated in the high-velocity, high-adiabat designs of present interest. The independently measured electron and ion temperatures of the hot spot with the D–T fusion neutron yield were used to estimate a corresponding x-ray yield expected from the nonequilibrium DT hot spot, assuming the absence of mix. The comparison of the measured and expected x-ray yields is consistent within the estimated sensitivity of the technique and therefore indicates that hot-spot mix, if present in these implosions, is at levels less than what the yield comparison can detect.

This material is based upon work supported by the Department of Energy National Nuclear Security Administration under Award Number DE-NA0003856, the University of Rochester, and the New York State Energy Research and Development Authority.

1. V. Gopalaswamy *et al.*, Nature **565**, 581 (2019).
2. M. J. Rosenberg *et al.*, Rev. Sci. Instrum. **90**, 013506 (2019); 029902(E) (2019).
3. T. J. Murphy, R. E. Chrien, and K. A. Klare, Rev. Sci. Instrum. **68**, 610 (1997).
4. T. Ma *et al.*, Phys. Rev. Lett. **111**, 085004 (2013).
5. B. Bachmann *et al.*, Rev. Sci. Instrum. **87**, 11E201 (2016).
6. G. Di Domenico *et al.*, Med. Phys. **43**, 294 (2016).

7. A. Pak *et al.*, Phys. Rev. Lett. **124**, 145001 (2020).
8. D. Cao *et al.*, "Understanding Origins of Observed Fusion Yield Dependencies," to be submitted to Physical Review Letters.
9. A. Bose *et al.*, Phys. Rev. E **94**, 011201(R) (2016).

Mitigation of Deceleration-Phase Rayleigh–Taylor Growth in Inertial Confinement Fusion Implosions

Y. Lawrence,[1,2] V. N. Goncharov,[2] K. M. Woo,[2] W. Trickey,[2] and I. V. Igumenshchev[2]

[1]University of Chicago
[2]Laboratory for Laser Energetics, University of Rochester

In inertial confinement fusion (ICF), small hot spots are desirable because they lower the threshold hot-spot energy required for ignition, $E_{\rm hs} > 16$ kJ $(R_{\rm hs}/50\ \mu{\rm m})^2$ (Refs. 1–4). However, they generally lead to greater implosion asymmetry due to the growth of the Rayleigh–Taylor (RT) instability on the inner shell surface during the deceleration phase. A challenge then arises of how to attain a high convergence ratio (CR, defined as the ratio of the initial inner shell radius to the hot-spot radius at peak compression), without excessively high RT growth. In this study we show that lowering the central density [by a factor of 5 or more compared to the vapor density of deuterium–tritium (DT) at triple point] has the greatest leverage in achieving small hot-spot sizes without excessive amplification of deceleration-phase RT.

First, we review some basic aspects of deceleration-phase RT growth. During the deceleration phase, initial perturbations on the inner shell surface grow exponentially because the less-dense hot spot pushes against the denser shell. Neglecting convergence effects and including only the instability drive term, $\Gamma_{\rm drive} = \int \sqrt{A_T k g}\, {\rm d}t$, where A_T is the Atwood number, g is the inner surface acceleration, and $k \cong \ell / R_{\rm hs}$ is the effective wave number ℓ [the inner surface perturbations are decomposed in spherical harmonics with the mode number ℓ (see also Ref. 5)] and $R_{\rm hs}$ is the position of the shell's inner surface. We postpone defining A_T until later in this summary and assume for now that $A_T \cong 1$. Evaluating this integral from the start of the deceleration phase until peak compression (when the hot-spot radius reaches its minimum value $R_{\rm hs,m}$), it can be shown that $\Gamma_{\rm drive} = \sqrt{2\ell}\,{\rm arcsinh}\left(\sqrt{{\rm CR_d} - 1}\right)$, where ${\rm CR_d} \equiv R_{\rm hs0} / R_{\rm hs,m}$ is the maximum hot-spot convergence ratio during shell deceleration and $R_{\rm hs0}$ is the hot-spot radius at the beginning of deceleration. So, to decrease the instability drive term, ${\rm CR_d}$ should be decreased, but to reduce the ignition threshold, $R_{\rm hs,m}$ must also be reduced. This means that the deceleration phase should start later (i.e., at a smaller radius); therefore, $R_{\rm hs0}$ needs to be reduced as well as ${\rm CR_d}$.

Now we turn to scaling laws for ${\rm CR_d}$ and $R_{\rm hs0}$ to identify the target design parameters that can achieve these desired reductions. It can be shown (following from Ref. 3) that

$$ {\rm CR_d} \sim \frac{v_{\rm imp}^{2/3}}{\alpha_{\rm inf}^{1/5} p_{\rm sh0}^{2/15}}, \tag{1} $$

where $v_{\rm imp}$ is the peak implosion velocity, $\alpha_{\rm inf}$ is the in-flight shell adiabat, and $p_{\rm sh0}$ is shell pressure at the onset of deceleration. Also,

$$ R_{\rm hs,m} = \frac{R_{\rm hs0}}{{\rm CR_d}} \sim R_0 \frac{p_0^{1/5} \alpha_{\rm inf}^{1/5}}{p_{\rm sh0}^{1/5} v_{\rm inf}^{2/3}}, \tag{2} $$

where R_0 is the initial inner surface radius and p_0 is the initial vapor (central) pressure of the target. Equations (1) and (2) show that CR_d and R_{hs0} can be reduced by lowering the initial vapor pressure p_0 and/or increasing the shell pressure at the start of deceleration p_{sh0}. The remaining reduction in RT growth for the lower-central-density design comes from the increase in the ablative stabilization and reduction in the Atwood number.

Mass ablation from the inner shell surface, characterized by an ablation velocity v_a, reduces RT growth since the hot spot preferentially ablates the RT spikes that contact the hot spot at higher temperature gradients. It can be shown (following from Refs. 6 and 7) that

$$v_a \sim \frac{\alpha_{inf}^{0.5} v_{imp}^{2.2}}{R_0 p_0^{0.2} p_{sh0}^{0.13}}, \quad \frac{v_a}{R_{hs,m}} \sim \frac{\alpha_{inf}^{0.3} v_{imp}^{2.85}}{R_0^2 p_0^{0.4} p_{sh0}^{0.07}}. \tag{3}$$

As with the deceleration-phase convergence ratio and hot-spot radius at the onset of deceleration, the mass ablation velocity v_a increases with a lower initial vapor pressure. Meanwhile, density scale lengths L_m that are higher correspond to lower Atwood numbers A_T. Following from the previously written scaling laws and Ref. 6, it can be shown that

$$L_m \sim R_0 p_0^{0.2} p_{sh0}^{0.27} \alpha_{inf}^{0.8} v_{imp}^{0.54}, \quad \frac{L_m}{R_{hs,m}} \sim v_{imp}^{1.2} p_{sh0}^{0.33}. \tag{4}$$

Equation (4) shows that L_m is larger in designs with increased shell pressure at the onset of deceleration, p_{sh0}. Taken together, the scaling laws in Eqs. (1)–(4) for CR_d, R_{hs0}, v_a, and L_m show the beneficial stabilizing effects of reducing the initial vapor density and increasing the shell pressure at the start of the deceleration phase. This is accomplished most efficiently by reducing the initial vapor pressure p_0. A lower initial vapor pressure leads to extra convergence of the central region necessary to build up its pressure and begin shell deceleration; then, because of the convergence effects, the shell pressure p_{sh0} at the beginning of deceleration increases as well. Furthermore, as will be shown in an upcoming paper, 1-D simulations in *LILAC*[8] show that low-central-density designs experience reduced CR_d and R_{hs0}, as well as increased v_a and L_m. However, the fairly weak dependence of the hot-spot convergence ratio and stabilizing terms on the initial vapor density requires that it must be significantly reduced (factor of 5 or more). While this is not feasible with nominal cryogenic targets, the new dynamic shell formation concept can achieve this reduction by controlling the strength of the blast wave and the duration of the target expansion phase.[9]

To validate these predictions, we use 2-D hydrodynamic simulations in *DEC2D*[10] to study perturbation amplification during shell deceleration for two dynamic shell designs driven by shorter and longer laser pulses. In Ref. 11, one can find details of the target dimensions and pulse shapes that produce central densities of 0.6 mg/cm^3 and 0.12 mg/cm^3, respectively. Figure 1 shows density maps for the two dynamic shell designs taken at times when the neutron production reaches $\dot{N} \cong 5 \times 10^{26}\,s^{-1}$. The perturbation amplification is significantly reduced in the lower-central-density design [Fig. 1(b)] compared to the high-central-density design [Fig. 1(a)], despite the smaller hot-spot size, in agreement with the scaling arguments described earlier. Similarly, Fig. 2(a), which shows the mode $\ell = 20$ growth for the two dynamic shell designs, again confirms larger stabilization effects in the lower-density design. Figure 2(b) compares even-mode spectra for the two designs. The greatest RT growth suppression for the lower-density design occurs at mid- and higher-mode numbers, while the improvement for the low-mode numbers is slightly more modest.

Motivated by various scaling laws, we have demonstrated with 2-D simulations that reducing the initial central density in ICF targets leads to smaller hot spots (reducing hot-spot energies required for ignition) and, at the same time, suppresses deceleration RT growth. The required central-density reduction can be achieved using the new dynamic shell-formation concept. These results show a promising path to achieving ignition and high gains in laser-direct-drive designs at moderate laser energies $E_{laser} \sim 1$ MJ.

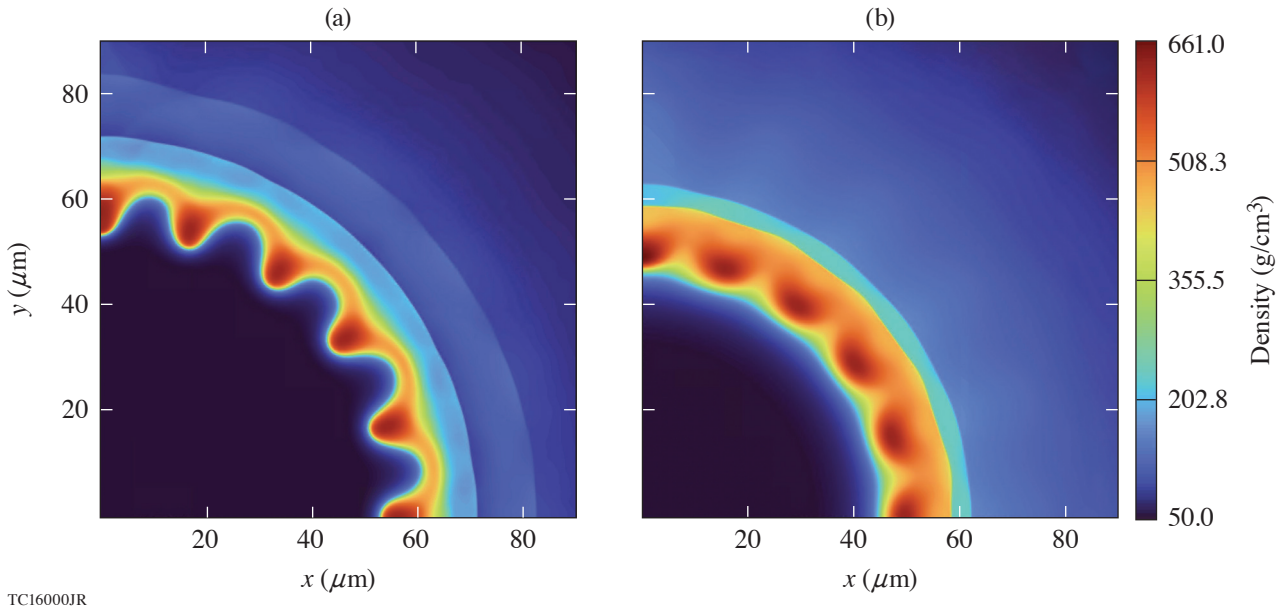

Figure 1
Two-dimensional density maps from mode $\ell = 20$ *DEC2D* simulations for the dynamic shell designs with (a) higher and (b) lower central densities (as described in Ref. 11), near stagnation at times of an equal neutron-production rate of $\dot{N} \cong 5 \times 10^{26}$ s^{-1}.

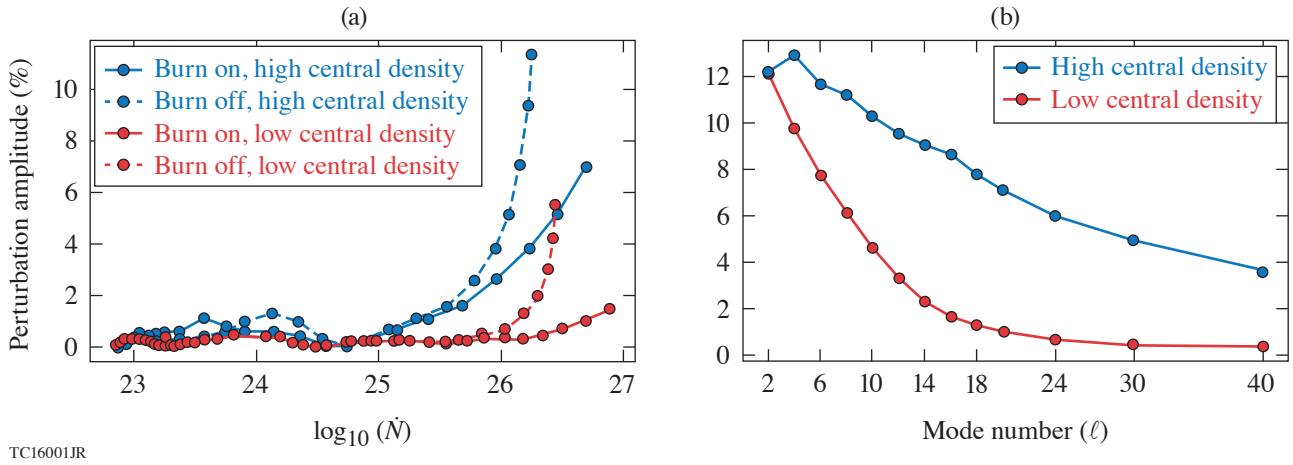

Figure 2
(a) Deceleration RT mode $\ell = 20$ evolution for dynamic shell designs with high/low central densities and alpha heating turned on or off. (b) Deceleration RT mode spectra with alpha heating turned on, taken at a neutron-production rate of $\dot{N} \cong 5 \times 10^{26}$ s^{-1} for the dynamic shell designs with high/low central densities. (Lines are used to guide the eye and do not represent fits.)

Funding was provided by the ARPA-E BETHE Grants No. DEFOA-0002212 and DE-AR0001272 and DOE OFES Award No. DE-SC0017951. This material is based upon work supported by the Department of Energy National Nuclear Security Administration under Award Number DE-NA0003856, the University of Rochester, and the New York State Energy Research and Development Authority.

1. J. D. Lindl, *Inertial Confinement Fusion: The Quest for Ignition and Energy Gain Using Indirect Drive* (Springer, New York, NY, 1998).
2. S. Atzeni and J. Meyer-ter-Vehn, *The Physics of Inertial Fusion: Beam Plasma Interaction, Hydrodynamics, Hot Dense Matter*, 1st ed., International Series of Monographs on Physics, Vol. **125** (Oxford University Press, Oxford, 2004).
3. V. N. Goncharov *et al.*, Phys. Plasmas **21**, 056315 (2014).
4. V. N. Goncharov *et al.*, Plasma Phys. Control. Fusion **59**, 014008 (2017).
5. V. N. Goncharov *et al.*, Phys. Plasmas **7**, 5118 (2000).
6. R. Betti *et al.*, Phys. Plasmas **8**, 5257 (2001).
7. C. D. Zhou and R. Betti, Phys. Plasmas **14**, 072703 (2007).
8. J. Delettrez *et al.*, Phys. Rev. A **36**, 3926 (1987).
9. V. N. Goncharov *et al.*, Phys. Rev. Lett. **125**, 065001 (2020).
10. K. M. Woo *et al.*, Phys. Plasmas **25**, 052704 (2018).
11. W. Trickey *et al.*, Front. Phys. **9**, 784258 (2021).

Emission Phases of Implosion X-Ray Sources for Absorption Spectroscopy

D. A. Chin,[1,2] J. J. Ruby,[1,2] P. M. Nilson,[1] D. T. Bishel,[1,2] F. Coppari,[3] Y. Ping,[3] A. L. Coleman,[3] R S. Craxton,[1] J. R. Rygg,[1,2,4] and G. W. Collins[1,2,4]

[1]Laboratory for Laser Energetics, University of Rochester
[2]Department of Physics and Astronomy, University of Rochester
[3]Lawrence Livermore National Laboratory
[4]Department of Mechanical Engineering, University of Rochester

At LLE's Omega Laser Facility, thin plastic shells were directly driven with ~20 kJ, resulting in a time-integrated x-ray yield of ~10^{12} ph/eV/sr at 7 keV. Using temporally, spatially, and spectrally discriminating diagnostics, three x-ray emission phases were identified: corona emission produced by the laser ablation of the shell, core stagnation, and afterglow emission due to the expanding hot material after stagnation. The newly measured corona and afterglow emission phases account for ~25% of the total x-ray signal and produce x-ray emission at a different time or larger radius than previously considered. The resulting implications of this additional emission for x-ray absorption fine structure (XAFS) spectroscopy are discussed.

This work presents a comprehensive measurement of the temporal, spatial, and spectral x-ray emission of implosion GDP (glow-discharge polymerization) shells on the OMEGA Laser System and identifies three experimental x-ray emission phases consisting of the corona, core stagnation, and afterglow. During the corona phase, the laser illuminates the shell, producing x-ray emission and driving a shock through the shell, causing the material to release inward. When the remaining material reaches the center, it stagnates, reaching Gbar pressures and producing a bright x-ray flash. After stagnating, the remaining material decompresses at Gbar pressures, remaining hot enough to emit x rays for a brief period of time. A schematic of each x-ray emission phase is shown in Fig. 1. To characterize the different emission phases, x-ray emission models were verified using a hydrodynamic simulation and fit to experimental data. The details of each emission phase are shown in Table I.

Table I: Fraction of the total emission in each phase obtained by fitting the streaked spectrum. The fractions are shown along with the 68% credible interval, which was calculated from uncertainty in the fit along with the variability between shots. The time duration was also calculated from the fit and represents the time interval that contains 95% of the signal. Lastly, the diameter was estimated from the time-integrated and time-resolved imaging.

	Corona	Core	Afterglow
Signal fraction	12^{+2}_{-2}	76^{+7}_{-6}	12^{+7}_{-6}
Time duration (ns)	0.2 to 1.1	1.0 to 1.1	1.1 to 1.4
Diameter (μm)	~850	~50	~300

The different spatial profiles of the x-ray sources directly impact the spectral resolution of the XAFS measurement. Using the Rowland (Yaakobi) x-ray spectrometer (XRS) as an example XAFS spectrometer, the impact of these three phases on the XAFS measurements can be estimated. An iron synchrotron absorption spectrum[1] was assumed to be the spectrum for a point source. To simulate the XAFS spectrum for the different source sizes, the point-source absorption spectrum was convolved with a Gaussian

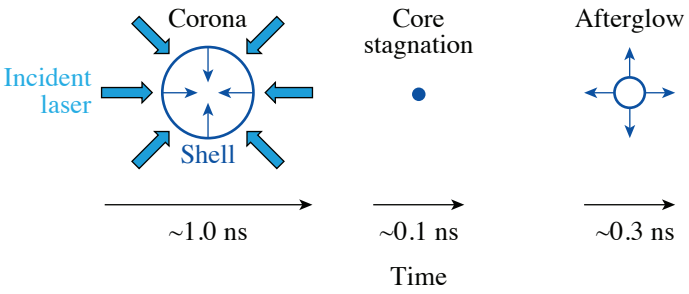

Figure 1
The x-ray emission occurs in three different phases: First, the incident laser causes the shell to emit x rays as the shell is ablated. Second, when the shell material stagnates in the center, there is a bright flash of x-ray emission. Finally, the remaining shell material expands and continues to emit x rays. The estimated time scale corresponds to an 865-μm-outer-diam, 9-μm-thick GDP shell.

function[2] whose full width at half maximum corresponded to the spectral resolution of each emission phase. The total signal was estimated by adding the signals from all three sources in transmission space while including the fractional weights from Table I.

The x-ray absorption near-edge spectroscopy (XANES) spectrum for each of the three phases along with the total signal is shown in Fig. 2(a). While the core spectrum is able to capture the majority of the features of the XANES spectrum, the corona and afterglow phases cannot. This is reflected in the total signal, which is not able to duplicate all of the features in the XANES spectrum. For example, the total spectrum loses the modulation, highlighted with the red arrow (in the inset plot), which can be used to distinguish structural changes and melting in iron.[3] Furthermore, the slope of the total spectrum is decreased, which must be accounted for when extracting the electron temperature.[4] Figure 2(b) shows the degraded extended x-ray absorption fine structure (EXAFS) spectra with each of the three phases and the total spectrum. Temperature can be extracted from the damping in the EXAFS modulations, and, under the harmonic approximation, this damping is given by $e^{-2k^2\mathrm{DWF}}$, where DWF represents the Debye–Waller factor.[5] Fitting[6] the point source and total signal spectra with this harmonic EXAFS approximation, the total signal spectrum has a DWF that is 16±6% larger. It should be noted that other spectrometers will have different spectral resolutions for each emission phase and will be impacted differently. Finally, these spectra represent a sample in a single thermodynamic state for the duration of the backlighter emission. If the material was not in a uniform thermodynamic state, each emission phase could potentially probe the material at a different density, temperature, or crystallographic structure resulting in shifting, amplifying, or decreasing XAFS modulations in unexpected ways.

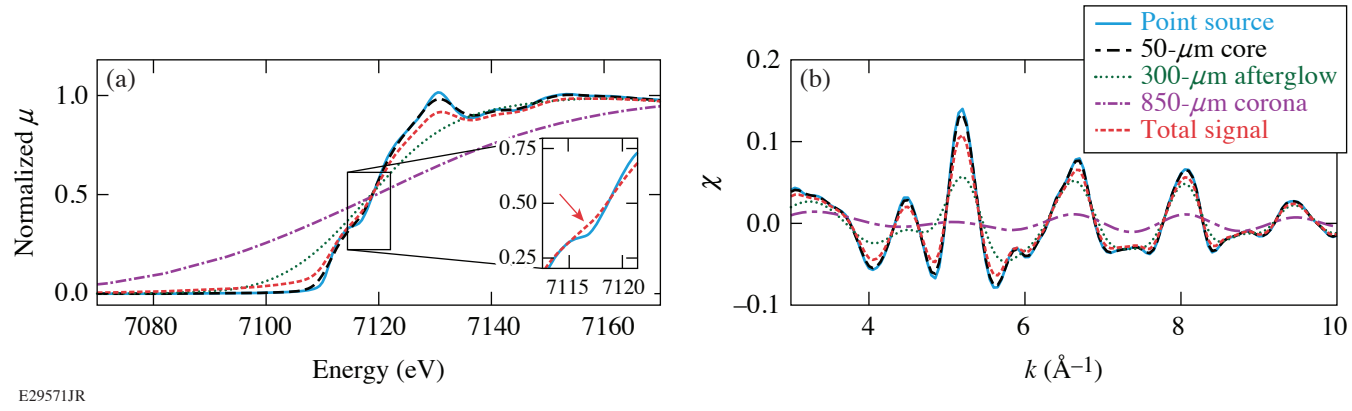

Figure 2
Iron XAFS spectra degraded with the three source sizes, assuming the XRS spectral resolutions. Iron synchrotron data[1] are assumed to give the point-source spectra. (a) XANES spectra as the normalized absorption coefficient (μ). The inset plot compares the point source and total signal with the other lines removed for visibility. The red arrow highlights a modulation that can be used to distinguish structural changes or melting in iron.[3] (b) The EXAFS data as $\chi(k)$ with E_0 = 7118 eV (Ref. 2).

This material is based upon work supported by the Department of Energy National Nuclear Security Administration under Award Number DE-NA0003856, the University of Rochester, and the New York State Energy Research and Development Authority. The support of DOE does not constitute an endorsement by DOE of the views expressed in this paper. D. Chin acknowledges

DOE NNSA SSGF support, which is provided under Cooperative Agreement No. DE-NA0003960. This collaborative work was partially supported under the auspices of the U.S. Department of Energy by Lawrence Livermore National Laboratory under Contract No. DE-AC52-07NA27344.

1. International X-Ray Absorption Society: Fe Data, IXAS X-Ray Absorption Data Library, Accessed 10 May 2021, https://xaslib.xrayabsorption.org/elem/.
2. B. Ravel and M. Newville, J. Synchrotron Rad. **12**, 537 (2005).
3. M. Harmand *et al.*, Phys. Rev. B **92**, 024108 (2015).
4. B. Kettle *et al.*, Phys. Rev. Lett. **123**, 254801 (2019).
5. E. Sevillano, H. Meuth, and J. J. Rehr, Phys. Rev. B **20**, 4908 (1979).
6. B. Ravel and M. Newville, J. Synchrotron Rad. **12**, 537 (2005).

Underdense Relativistically Thermal Plasma Produced by Magnetically Assisted Direct Laser Acceleration

K. Weichman,[1,2] J. P. Palastro,[1] A. P. L. Robinson,[3] and A. V. Arefiev[2,4]

[1]Laboratory for Laser Energetics, University of Rochester
[2]Department of Mechanical and Aerospace Engineering, University of California, San Diego
[3]Central Laser Facility, STFC Rutherford Appleton Laboratory
[4]Center for Energy Research, University of California, San Diego

The discovery of special relativity in 1905 transformed the fields of electromagnetism and charged-particle kinetics that, some 20 years later, would coalesce into the field of plasma physics. Predictions have continually emphasized the importance of special relativity in plasmas where the majority of electrons are relativistic regardless of reference frame, but, even today, experimental verifications of these predictions remain relatively rare. The laboratory generation of these relativistically thermal plasmas is needed to address open questions in astrophysics regarding shock acceleration and the origin of cosmic rays,[1] fast radio bursts,[2,3] and γ-ray bursts.[4] Relativistically thermal plasmas also feature a substantially modified response to electromagnetic radiation relative to the nonrelativistic or nonthermal cases, which is of significant interest in basic plasma physics,[5] laboratory astrophysics,[6,7] and laser-plasma physics.[8–11]

It is challenging, however, to produce relativistically thermal plasma in the laboratory with sufficient volume and duration for subsequent probing. Pulsed-power and microwave sources, while capable of igniting thermal plasma over large volumes, are incapable of reaching relativistic electron temperatures. Laser pulses with relativistic intensity ($I_0 \gtrsim 10^{18}$ W/cm^2 for $\lambda_0 = 1$-μm wavelength) are capable of imparting substantial energy to electrons, but they are conventionally unable to create persistent, large-volume plasma where the majority of electrons are relativistic. Configurations involving opaque plasma ($n_e > n_c$, where $n_c \approx 10^{21}$ cm^{-3} is the critical density for $\lambda_0 = 1$ μm),[12,13] near-critical density plasma,[14] or acceleration by the plasma (wakefield) electric field[15,16] typically leave the majority of electrons cold in either momentum or configuration space. In the underdense regime ($n_e < n_c$), laser pulses can volumetrically accelerate electrons to high energy,[17,18] but the plasma does not remain hot after the laser pulse passes due to the reversibility of the acceleration process. This reversibility is disrupted, however, by the addition of a uniform static magnetic field, enabling dramatic plasma heating.

We propose the first method to volumetrically generate relativistically thermal, underdense plasma. Our approach leverages two regimes of magnetically assisted direct laser acceleration, as illustrated in Figs. 1(a)–1(c). First, a $+x$-propagating, y-polarized relativistic short (20-fs) laser pulse interacts with electrons in an underdense (10^{-3} n_c) plasma with an embedded transverse magnetic field $B_0\hat{z} = 500$ T, imparting net energy as electrons slip through the full pulse duration [Fig. 1(b)]. Second, a longer (0.8-ps) laser pulse with the same propagation and polarization directions interacts with these preheated electrons, delivering half-laser-cycle energy kicks that promote the electron to higher-energy cyclotron orbits [Fig. 1(c)]. The short (subscript "s") and long (subscript "ℓ") laser pulses have peak normalized electric-field amplitude ($a_0 = |e|E_0/mc\omega_0$, where ω_0 is the laser frequency) of $a_s = 5$ and $a_\ell = 1$. Simulations were conducted in 2-D using the particle-in-cell code *EPOCH*.[19]

The interaction of the two laser pulses with the target creates multi-MeV average electron energy over a large volume (e.g., $r < w/2 = 25$ μm, where w is the HWHM laser spot size), which persists for picoseconds following the interaction [Fig. 1(d)]. The corresponding momentum spectrum is 2-D isotropic (in p_x and p_y) with a flat energy spectrum. While the plasma can be heated somewhat by the short laser pulse and magnetic field alone, significant relativistic heating requires all three elements of

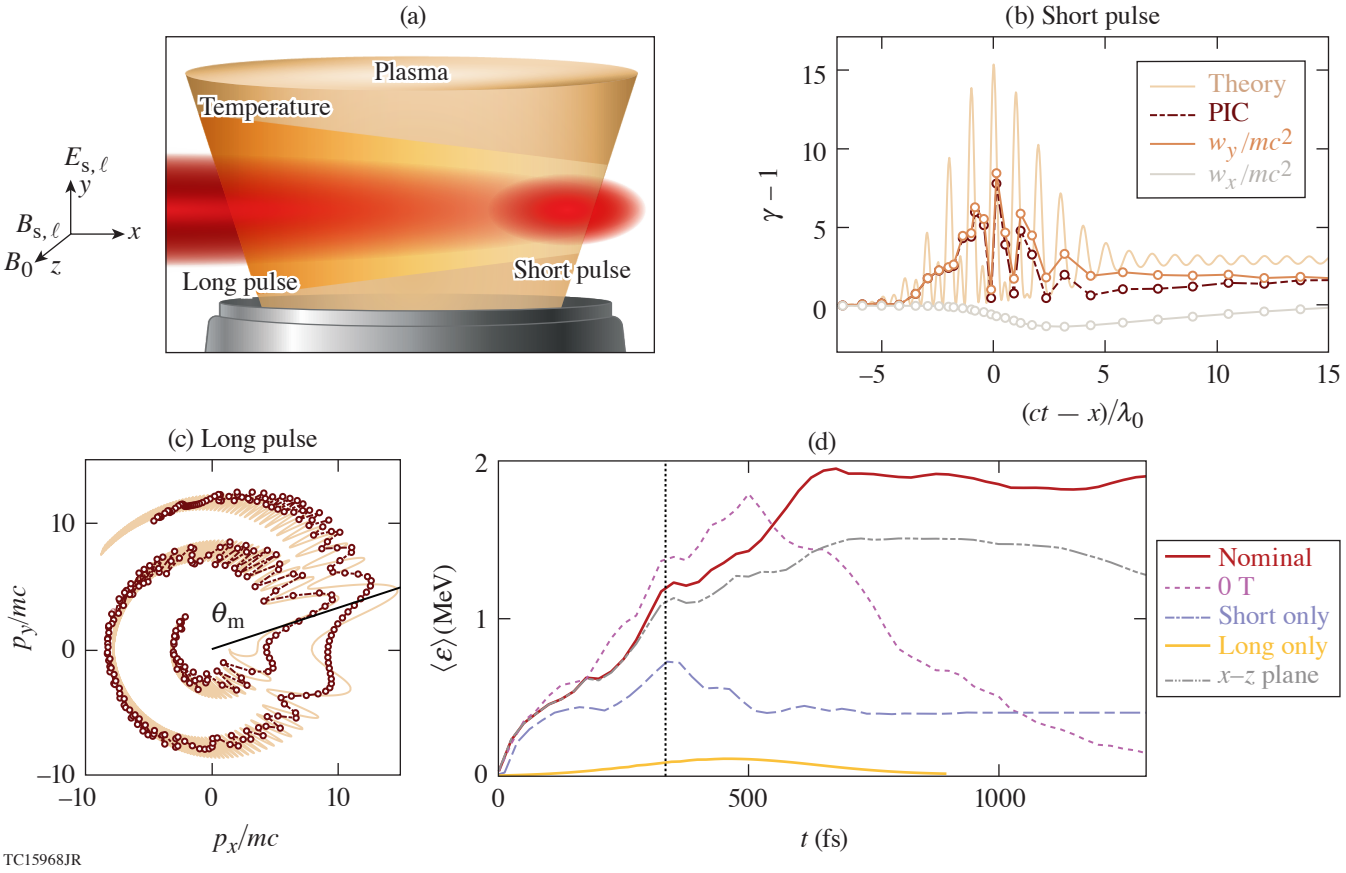

Figure 1
Generation of relativistic underdense plasma via magnetically assisted direct laser acceleration. (a) Illustration of laser and magnetic-field configuration. [(b),(c)] Example of the energy-gain process for a representative electron interacting with (b) the short pulse, and (c) the long pulse. w_y (w_x) is the work done by the transverse (longitudinal) electric field. (d) Average energy of all electrons in $r < 25$ μm. Vertical black dotted line: the time the peak of the short pulse leaves the plasma slab. The long-pulse intensity has dropped to a_ℓ/e at the right edge of the slab at the final time shown. The nominal case corresponds to both laser pulses and $B_{z0} = 500$ T, simulated in the x–y plane.

the short laser pulse, long laser pulse, and applied magnetic field [c.f., cases in Fig. 1(d)]. Unlike conventional laser-based heating methods, more than half of the electron population is heated to $\gamma \geqslant 2$, i.e., the plasma is relativistically thermal.

These observations are explainable as volumetric heating by magnetically assisted direct laser acceleration in the two distinct regimes covered by the short pulse and the long pulse. The energy retained following electron interaction with the short laser pulse through multicycle magnetically assisted direct laser acceleration[20] is used to catalyze subsequent heating by a long (picosecond) laser pulse via half-cycle magnetically assisted direct laser acceleration.[21] The latter process is capable of imparting higher net energy than the former; however it requires preheating of electrons, which in our case is provided by the short pulse.

The generation of relativistically thermal plasma is robust to increased electron density (up to $10^{-2}\,n_c$), finite laser spot size in the magnetic-field direction, and lower applied magnetic-field strength (e.g., 200 T). The average electron energy can additionally be increased by increasing the plasma size and the laser pulse duration, as shown in Fig. 2.

Our results demonstrate that the generation of underdense, relativisitically thermal plasma can be realized with currently available laser and magnetic-field–generation capabilities. With a 200-T magnetic field, we anticipate multi-MeV average electron energy under gas-jet–relevant conditions ($n_e \sim 10^{18}$ cm^{-3}, few-millimeter plasma size) using kilojoule-class laser pulses with a

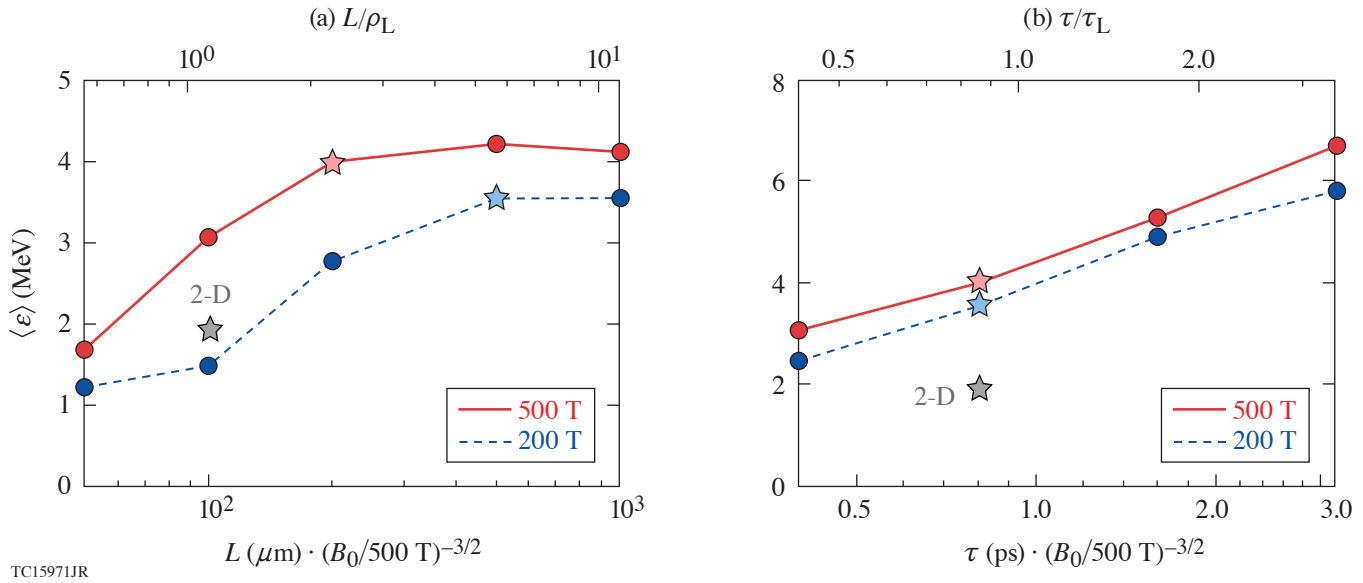

Figure 2
Strategies for improving average electron energy in 1-D particle-in-cell simulations. (a) Scan over plasma size near $L/\rho_L \sim 1$ with fixed duration. (b) Scan over long-pulse duration near $\tau_\ell/\tau_L \sim 1$ with fixed plasma size. ρ_L and τ_L are the Larmor radius and cyclotron period associated with the maximum energy that can be delivered in a half-cycle energy kick $\Delta\gamma \sim 2^{3/2}a^{3/2}_\ell\,(\omega_0/\omega_{c0})^{1/2}$. The starred points are shared between (a) and (b). The peak of the short pulse is kept coincident with a_ℓ/e on the rising edge of the long pulse. τ_s = 50 fs for the 200-T cases.

few-hundred-micron spot size and 50-fs/multipicosecond duration. Our approach is thereby anticipated to offer the first practical access to the relativistically thermal plasma regime, enabling experimental verification of longstanding, foundational predictions in basic plasma physics, laboratory astrophysics, and laser-plasma physics.

We thank R. Bingham (STFC Rutherford-Appleton Laboratory) for useful discussions. This material is based upon work supported by the Department of Energy National Nuclear Security Administration under Award Number DE-NA0003856, the University of Rochester, and the New York State Energy Research and Development Authority, and the DOE Office of Science under Grant No. DESC0018312. A. V. Arefiev was supported by NSF Grant No. 1903098. The support of DOE does not constitute an endorsement by DOE of the views expressed in this paper. Particle-in-cell simulations were performed using *EPOCH*,[19] developed under UK EPSRC Grant Nos. EP/G054940, EP/G055165, and EP/G056803. This work used HPC resources of the National Energy Research Scientific Computing Center (NERSC), a U.S. Department of Energy Office of Science User Facility operated under Contract No. DE-AC02-05CH11231, and the Extreme Science and Engineering Discovery Environment (XSEDE),[22] which is supported by National Science Foundation grant number ACI-1548562, under allocation TG-PHY190034 on the Texas Advanced Computing Center (TACC) at The University of Texas at Austin.

1. R. Blandford and D. Eichler, Phys. Rep. **154**, 1 (1987).
2. R. Bingham *et al.*, Astrophys. J. **595**, 279 (2003).
3. B. D. Metzger, B. Margalit, and L. Sironi, Mon. Not. R. Astron. Soc. **485**, 4091 (2019).
4. P. Kumar and B. Zhang, Phys. Rep. **561**, 1 (2015).
5. J. Bergman and B. Eliasson, Phys. Plasmas **8**, 1482 (2001).
6. M. Lontano, S. Bulanov, and J. Koga, Phys. Plasmas **8**, 5113 (2001).
7. T.-Y. B. Yang, J. Arons, and A. B. Langdon, Phys. Plasmas **1**, 3059 (1994).
8. D. J. Stark *et al.*, Phys. Rev. Lett. **115**, 025002 (2015).
9. G. Li, W. B. Mori, and C. Ren, Phys. Rev. Lett. **110**, 155002 (2013).
10. Y. Zhao *et al.*, Phys. Plasmas **21**, 112114 (2014).
11. J. S. Ross *et al.*, Phys. Rev. Lett. **104**, 105001 (2010).

12. M. A. Purvis *et al.*, Nat. Photonics **7**, 796 (2013).
13. S. M. Weng *et al.*, Sci. Rep. **6**, 22150 (2016).
14. G. Li *et al.*, Phys. Rev. Lett. **100**, 125002 (2008).
15. T. Tajima and J. M. Dawson, Phys. Rev. Lett. **43**, 267 (1979).
16. E. Esarey, C. B. Schroeder, and W. P. Leemans, Rev. Mod. Phys. **81**, 1229 (2009).
17. J. Krüger and M. Bovyn, J. Phys. A **9**, 1841 (1976).
18. F. V. Hartemann *et al.*, Phys. Rev. E **51**, 4833 (1995).
19. T. D. Arber *et al.*, Plasma Phys. Control. Fusion **57**, 113001 (2015).
20. A. P. L. Robinson and A. V. Arefiev, Phys. Plasmas **27**, 023110 (2020).
21. A. Arefiev, Z. Gong, and A. P. L. Robinson, Phys. Rev. E **101**, 043201 (2020).
22. J. Towns *et al.*, Comput. Sci. Eng. **16**, 62 (2014).

An Independent-Hot-Spot Approach to Multibeam Laser–Plasma Instabilities

R. K. Follett, H. Wen, D. H. Froula, D. Turnbull, and J. P. Palastro

Laboratory for Laser Energetics, University of Rochester

In laser-driven inertial confinement fusion (ICF), a millimeter-scale cryogenic capsule of deuterium–tritium fuel with a thin outer ablator is imploded by either direct laser illumination (direct drive) or focusing the lasers onto the interior walls of a hohlraum to generate an x-ray bath (indirect drive).[1] In both cases, the many high-intensity laser beams overlapping in underdense plasma can drive various laser–plasma instabilities (LPI's) that can severely inhibit implosion performance.[2,3]

Analytic results for instability behavior are typically limited to the case of a single plane-wave laser driving instability in the linear regime. ICF experiments, however, involve multiple overlapping laser beams, each using a phase plate that generates a complex speckle pattern in the plasma,[4] and accurate predictions of instability behavior require a description that accounts for their combined interaction.[5] Analytic theories for instability behavior in a single speckled beam have been developed using the independent-hot-spot model, where a statistical description of the speckle intensity is combined with the single-speckle instability behavior to predict the global instability behavior.[6,7] Multibeam interactions have historically been described using the common-wave model, where wave-vector matching considerations are used to show that overlapping laser beams can couple to a shared daughter wave propagating along the drive-beam axis of symmetry.[8–13] However, recent experiments and simulations of multibeam LPI's have shown that the common-wave description often fails to predict instability behavior. In particular, laser beams that do not satisfy the geometric requirements imposed by the common-wave matching conditions can still contribute to instability growth.[14–16]

Here we develop a multibeam hot-spot model that provides a more-predictive description of LPI behavior than the widely used common-wave approach. The model is extended to include absolute instability in an inhomogeneous plasma and applied to the two-plasmon–decay (TPD) instability. The excellent agreement with multibeam *LPSE* simulations demonstrates its utility and shows that there is an important qualitative difference between 2-D and 3-D single-speckle instability thresholds that is not present in the plane-wave case and results in lower instability thresholds in 2-D. This approach leads to a new understanding of multibeam instability behavior that can be used to make better quantitative predictions for improving the design of experiments and future laser facilities.

Given a collection of N speckles, the absolute instability threshold occurs when the peak speckle intensity is equal to the single-speckle threshold, $I_M = I_{\text{thr,speckle}}$. Introducing the average laser intensity I_0 and ensemble averaging over speckle realizations, this can be written as

$$I_{\text{thr}} = \frac{1}{\left\langle I_M / I_0 \right\rangle} I_{\text{thr,speckle}}, \tag{1}$$

where we have defined the expected average intensity at threshold $I_{\text{thr}} \equiv \left\langle I_0 \right\rangle$. Accordingly, evaluation of the expected threshold in the independent-hot-spot model is reduced to the evaluation of $\left\langle I_M / I_0 \right\rangle$ and $I_{\text{thr,speckle}}$. The expected peak speckle intensity can be written in terms of the probability that every speckle intensity is less than u:[17]

$$\left\langle I_M / I_0 \right\rangle = \int_0^\infty \left[1 - P\left(I / I_0 < u\right)^N\right] \mathrm{d}u. \tag{2}$$

Reference 18 derives speckle distributions that are valid for high-intensity speckles but behave badly at low intensities. Accordingly, we use exponential distributions at low intensities to generate probability distributions that behave well at all intensities:

$$P\left(I/I_0 > u\right)_{2\text{-D}} = \begin{cases} e^{-u/\mu_2}, & u < u_{s2} \\ A_2\left[\left(\frac{1}{2}+\frac{\pi}{4}\right)u+\frac{1}{2}\right]e^{-u}, & u > u_{s2} \end{cases}, \tag{3}$$

$$P\left(I/I_0 > u\right)_{3\text{-D}} = \begin{cases} e^{-u/\mu_3}, & u < u_{s3} \\ A_3\left[u^{3/2}-\frac{3}{10}u^{1/2}\right]e^{-u}, & u > u_{s3} \end{cases}, \tag{4}$$

where the μ_i are parameters and the A_i and u_{si} are chosen to make the distributions and their first derivatives continuous. Here $\mu_2 = \mu_3 = 4$ was chosen on the basis of comparison to simulations, which gives $A_2 = 1.185$, $u_{s2} = 0.944$, $A_3 = 1.848$, and $u_{s3} = 2.210$.

Incorporating Eqs. (3) and (4) into Eq. (2), using the binomial theorem, and integrating gives

$$\left\langle I_M/I_0\right\rangle_{2\text{-D}} = \sum_{a=1}^{N}\binom{N}{a}(-1)^a\left[\frac{\mu_2}{a}\left(e^{-au_{s2}/\mu_2}-1\right)-A_2^a a^{-1-a}e^{2a/2+\pi}\left(\frac{2+\pi}{4}\right)^a\Gamma\left(1+a,\frac{2a}{2+\pi}+au_{s2}\right)\right], \tag{5}$$

$$\left\langle I_M/I_0\right\rangle_{3\text{-D}} = \sum_{a=1}^{N}\binom{N}{a}(-1)^a\left[\frac{\mu_3}{a}\left(e^{-au_{s3}/\mu_3}-1\right)-A_3^a\sum_{k=0}^{a}\binom{a}{k}\left(-\frac{3}{10}\right)^k a^{k-1-3a/2}\Gamma\left(1-k+3a/2,au_{s3}\right)\right], \tag{6}$$

where $\Gamma(s,x)$ is the incomplete gamma function.

To determine N, we restrict our discussion to instabilities that are spatially localized by plasma inhomogeneity such that N is the number of speckles in a cross section of the laser field (i.e., the interaction region is not significantly longer than the speckle length). Accordingly, N is approximately the laser power divided by the mean power in a speckle, $N = P_L/\langle P_s\rangle$. The laser power is the average intensity times the cross-sectional area ($P_L = I_0\sigma_b$). To determine the mean power in a speckle, we first average over the probability density of speckle intensities to obtain the mean speckle intensity $\left\langle I/I_0\right\rangle = \int_0^\infty uP(u)\mathrm{d}u$, where $P(u) = -\partial P\left(I/I_0 > u\right)/\partial u$. Equations (3) and (4) give

$$\left\langle I/I_0\right\rangle_{2\text{-D}} = \mu_2-\left(\mu_2+u_{s2}\right)e^{-u_{s2}/\mu_2}+A_2e^{-u_{s2}}\left[4+\pi+(4+\pi)u_{s2}+(2+\pi)u_{s2}^2\right]/4, \tag{7}$$

$$\left\langle I/I_0\right\rangle_{3\text{-D}} = \mu_3-\left(\mu_3+u_{s3}\right)e^{-u_{s3}/\mu_3}+A_3\left[\frac{3\sqrt{\pi}}{5}\operatorname{erfc}\left(\sqrt{u_{s3}}\right)+e^{-u_{s3}}\sqrt{u_{s3}}\left(u_{s3}^2+\frac{7}{10}u_{s3}+\frac{6}{5}\right)\right], \tag{8}$$

where erfc(x) is the complementary error function. For speckles with a Gaussian transverse profile $\left[I(r) = Ie^{-\left(2\sqrt{\log 2}\,r/w_s\right)^2}\right]$ and full width at half maximum (FWHM) w_s, integration over r gives the mean power in a speckle, $\langle P_s\rangle_{2\text{-D}} = \left\langle I/I_0\right\rangle_{2\text{-D}}I_0w_s\sqrt{\pi/\log 2}$ and $\langle P_s\rangle_{3\text{-D}} = \left\langle I/I_0\right\rangle_{3\text{-D}}I_0w_s^2\pi/(4\log 2)$. Finally, the expected number of speckles in 2-D and 3-D, respectively, is

$$N = \frac{\sigma_b}{w_s\left\langle I/I_0\right\rangle_{2\text{-D}}}\sqrt{\frac{\log 2}{\pi}}, \tag{9}$$

$$N = \frac{\sigma_b}{w_s^2 \langle I/I_0 \rangle_{3\text{-D}}} \frac{4\log 2}{\pi}. \tag{10}$$

The single-speckle threshold ($I_{\text{thr,speckle}}$) generally depends on the speckle size, plasma conditions, and the instability under consideration. An analytic approximation can be obtained by constructing a spatially localized solution out of the linear eigenmodes for a plane-wave drive laser,[19] but it is not sufficiently accurate for quantitative applications. Here we take a semi-analytic approach where the speckle statistics are given by Eqs. (5) and (6), while $I_{\text{thr,speckle}}$ is taken from single-speckle *LPSE* simulations.

Figure 1 compares Eq. (1) to various speckled-beam *LPSE* calculations. The thresholds are normalized to the threshold for a single plane-wave drive beam, $I_{\text{thr,TPD}}$ (Ref. 19). Figure 1(a) shows 2-D calculations using a single beam with a varying *f* number at $L_n = 200\ \mu$m, $T_e = 2$ keV, and $L_n = 400\ \mu$m, $T_e = 4$ keV, which are similar to the conditions in direct-drive ICF experiments on the OMEGA[20] and National Ignition Facility[15] lasers, respectively. The thresholds are higher in the longer-scale-length calculations because, for a given speckle width, the single-speckle threshold increases with increasing temperature and scale length. The non-monotonic nature of the thresholds is a result of the competition between the increasing thresholds with decreasing speckle size and the increased number of speckles with decreasing *f* number.

Figures 1(b) and 1(c) show 3-D instability thresholds for $L_n = 200\ \mu$m, $T_e = 2$ keV and $L_n = 400\ \mu$m, $T_e = 4$ keV, respectively, for three different beam configurations: (1) a single beam with varying *f* number; (2) six *f*/6.7 beams uniformly distributed on a cone relative to the *x* axis with polar angle θ and azimuthal angle for the *m*th beam $\varphi_m = 2\pi m/6$; and (3) eight *f*/6.7 beams organized into two four-beam cones with polar angles θ and $\theta/2$ and azimuthal angles $\varphi_m = 2\pi m/4$ and $\varphi_m = 2\pi m/4 + \pi/4$, respectively. For the multibeam cases, the horizontal axis corresponds to an effective *f* number given by the cone angle, $f_{\#} = 1/(2\tan\theta)$ and the beam polarizations were aligned. All three beam configurations give the same threshold to within statistical variations and are in good agreement with the semi-analytic model. This shows that the instability behavior is predominantly determined by the smallest (and highest intensity) speckles and justifies the treatment of the cones of beams as a single beam with a small effective *f* number.

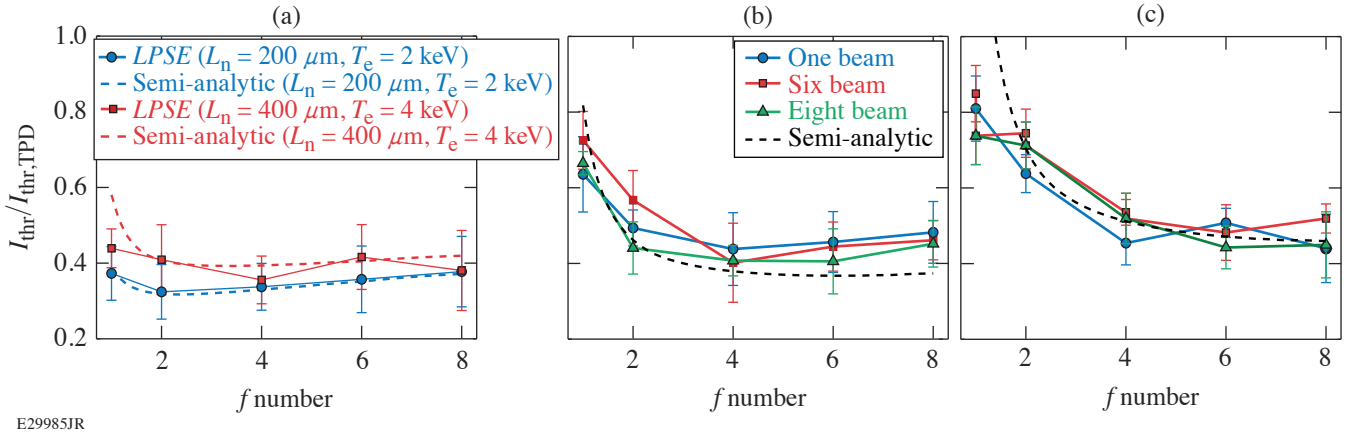

Figure 1
Absolute TPD instability thresholds for speckled beams (normalized to the plane-wave threshold). (a) Two-dimensional *LPSE* calculations at $L_n = 200\ \mu$m, $T_e = 2$ keV (blue circles), and $L_n = 400\ \mu$m, $T_e = 4$ keV (red squares). [(b),(c)] Three-dimensional *LPSE* calculations show $L_n = 200\ \mu$m, $T_e = 2$ keV and $L_n = 400\ \mu$m, $T_e = 4$ keV, respectively, for one beam (blue circles), six beams (red squares), and eight beams (green triangles). The dashed curves show the corresponding semi-analytic results. The error bars correspond to the standard deviation from an ensemble of 20 (5) speckle realizations in 2-D (3-D).

This material is based upon work supported by the Department of Energy National Nuclear Security Administration under Award Number DE-NA0003856, ARPA-E BETHE grant number DE-FOA-0002212, the University of Rochester, and the New York State Energy Research and Development Authority.

1. S. Atzeni and J. Meyer-ter-Vehn, *The Physics of Inertial Fusion: Beam Plasma Interaction, Hydrodynamics, Hot Dense Matter*, 1st ed., International Series of Monographs on Physics, Vol. 125 (Oxford University Press, Oxford, 2004).
2. W. L. Kruer, *The Physics of Laser Plasma Interactions, Frontiers in Physics*, Vol. 73, edited by D. Pines (Addison-Wesley, Redwood City, CA, 1988).
3. R. S. Craxton *et al*., Phys. Plasmas **22**, 110501 (2015).
4. Y. Kato *et al*., Phys. Rev. Lett. **53**, 1057 (1984).
5. C. Stoeckl *et al*., Phys. Rev. Lett. **90**, 235002 (2003).
6. H. A. Rose and D. F. DuBois, Phys. Rev. Lett. **72**, 2883 (1994).
7. V. T. Tikhonchuk, C. Labaune, and H. A. Baldis, Phys. Plasmas **3**, 3777 (1996).
8. D. F. DuBois, B. Bezzerides, and H. A. Rose, Phys. Fluids B **4**, 241 (1992).
9. D. T. Michel *et al*., Phys. Rev. Lett. **109**, 155007 (2012).
10. P. Michel *et al*., Phys. Rev. Lett. **115**, 055003 (2015).
11. J. Zhang *et al*., Phys. Rev. Lett. **113**, 105001 (2014).
12. D. T. Michel *et al*., Phys. Plasmas **20**, 055703 (2013).
13. J. F. Myatt *et al*., Phys. Plasmas **21**, 055501 (2014).
14. R. K. Follett *et al*., Phys. Plasmas **24**, 102134 (2017).
15. M. J. Rosenberg *et al*., Phys. Rev. Lett. **120**, 055001 (2018).
16. R. K. Follett *et al*., Phys. Rev. E **101**, 043214 (2020).
17. B. Eisenberg, Stat. Probab. Lett. **78**, 135 (2008).
18. J. Garnier, Phys. Plasmas **6**, 1601 (1999).
19. A. Simon *et al*., Phys. Fluids **26**, 3107 (1983).
20. T. R. Boehly *et al*., J. Appl. Phys. **85**, 3444 (1999).

Density Reconstruction in Convergent High-Energy-Density Systems Using X-Ray Radiography and Bayesian Inference

S. Ressel,[1,*] J. J. Ruby,[1,2,†] G. W. Collins,[1,2,3] and J. R. Rygg[1,2,3]

[1]Laboratory for Laser Energetics, University of Rochester
[2]Department of Physics and Astronomy, University of Rochester
[3]Department of Mechanical Engineering, University of Rochester
[*]Currently at Department of Atmospheric Sciences, University of Washington
[†]Currently at Lawrence Livermore National Laboratory

X-ray radiography is a technique frequently used to diagnose convergent high-energy-density (HED) systems, such as inertial confinement fusion (ICF) implosions, and to provide unique information that is not available through self-emission measurements. We investigate the scope and limits of that information using a radiography simulation combined with Bayesian inference workflow. The accuracy of density reconstruction from simulated radiographs of spherical implosions driven with 20 kJ of laser energy is assessed, including the increase or decrease in accuracy due to the addition of Lagrangian marker layers, Poisson noise, and improved prior information. This work is the first to present the full uncertainty distributions inferred from radiography analysis in HED systems and demonstrates the importance of constructing the full posterior probability density, as opposed to a point estimate, due to the modal structure of the likelihood surface introduced by typical experimental noise sources. This general methodology can be used for both robust analysis of radiographic data and improved design of radiography experiments by modeling the full experimental system.

The inference workflow was tested on realistic data generated from the 1-D radiation-hydrodynamic code *LILAC*, where a single spherically converging shock wave was simulated in a solid hydrocarbon sphere (CH) driven by 27 kJ of UV light using the *SESAME* 7592 EOS table and Los Alamos's astrophysical opacity tables. The resulting radial density profiles are used to generate a simulated radiograph, using a straight-line ray trace to simulate the optical system of an x-ray streak camera with a slit imager, to determine how much density-profile information is encoded in the lineout and to what extent the density profile can be reconstructed from lineout data.

The parameterization used to represent the *LILAC* density profile is similar in form to previous work[1] and is given by

$$\rho(r) = \rho_0; r < r_s,$$

$$\rho(r) = \rho_s + (\rho_p - \rho_s)(r - r_s)/(r_p - r_s); r_s < r < r_p,$$

$$\rho(r) = \rho_p \cdot \exp\left[-(r - r_p)^2/(2\sigma^2)\right]; r_p < r < r_e,$$

$$\rho(r) = \rho_e \cdot \exp\left[-a(r - r_e)\right]; r_e < r,$$

$$\text{and } \sigma = \sqrt{-(r_p - r_e)^2/2\ln(\rho_e - \rho_p)}. \quad (1)$$

where r_s, r_p, and r_e are the radial locations of the shock, peak density, and tail, respectively; ρ_0, ρ_s, ρ_p, and ρ_e are the densities of the material in ambient conditions, immediately after being shocked, at its maximum due to converging flows, and at the tail of the density profile, respectively; and α is a scale parameter that determines how quickly the density reduces to zero in the tail.

The results of using Bayesian inference to construct the posterior probability densities for the parameters in the density profile (shown in Fig. 1) demonstrate that some additional information is needed to constrain the inferred shock compression. Figure 2(a) shows the uniform prior distribution (green) for the shock compression, alongside the posteriors from inference including an additional constraint and including noise. A defining feature of the inference from these cases is the upper limit placed on the shock compression, which can be used in combination with outside information to further constrain the posterior.

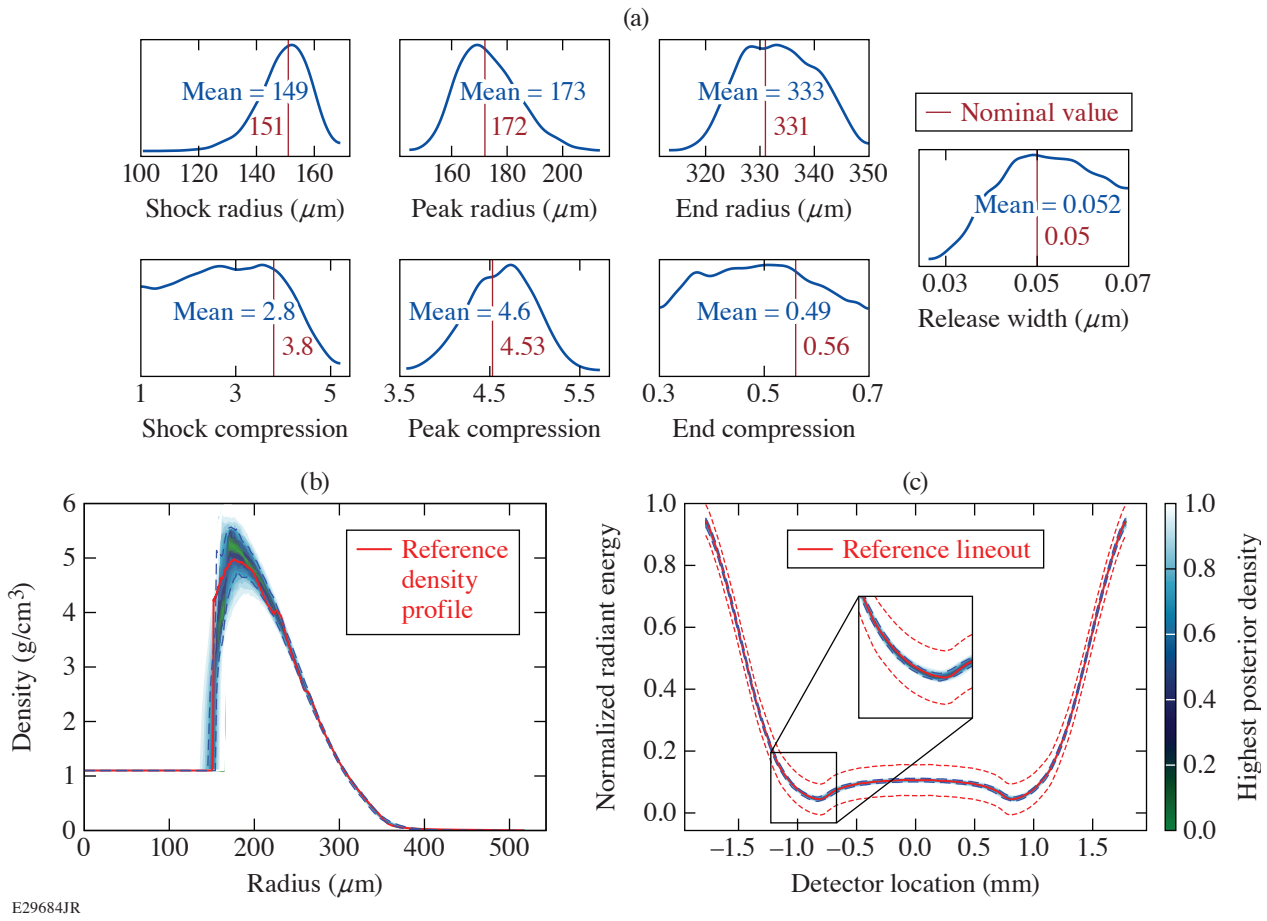

Figure 1

(a) Posterior distributions for each of the seven parameters of the model given in Eq. (1), as well as (b) posterior predictive distributions (PPD's) of the density profiles and (c) lineouts generated from said posterior distributions. A number of the parameters are well constrained, as shown by a single narrow peak in their posterior distributions, including the location of the shock, the location of the peak density, and the peak compression, and they all recover the underlying nominal value, given by the vertical red line, which is the least-squares best fit value recovered by fitting the simulated density profile with the assumed model. Notably, the posterior distribution for the shock compression (ρ_s/ρ_0) is not well constrained, presenting an upper bound of about 4, but roughly equal probability density across all values below 4. This can also be seen in (b), which is well matched to the reference density profile outside the region of the shock. Despite this, the PPD's of the lineouts in (c) are converged from the inference and well matched to the reference information, even around the feature due to the shock limb highlighted in the inset.

The simplest way to introduce this outside information is by using a more-informed prior distribution—for example, one that introduces a lower limit on the shock compression. A naive implementation is shown in Fig. 2(b) where the data-informed prior (orange) is simply a uniform distribution with a lower bound set by the maximum compression measurement of 3.39 (Ref. 2)

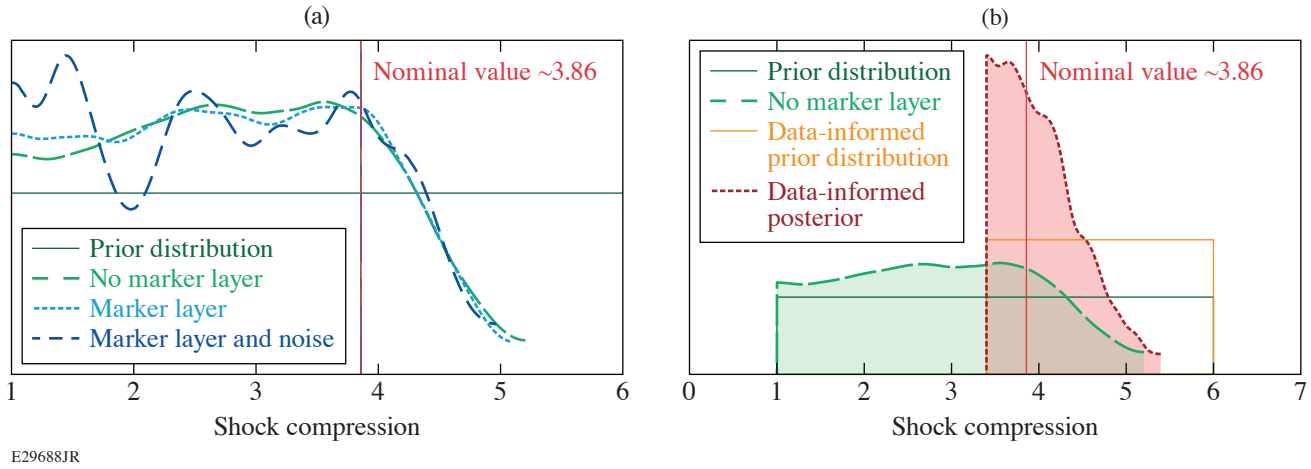

Figure 2

(a) Posterior distributions of the shock compression (ρ_s/ρ_0) for the cases with no noise and no Lagrangian marker layer (dashed green curve), no noise with a Lagrangian marker layer (dotted light blue curve), and with noise and a Lagrangian marker layer (dashed dark blue curve). Also shown are the prior used for each case (solid green, horizontal line) and the nominal value from the *LILAC* density profile (solid red, vertical line), given as ~3.86. All of the distributions show the same general trend that above a compression of 4 the probability density drops sharply, due to the peak compression behind the shock being well constrained and the shock jump necessarily being smaller, effectively giving an upper bound on the shock jump. There is little constraint on the lower end of the compression where the probability density is effectively flat between 1 and 4. The case with noise shows modal structure that, if point estimates are used, can give the impression of constraint while being only a local maximum in probability density. (b) The posterior for shock compression (dashed green curve) for the case with a broad uniform prior (solid green line) and posterior (dotted red curve) for the case with a narrow uniform prior (solid orange line) truncated at the low end at the location of previous measurements.[2] This demonstrates how Bayesian inference allows additional information to be leveraged to constrain a quantity that is otherwise unconstrained. The combination of the prior informing a lower limit of compression and the radiograph constraining upper limits of compression results in a nicely peaked posterior probability density that captures the proper underlying value (solid red line). The axes are expanded to demonstrate how the priors enforce that there is zero probability density outside of their bounds. Note that the data-informed posterior is largely asymmetric, although it presents a strongly peaked result that recovers the nominal value.

from previous data along the Hugoniot of CH up to 8.74 Mbar performed in planar geometry using a different methodology. Figure 2(b) also shows the posterior for shock compression given the new prior (red), which is now significantly more peaked than the previous results (green), meaning that there is a well-defined region of high probability density.

Although the shock compression is not strongly constrained by the radiograph alone, the density profile is well constrained by the radiograph measurement. In particular, the areal density (ρR) is very well constrained and is a quantity of particular interest within the ICF community. The findings here are in excellent agreement with previous radiography measurements taken on shells for the purpose of diagnosing metrics relevant to ICF modeling.[3] This work can be seen as an extension of those efforts with additional insight into the uncertainties associated with such reconstructions. Additionally, the peak density achieved within the bulk of the material behind the shock, which has a great effect on the propagation of the outgoing shock wave, is well constrained. Radiography measurements of this kind contain a great deal of information that can be used in combination with other measurements to develop a full picture of implosion experiments, including how materials respond to strong converging shock waves. This work can be used as a foundation to develop further investigations about the information contained in measurements of this type.

This material is based upon work supported by the Department of Energy National Nuclear Security Administration under Award Number DE-NA0003856, the U.S. Department of Energy, Office of Science, Office of Fusion Energy Sciences under Award No. DE-SC001926, the University of Rochester, and the New York State Energy Research and Development Authority.

1. D. C. Swift *et al.*, Rev. Sci. Instrum. **89**, 053505 (2018).
2. M. A. Barrios *et al.*, Phys. Plasmas **17**, 056307 (2010).
3. D. G. Hicks *et al.*, Phys. Plasmas **17**, 102703 (2010).

Diamond Formation in Double-Shocked Epoxy to 150 GPa

M. C. Marshall,[1] M. G. Gorman,[2] D. N. Polsin,[1,3] J. H. Eggert,[2] M. K. Ginnane,[1,3] J. R. Rygg,[1,3,4] G. W. Collins,[1,3,4] and L. D. Leininger[2]

[1]Laboratory for Laser Energetics, University of Rochester
[2]Lawrence Livermore National Laboratory
[3]Department of Mechanical Engineering, University of Rochester
[4]Department of Physics and Astronomy, University of Rochester

The formation of diamond from carbon-based polymers, compounds, or other carbon polymorphs (i.e., graphite) under extreme pressures has been actively researched for many decades.[1–12] Diamond can form by extreme heating and compression of some plastics,[1] methane,[2,3] and explosive materials.[10,12] For example, cubic diamond was detected from double-shocked polystyrene (CH) at 139 to 159 GPa using *in-situ* x-ray diffraction in experiments at the Linac Coherent Light Source (LCLS), indicating that breaking of the carbon and hydrogen bonds and restructuring of the carbon into diamond can occur over only nanosecond time scales.[1] The results presented here indicate that cubic diamond also forms from Stycast 1266 epoxy (C:H:Cl:N:O ≈ 27:38:1:1:5) (Ref. 13) doubly shocked to 80 and 148 GPa. These results demonstrate that the chemical and thermodynamic conditions inside ice giant planets, which have inner ice layers dominated by CH_4, NH_3, and H_2O, are suitable for diamond formation.

Two experiments were conducted on the OMEGA EP Laser System,[14] where laser beams were used to shock compress the target comprising an epoxy sample and a LiF window with a reflective Ti coating between them to measure the interface velocity using a velocity interferometer system for any reflector (VISAR).[15] When the shock wave is incident on the higher-impedance LiF interface, a return shock (reshock) is launched back through the epoxy, which approximately doubles the pressure. The target was probed with x rays, and the resulting diffraction pattern was measured using the powder x-ray diffraction image-plate diagnostic[16] when the epoxy was in the reshocked state. Diffraction consistent with cubic diamond was observed for both shots (Fig. 1). The pressure and temperature state during the x-ray exposure time were determined using hydrodynamic simulations matched to the measured epoxy/LiF interface velocity.

The results are compared to previous works in Fig. 1(a), where CH (Ref. 1), polyethylene (CH_2) (Ref. 5), methane (CH_4), (Refs. 2 and 3), and methane hydrate (MH) (Ref. 4) were also probed *in situ* at high pressures and temperatures to study diamond formation. Diamond formation from methane and methane hydrate is observed over ~10 to 80 GPa and ~2000 to 4000 K in laser-heated diamond-anvil cell experiments, where the samples are compressed and heated over seconds to hours.[2–4] At these conditions and compression rates, diamond formation is largely temperature dependent and the temperature threshold at which it occurs is lowered by the addition of oxygen as suggested by the methane hydrate experiments.[4] Diamond formation is not observed in singly shocked CH (Ref. 1) and CH_2 (Ref. 5) when they are compressed over nanoseconds at similar temperatures and pressures. While diamond still does not form in doubly shocked CH_2, it does form from doubly shocked CH and epoxy at ~80 to 200 GPa pressures and ~2000 to 6000 K temperatures. Diamond formation at these fast nanosecond times scales is not purely pressure or temperature dependent and is affected by the initial material composition and thermodynamic compression path (e.g., single versus double shock). These differences in behavior among all the experiments collectively suggest that the kinetics associated with the vastly different time scales, the thermodynamic path, and the chemical composition of the initial material play an important role in diamond formation at extreme conditions.

(a)

Diamond	No diamond	Initial material	Experiment type, time scale	
◆		Epoxy (C,H,O,N,Cl)	Laser shock, ~1 to 15 ns	Marshall (this work)
◆	+	CH	Laser shock, ~1 to 10 ns	Kraus[1]
	+ +	CH_2	Laser shock, ~1 to 10 ns	Hartley[5]
◆	+	MH (C,H,O)	LHDAC, ~10 to 120 min	Kadobayashi[4]
▭		CH_4	LHDAC, ~1 to 15 min	Benedetti[2]
▭		CH_4	LHDAC, ~10 s to 15 min	Hirai[3]

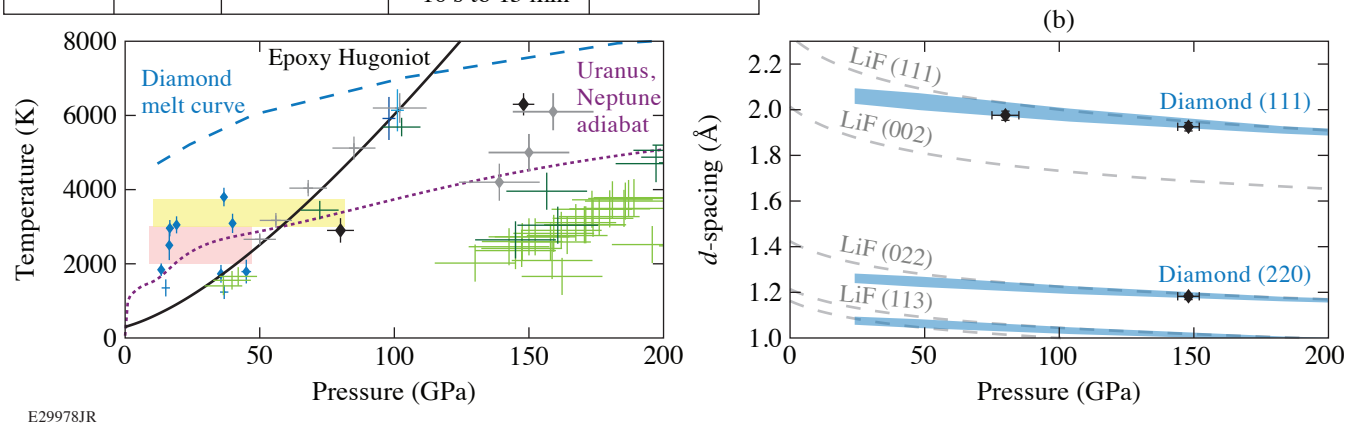

Figure 1
(a) Phase diagram showing diamond-formation results from compressed and heated epoxy, polystyrene (CH), polyethylene (CH_2), methane hydrate (MH), and methane (CH_4). Data points on singly shocked CH and CH_2 lie close to the epoxy Hugoniot (*SESAME* 7602). Data points from this work and all points above 120 GPa on CH and CH_2 are on doubly shocked samples. (b) Lattice *d*-spacing results from this work compared to predictions for compressed diamond (spanning the cold curve[17] to the melt curve[18] to encompass all possible temperature effects) and shocked LiF.

This material is based upon work supported by the Department of Energy National Nuclear Security Administration under Award Number DE-NA0003856, the University of Rochester, and the New York State Energy Research and Development Authority. This work was performed under the auspices of the U.S. Department of Energy by Lawrence Livermore National Laboratory (LLNL) under LLNL's Laboratory Directed Research and Development (LDRD) Program under Grant No. 18-SI-004. Lawrence Livermore National Laboratory is operated by Lawrence Livermore National Security, LLC, for the U.S. Department of Energy, National Nuclear Security Administration under Contract DE-AC52-07NA27344.

1. D. Kraus *et al.*, Nat. Astron. **1**, 606 (2017).
2. L. R. Benedetti *et al.*, Science **286**, 100 (1999).
3. H. Hirai *et al.*, Phys. Earth Planet. Inter. **174**, 242 (2009).
4. H. Kadobayashi *et al.*, Sci. Rep. **11**, 8165 (2021).
5. N. J. Hartley *et al.*, Sci. Rep. **9**, 4196 (2019).
6. D. Kraus *et al.*, Nat. Commun. **7**, 10970 (2016).
7. E. B. Watkins *et al.*, Sci. Rep. **12**, 631 (2022).
8. D. G. Morris, J. Appl. Phys. **51**, 2059 (1980).

9. F. H. Ree, J. Chem. Phys. **70**, 974 (1979).
10. M. van Thiel and F. H. Ree, J. Appl. Phys. **62**, 1761 (1987).
11. W. J. Nellis *et al.*, J. Chem. Phys. **75**, 3055 (1981).
12. J. B. Donnet *et al.*, Diam. Relat. Mater. **9**, 887 (2000).
13. We provide only an estimated C:H:Cl:N:O ratio for the final cured Stycast 1266 mixture, obtained by combining the listed components in the safety data sheets for Parts A and B by the quoted mix ratios and assuming a closed system. The exact composition of the Stycast 1266 Part A and B may vary from the quoted percentages or are trade secrets.
14. D. D. Meyerhofer *et al.*, J. Phys.: Conf. Ser. **244**, 032010 (2010).
15. P. M. Celliers *et al.*, Rev. Sci. Instrum. **75**, 4916 (2004).
16. J. R. Rygg *et al.*, Rev. Sci. Instrum. **83**, 113904 (2012).
17. A. Dewaele *et al.*, Phys. Rev. B **77**, 094106 (2008).
18. X. Wang, S. Scandolo, and R. Car, Phys. Rev. Lett. **95**, 185701 (2005).

Meta-GGA Exchange-Correlation Free Energy Density Functional to Increase the Accuracy of Warm-Dense-Matter Simulations

V. V. Karasiev, D. I. Mihaylov, and S. X. Hu

Laboratory for Laser Energetics, University of Rochester

High-energy-density physics includes a complicated warm-dense-matter (WDM) domain of state conditions that is characterized by elevated temperatures (from few to hundreds of eV) and pressures to 1 Mbar or greater. Accurate knowledge of equation of state, transport, and optical properties describing possible phase transitions (e.g., insulator-to-metal transition) across a warm dense regime plays an important role in planetary science, astrophysics, and inertial confinement fusion.[1–6] Currently, the vast majority of density-functional-theory (DFT) simulations of WDM and high-energy-density plasmas use the zero-temperature (ground-state) exchange-correlation (XC) functionals without explicit temperature dependence, which were developed by the condensed-matter physics and quantum chemistry communities, leading to neglect of thermal XC effects and degraded accuracy of predictions. The use of a ground-state XC functional is justified only at low electronic temperatures not exceeding a few tenths of the Fermi temperature or in the high-temperature limit when the XC contribution to the total free energy is negligible.[7–10] Recent development of the temperature-dependent Karasiev–Sjostrom–Dufty–Trickey (KSDT)[11] local-density approximation (LDA) (see Ref. 12 for the corrected set of parameters corrKSDT), the generalized gradient approximation (GGA)–type XC functional "KDT16" (Ref. 12), and the thermal hybrid KDT0[13] have shown that thermal XC effects are very important to increasing the accuracy of simulations at extreme conditions and improving agreement with experimental measurements as compared to the standard zero-temperature Perdew–Burke–Ernzerhof (PBE)[14] calculations. The way to improve overall accuracy of the thermal GGA XC functional is to use the next rung approximation at zero temperature and construct thermally extended meta-GGA XC.

In this work, we address this problem by developing a thermalization framework for XC functionals at the meta-GGA level of refinement and realization of a simple scheme via universal thermal XC additive correction at the GGA level of theory, which is applied to an accurate at low-T, ground-state meta-GGA XC. Thermal correction is applied to the ground-state deorbitalized, strongly constrained, and appropriately normed semilocal density functional (SCANL)[15–18]—to date, one of the most-accurate meta-GGA XC functionals, which, for example, is capable of accurately describing the liquid–liquid insulator-to-metal transition of warm dense hydrogen.[3] The resulting thermal meta-GGA XC functional, referred to here as T-SCAN-L, inherits the precision of the ground-state meta-GGA SCAN-L at low T, and most of the thermal XC effects are captured at the GGA level of theory, providing overall a much higher accuracy across the temperature regimes spanned by the WDM domain.

With increasing temperature, the electron density approaches the slowly varying regime. The KDT16 GGA functional, by construction, recovers the finite-T gradient expansion. Thermal XC corrections beyond the GGA level are expected to be small; therefore, in the following we propose a simple perturbative-like self-consistent approach via a universal thermal additive correction treated self-consistently, similar to the idea used in Ref. 19 to construct GGA XC with additive thermal LDA correction. The KDT16 XC free energy in the zero-T limit reduces to the ground-state PBE by construction:

$$\lim_{T\to 0} \mathcal{F}_{\mathrm{xc}}^{\mathrm{KDT16}}[n,T] \approx E_{\mathrm{xc}}^{\mathrm{PBE}}[n], \tag{1}$$

a choice driven by popularity of the PBE functional and by availability of pseudo-potentials and projector augmented wave (PAW) data sets generated by using the PBE XC. Given the quality of SCAN-L functional at zero temperature, we propose a simple temperature-dependent meta-GGA

$$\mathcal{F}_{\mathrm{xc}}^{\text{meta-GGA}}[n,T] = E_{\mathrm{xc}}^{\text{meta-GGA}}[n] + \Delta\mathcal{F}_{\mathrm{xc}}^{\mathrm{GGA}}[n,T], \tag{2}$$

with the additive thermal correction defined as follows:

$$\Delta\mathcal{F}_{\mathrm{xc}}^{\mathrm{GGA}}[n,T] := \mathcal{F}_{\mathrm{xc}}^{\mathrm{KDT16}}[n,T] - E_{\mathrm{xc}}^{\mathrm{PBE}}[n] \tag{3}$$

and meta-GGA = SCAN-L. An explicit functional form defined by Eqs. (2) and (3) is used in standard fully self-consistent DFT calculations with local XC potential calculated as a functional derivative of $\mathcal{F}_{\mathrm{xc}}^{\text{meta-GGA}}[n,T]$ with respect to electron density n.

Ab initio molecular dynamics (AIMD) simulations that demonstrate the superior accuracy of the new T-SCAN-L meta-GGA functional are for dense helium. Figure 1 compares relative errors for total pressures obtained from DFT simulations with four XC functionals and high-quality path-integral Monte Carlo (PIMC). PIMC is an efficient *first-principles* simulation technique for quantum systems at finite temperature that accurately takes into account the Coulombic interaction between electrons using pair-density matrices, so it therefore can be used to benchmark approximate XC density functionals at elevated temperatures.[7] Both ground-state functionals (PBE and SCAN-L) systematically overestimate the total pressure: the relative error with respect to the reference PIMC data is between 4.2% and 5.8% at T = 10.77 eV. In contrast, the T-SCAN-L total pressures are in excellent agreement with the PIMC values, demonstrating unprecedented accuracy between 0.05% and 0.35% for this range of densities. Relative differences between the KDT16 and PIMC values are larger as compared to the T-SCAN-L values and range from 0.4% to 1.4%. These comparisons show that T-SCAN-L calculations can improve the DFT simulation accuracy for He at these warm dense conditions by a factor of ~3 to 10 over the widely used XC functionals (PBE, SCANL, and KDT16). This clearly demonstrates that the T-SCAN-L meta-GGA functional can accurately capture combined XC thermal and nonhomogeneity effects. When temperature increases to 21.54 eV, the relative error of the ground-state functionals reduces to the range between 1.3% and 3.6% (because the XC contribution becomes less important as compared to the noninteracting free-energy term at high T), while the relative difference between T-SCAN-L and PIMC values is still less than ~1%.

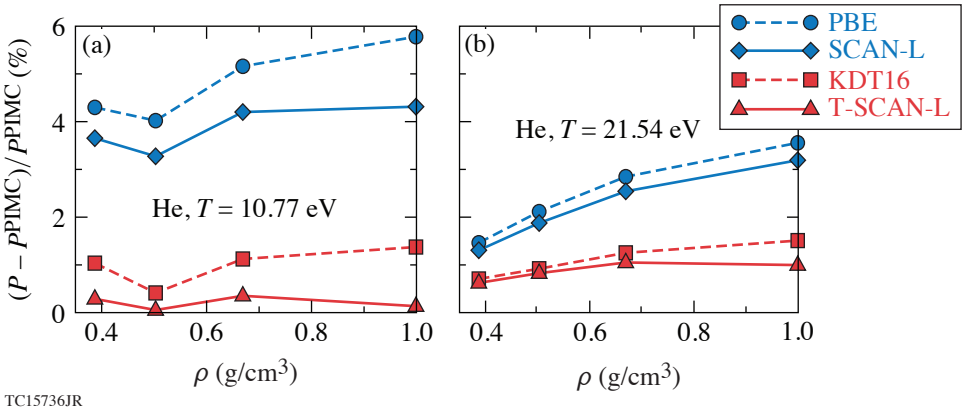

Figure 1
The relative error of total pressure from AIMD simulations of warm dense He using PBE, SCAL-L, KDT16, and T-SCAN-L XC functionals calculated with respect to the reference PIMC results and shown as a function of material density for two temperatures.

The simplest thermalization scheme, which uses a universal additive thermal correction and a perturbative-like self-consistent approach, has been implemented, leading to thermal T-SCAN-L functional. The nonempirical T-SCAN-L meta-GGA density functional takes into account combined thermal and nonhomogeneity effects at the meta-GGA level, providing a significantly higher accuracy for DFT to better predict material properties in the WDM regime, as compared to the thermal KDT16, and to the ground-state PBE and SCAN-L XC functionals. In the zero-temperature limit, T-SCAN-L reduces to its ground-state counterpart, therefore preserving the SCAN-L meta-GGA level of accuracy at low T.

This material is based upon work supported by the Department of Energy National Nuclear Security Administration under Award Number DE-NA0003856 and U.S. National Science Foundation PHY Grant No. 1802964. This research used resources of the National Energy Research Scientific Computing Center, a DOE Office of Science User Facility supported by the Office of Science of the U.S. Department of Energy under Contract No. DE-AC02-05CH11231.

1. J. J. Fortney and N. Nettelmann, Space Sci. Rev. **152**, 423 (2010).
2. W. Lorenzen, B. Holst, and R. Redmer, Phys. Rev. B **84**, 235109 (2011).
3. J. Hinz *et al*., Phys. Rev. Research **2**, 032065(R) (2020).
4. C. A. Iglesias, F. J. Rogers, and D. Saumon, Astrophys. J. Lett. **569**, L111 (2002).
5. S. X. Hu *et al*., Phys. Plasmas **22**, 056304 (2015).
6. V. V Karasiev and S. X. Hu, Phys. Rev. E **103**, 033202 (2021).
7. V. V. Karasiev, L. Calderín, and S. B. Trickey, Phys. Rev. E **93**, 063207 (2016).
8. V. V. Karasiev, S. B. Trickey, and J. W. Dufty, Phys. Rev. B **99**, 195134 (2019).
9. K. Ramakrishna, T. Dornheim, and J. Vorberger, Phys. Rev. B **101**, 195129 (2020).
10. M. Bonitz *et al*., Phys. Plasmas **27**, 042710 (2020).
11. V. V. Karasiev *et al*., Phys. Rev. Lett. **112**, 076403 (2014).
12. V. V. Karasiev, J. W. Dufty, and S. B. Trickey, Phys. Rev. Lett. **120**, 076401 (2018).
13. D. I. Mihaylov, V. V. Karasiev, and S. X. Hu, Phys. Rev. B **101**, 245141 (2020).
14. J. P. Perdew, K. Burke, and M. Ernzerhof, Phys. Rev. Lett. **77**, 3865 (1996); **78**, 1396(E) (1997).
15. J. Sun, A. Ruzsinszky, and J. P. Perdew, Phys. Rev. Lett. **115**, 036402 (2015).
16. H. Peng *et al*., Phys. Rev. X **6**, 041005 (2016).
17. D. Mejia-Rodriguez and S. B. Trickey, Phys. Rev. A **96**, 052512 (2017).
18. D. Mejia-Rodriguez and S. B. Trickey, Phys. Rev. B **98**, 115161 (2018).
19. T. Sjostrom and J. Daligault, Phys. Rev. B **90**, 155109 (2014).

Unveiling the Nature of the Bonded-to-Atomic Transition in Liquid SiO_2 to TPa Pressures

S. Zhang,[1] M. A. Morales,[2,3] R. Jeanloz,[4] M. Millot,[3] S. X. Hu,[1] and E. Zurek[5]

[1]Laboratory for Laser Energetics, University of Rochester
[2]Center for Computational Quantum Physics, Flatiron Institute
[3]Lawrence Livermore National Laboratory
[4]Departments of Earth and Planetary Science and Astronomy, University of California, Berkeley
[5]Department of Chemistry, State University of New York at Buffalo

SiO_2 is an important compound for theory, basic science, and technology, including as a laboratory standard for high-energy-density experiments. As a key constituent of Earth, terrestrial, and even giant planets, the response of SiO_2 to dynamic compression helps to determine (1) how planets form through giant impacts and (2) the high pressure–temperature material properties that control, for example, how the deep interiors of planets evolve.

Laser and magnetically driven experiments and first-principles calculations over the past two decades[1–12] have provided important constraints on the high-temperature phase diagram and properties of SiO_2 and established it as a standard for impedance matching at up to 1.2 TPa. Questions remain, however, about the liquid structure of SiO_2 at extreme conditions,[8,13–15] the understanding of which not only helps to clarify phase transitions and metallization that generally occurs in materials under significant compression but can also shed light on material transport properties (e.g., electrical and thermal conductivity) critical to modeling the dynamics of the magma ocean and magnetic-field generation in early Earth and super-Earth exoplanets, as well as for numerical simulations of giant impacts.

We have performed extensive simulations from first principles and in-depth analysis of the structure, electron density, and thermodynamic properties of liquid SiO_2 to gain insights into the nature of the bonded-to-atomic transition. Our results show that a heat capacity anomaly happens at 2 to 3×10^4 K (1.5 to 2.5 eV) over the pressure range of 0.1 to 1 TPa, coinciding with conditions where the lifetime of Si–O bonds equals 50 fs. This corresponds to bonded-to-atomic liquid transition temperatures that are lower and more sensitive to pressure than previous estimates based on laser-driven Hugoniot measurements (black line with diamonds versus gray dashed curve in Fig. 1). These results render a new bonded-to-atomic boundary of liquid SiO_2 that overlaps with the conditions of interest to giant-impact simulations, which indicates more-complex variations (i.e., a decrease and then an increase with temperatures) in heat capacity than that considered previously. This can rebalance the dissipation of irreversible work into temperature and entropy in events of giant impact, necessitating reconsideration of predictions by simulations that are based on empirical equation-of-state (EOS) models.

Furthermore, our calculated Hugoniots show overall agreement with experimental ones (see Fig. 1) and are similar to previous calculations using similar methods.[4,8,9,14] The discrepancies between theory and experiment in the stishovite temperature–pressure Hugoniot near melting, together with the previously shown inconsistencies at 1.0 to 2.5 TPa, emphasize the need for further development in both numerical simulations and dynamic compression experiments to improve constraints on the phase diagram, EOS, and properties of SiO_2 in regions off the Hugoniots of α-quartz and fused silica and elucidate the exotic behaviors affecting matter at extreme conditions. These include simulations that overcome the increased limitations of pseudopotentials and computational cost for reaching convergence at the high density/temperature conditions or go beyond LDA/GGA (local density approximation/generalized gradient approximation) for the exchange-correlation functional, as well as more in-depth experimental

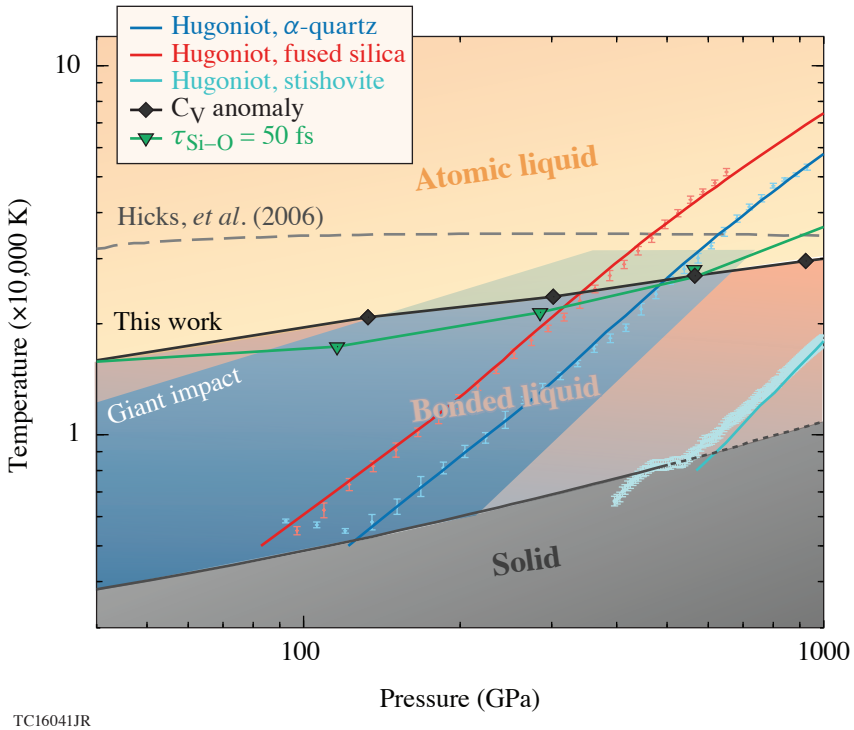

Figure 1
Phase diagram of SiO_2 featuring the bonded-to-atomic liquid transition determined in this work (black curve with diamond symbols) as compared to a previous estimation (Hicks *et al.*,[1] gray dashed curve). Also shown are the conditions for Si–O bond lifetime equaling 50 fs (green line with triangles), Hugoniots from this work (solid curves in red, blue, and turquoise for fused silica, α-quartz, and stishovite, respectively) in comparison to experiments[1,2] (lighter-colored symbols), the melting curve (solid dark-gray curve: measured; dashed dark-gray curve: extrapolated) from Millot *et al.*,[2] and the conditions of interest (blue shaded area) to giant impacts.[16]

studies, currently lacking benchmarking u_s–u_p data for stishovite between 0.2 and 1.2 TPa and relying on pyrometry and a gray-body approximation for temperature estimation.

This material is based upon work supported by the Department of Energy National Nuclear Security Administration under Award Number DE-NA0003856, the University of Rochester, and the New York State Energy Research and Development Authority.

1. D. G. Hicks *et al.*, Phys. Rev. Lett. **97**, 025502 (2006).
2. M. Millot *et al.*, Science **347**, 418 (2015).
3. M. D. Knudson and M. P. Desjarlais, Phys. Rev. B **88**, 184107 (2013).
4. T. Qi *et al.*, Phys. Plasmas **22**, 062706 (2015).
5. M. D. Knudson and R. W. Lemke, J. Appl. Phys. **114**, 053510 (2013).
6. C. A. McCoy *et al.*, J. Appl. Phys. **119**, 215901 (2016); **120**, 235901 (2016).
7. M. C. Marshall *et al.*, Phys. Rev. B **99**, 174101 (2019).
8. S. Root, J. P. Townsend, and M. D. Knudson, J. Appl. Phys. **126**, 165901 (2019).
9. T. Sjostrom and S. Crockett, AIP Conf. Proc. **1793**, 050010 (2017).
10. M. Li *et al.*, Phys. Rev. Lett. **120**, 215703 (2018).
11. M. Guarguaglini *et al.*, Nat. Commun. **12**, 840 (2021).
12. F. Soubiran and B. Militzer, Nat. Commun. **9**, 3883 (2018).
13. R. G. Kraus *et al.*, J. Geophys. Res. Planets **117**, E09009 (2012).
14. R. Scipioni, L. Stixrude, and M. P. Desjarlais, Proc. Nat. Acad. Sci. **114**, 9009 (2017).
15. E. C. R. Green, E. Artacho, and J. A. D. Connolly, Earth Planet. Sci. Lett. **491**, 11 (2018).
16. R. M. Canup, Icarus **168**, 433 (2004).

A Case Study of Using X-Ray Thomson Scattering to Diagnose the In-Flight Plasma Conditions of DT Cryogenic Implosions

H. Poole,[1] D. Cao,[2] R. Epstein,[2] I. Golovkin,[3] T. Walton,[3] S. X. Hu,[2] M. Kasim,[1] S. M. Vinko,[1] J. R. Rygg,[2] V. N. Goncharov,[2] G. Gregori,[1] and S. P. Regan[2]

[1]Department of Physics, University of Oxford
[2]Laboratory Laboratory for Laser Energetics, University of Rochester
[3]Prism Computational Sciences

The design of inertial confinement fusion ignition targets requires radiation-hydrodynamic simulations with accurate models of the fundamental material properties (i.e., equation of state, opacity, and conductivity). Validation of these models are required via experimentation. A feasibility study of using spatially integrated, spectrally resolved, x-ray Thomson-scattering (XRTS) measurements to diagnose the temperature, density, and ionization of the compressed DT shell of a cryogenic DT implosion at two-thirds convergence was conducted. This study involved analyzing the x-ray scattering data produced by targets with very different adiabats, specifically 2.8 and 8.0, to determine if their conditions were distinguishable.

Synthetic scattering spectra were generated using 1-D implosion simulations from the *LILAC* code[1] that were post-processed with the x-ray scattering model, which is incorporated within *Spect3D*.[2] To model the x-ray emissivity, a 1-kJ laser with a 10-ps pulse length and a source diameter of 50 μm was used to produce a Gaussian x-ray source, with a FWHM of 10 eV (Ref. 3). The scattering geometry is shown in Fig. 1. The detectors captured scattering data at $\theta_F = 40°$ and $\theta_B = 120°$. Two x-ray photon energies, 2 keV and 3.5 keV, were considered.

Using the output spectra from *Spect3D*, synthetic experimental data were produced by assuming a detector efficiency of $\Gamma_{det} \sim 10^{-5}$ and a spectral resolution of 3 eV/bin, which gives ~300 inelastically scattered photons resolved by the detector. Synthetic experimental noise was added by removing the uniform background signal and using the Poisson statistic, which estimates the noise as $\sim 1/N_t$, where N_t is the number of photons per spectral resolution element.

Before extracting the plasma parameters from the spatially integrated simulated spectra, the inverse problem instability must first be addressed, which implies that the same measured spectra could be fitted equally well by very different plasma parameters. Bayesian inference, using Markov–Chain Monte Carlo (MCMC) to sample the multidimensional space, is a more-robust approach to exploring the behavior of the complex multiparameter simulations.[4]

The MCMC exploration fit the entire spectra, assuming two weighted uniform plasma regions, one containing DT and the other CH. The cost function used to determine the appropriateness of each MCMC spectrum calculates the maximum percentage error to allow equal weighting of the fitting to the elastic and inelastic peaks between the MCMC spectrum I_{fit}, and the synthetic experimental spectra I_{raw},

$$\beta_{cost} = \max\left(\frac{I_{fit} - I_{raw}}{I_{raw}} \frac{1}{\sqrt{2}\,\sigma}\right)^2,$$

where σ is the standard deviation representative of the noise of the synthetic scattering spectra. The σ is selected such that the noise of the scattering signal falls comfortably within the spread of the accepted fits. A value of 0.075 was chosen. The forward-

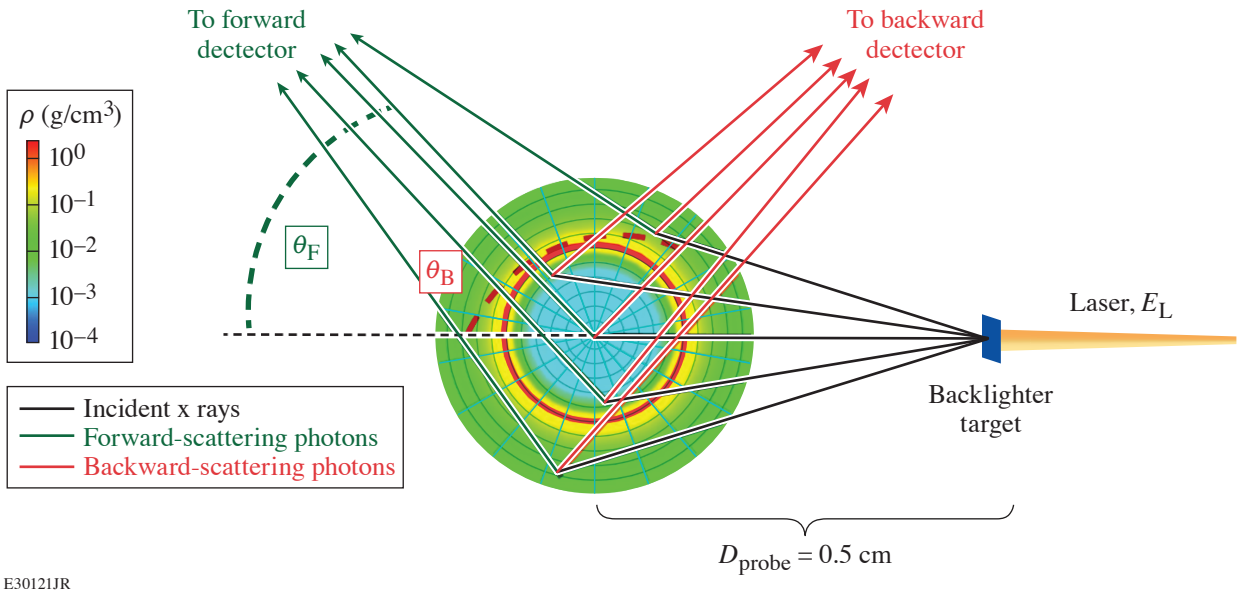

Figure 1
A sketch of the proposed experimental setup, with a laser of energy E_L incident on a backlighter target, producing x rays with a conversion efficiency of η_x. The scattering x rays are shown incident on the 3-D inferred density profile from *Spect3D* using the 1-D simulation data produced by the *LILAC* code. A schematic of the scattering events, recorded on the detector by *Spect3D*, from different zones throughout the implosion, is shown. The scattering geometry is demonstrated and not drawn to scale.

and backward-scattering spectra were analyzed separately, and their parameter distributions were combined to produce an overall distribution for each plasma parameter. The distributions for each adiabat and x-ray photon energy are shown in Table I.

Good agreement was found between the mass-averaged simulation parameter values and the MCMC distributions. There is, predictably, very little information regarding the CH plasma. This is due to its lower density compared to the DT compressed shell, meaning it does not contribute to the overall shape of the scattering. Overall, the optimum analysis presented in this summary to resolve the plasma conditions in the compressed shell, using a realistic laser probe from OMEGA EP, is performing MCMC analysis from spectra produced using a backward fielding detector. Since the collective forward-scattering detector is not required for sufficient convergence on the DT compressed shell parameters, either a 2-keV or 3.5-keV x-ray photon energy probe could be used. Better agreement may be achieved between the MCMC parameters and the simulations if a narrower bandwidth probe beam could be used.

Table I: The full spectral analysis of MCMC DT fitting parameters compared to the mass-weighted parameters from the *LILAC* 1-D simulations, focused on the compressed DT shell, for each adiabat and each probe.

DT parameter	T_e	n_e (cm^{-3})	Z
Adiabat = 2.8			
Simulation	25	5.5×10^{23}	0.97
MCMC 2 keV	33±8	$(5.2\pm0.6) \times 10^{23}$	0.94±0.03
MCMC 3.5 keV	25±3	$(5.0\pm0.3) \times 10^{23}$	0.95±0.03
Adiabat = 8.0			
Simulation	38	3.7×10^{23}	0.97
MCMC 2 keV	50±6	$(2.6\pm0.4) \times 10^{23}$	0.88±0.07
MCMC 3.5 keV	56±6	$(3.2\pm0.5) \times 10^{23}$	0.87±0.05

In summary, spatially integrated XRTS spectra for 1-D *LILAC*-simulated conditions of low- and high-adiabat, DT cryogenic implosions have been calculated at two-thirds convergence. Markov–Chain Monte Carlo analysis was performed for two different scattering setups. Information on the compressed shell conditions was obtained since it has been shown to be possible to use the spectral resolution in a spatially integrated measurement to discriminate between different regions in the plasma. Fielding just one detector in the noncollective scattering regime produces good agreement with the compressed shell mass-averaged parameters from the simulation. This technique can be used to resolve both the low- and high-adiabat implosions. In the future, similar analysis will be performed on the conditions at stagnation, the effect of mixing in the implosion, as well as investigations into 2-D and 3-D simulations using *DRACO* and *ASTER*.

This material is based upon work supported by the Department of Energy National Nuclear Security Administration under Award Number DE-NA0003856, the University of Rochester, and the New York State Energy Research and Development Authority.

1. J. Delettrez *et al.*, Phys. Rev. A **36**, 3926 (1987).
2. I. Golovkin *et al.*, High Energy Density Phys. **9**, 510 (2013).
3. C. Stoeckl *et al.*, Rev. Sci. Instrum. **85**, 11E501 (2014).
4. M. F. Kasim *et al.*, Phys. Plasmas **26**, 112706 (2019).

Interdigitated Electrode Geometry Variation and External Quantum Efficiency of GaN/AlGaN-Based Metal–Semiconductor–Metal Ultraviolet Photodetectors

S. F. Nwabunwanne and W. R. Donaldson

Laboratory for Laser Energetics
Department of Electrical and Computer Engineering, University of Rochester

Efficient and ultrafast $Al_xGa_{1-x}N$-based ultraviolet (UV) photodiodes are suitable candidates for UV photodetection because of their highly mobile carriers. The characteristics of $Al_xGa_{1-x}N$, a group III–V compound that has endeared it to the optoelectronics community, consist of a tunable direct band gap, superior electrical stability, elevated thermal resistivity, and robust performance in hazardous environments like inertial confinement chambers and space environments. $Al_xGa_{1-x}N$-based photodiodes (PD's) offer an important feature that permits the selection of a desired spectral window by simply altering the percentage composition of Al in the $Al_xGa_{1-x}N$ compound.[1,2]

AlGaN-based PD's produce the best response speed in the metal–semiconductor–metal (MSM) configuration because in this design, the response time is limited by the carrier transit time between the interdigitated fingers. Furthermore, in the MSM setup, the capacitance due to the interdigitated fingers is extremely small, of the order of 20×10^{-15} F, which leads to an ~1-ps resistor capacitor time constant for a 50-Ω external coupling circuit.[3]

Here, we discuss the successful design and fabrication of $Al_xGa_{1-x}N$-based photodetectors with rectangular and circular asymmetric, interdigitated electrode geometries GaN/AlGaN semiconductors. The thin films were grown on commercially available sapphire substrates via metal-organic chemical vapor deposition by KYMA Technologies.[4] The best-performing devices yielded a scope-limited pulse duration of 62 ps with a 29-ps rise time. The bias-independent external quantum efficiency of the devices was >70% for intrinsic devices at 60 V and >400% at 10 V. The main goal of this investigation was to establish the bias voltage that saturates the external quantum efficiency (EQE) of these devices.

Figure 1 depicts the device's epitaxial structure for both metals that were employed in the detectors. The experimental setup is shown in Fig. 2. UV light was produced by Astrella and an optical parametric amplifier (OPA) by a fourth-harmonic–generation technique. Astrella is an 800-nm Coherent laser operating at 1 kHz and possessing a 30-fs pulse duration. The 800-nm visible

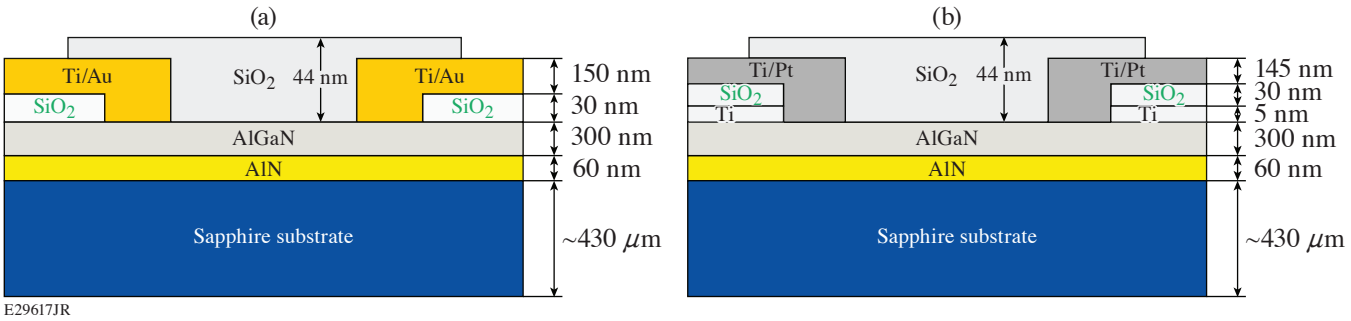

Figure 1
Epitaxial stack of the fabricated (a) Au and (b) Pt AlGaN-based MSM UV PD's for efficient and ultrafast UV detection.

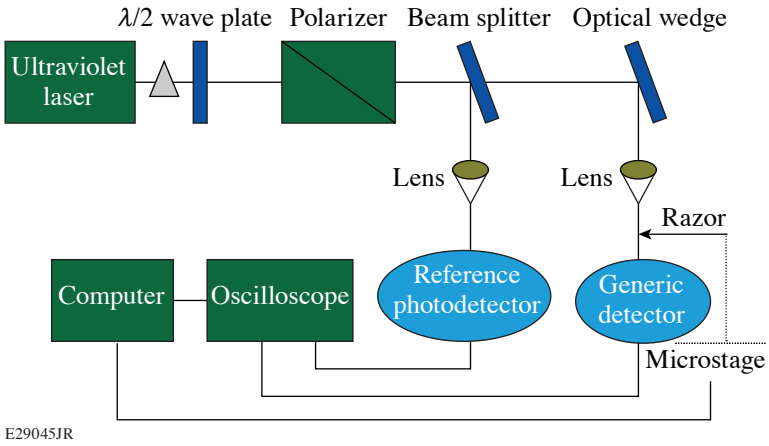

Figure 2
Experimental setup for ultrafast testing of AlGaN PD's at 262 nm (Ref. 1).

light output of Astrella served as the input pump laser to the OPA, which changes it to 262 nm of UV light using fourth-harmonic generation. The output energy per pulse from the OPA at 262 nm is 40×10^{-6} J, but only 0.749×10^{-9} J reached the detector under test. The reference detector was a 200- to 1100-nm Thorlab Det10 Si-biased detector.

Figure 3(a) posits the photocurrent of Pt intrinsic $Al_{0.2}Ga_{0.8}N$ with the circular asymmetric contact device as a function of bias voltage. The Schottky contact blocks current from –3.5 V to +3.5 V.

Figure 3(b) depicts the ultrafast impulse response function of Au $Al_{0.1}Ga_{0.9}N$ and Pt $Al_{0.2}Ga_{0.8}N$ intrinsic MSM UV photodiodes at 20-V bias voltage. The Au PD recorded a 29-ps rise time with 62-ps pulse duration, while the Pt PD showed a 34-ps rise time and 72-ps pulse width. The Au device exhibited the best response characteristics with a 29-ps rise time with 62-ps full width at half maximum; this response is not the intrinsic response time of the device due to the bandwidth limitation of the oscilloscope.

$$\mathrm{QE}(\eta) = \frac{I_{\mathrm{ph}}/e}{P/hv}. \tag{1}$$

The efficiency of the devices was computed using Eq. (1) and the results for Pt $Al_{0.1}Ga_{0.9}N$ *n*-doped circular asymmetric (CA) and Pt $Al_{0.2}Ga_{0.8}N$ intrinsic rectangular asymmetric (RA) detectors are plotted in Figs. 3(c) and 3(d), respectively.

The interdigitated electrode geometries of $Al_xGa_{1-x}N$ MSM UV photodiodes were redesigned as rectangular asymmetric and circular asymmetric fingers. These were successfully implemented and tested to establish their UV response profiles. Investigations were done to obtain the bias voltage that saturates these devices to find the detector's bias-independent EQE. The alterations of electrode geometry in addition to fewer electrodes on the devices reduced the effects of electrode shadowing and allowed about 34% more UV light to be absorbed. A combination of these factors resulted in the recorded bias-voltage–independent EQE of our devices. Establishment of the efficiency of these detectors will improve the quest for semiconductor-driven ultrafast laser pulse characterization and plasma diagnostics.

This material is based upon work supported by the Department of Energy National Nuclear Security Administration under Award Number DE-NA0003856, the University of Rochester, and the New York State Energy Research and Development Authority.

1. S. Nwabunwanne and W. Donaldson, Proc. SPIE **12001**, 120010F (2022).
2. E. Monroy *et al.*, Appl. Phys. Lett. **74**, 3401 (1999).
3. Y. Zhao and W. R. Donaldson, IEEE J. Quantum Electron. **56**, 4000607 (2020).
4. AlGaN Templates, Kyma Technologies Inc., Raleigh, NC 27617, accessed 10 June 2022, https://kymatech.com/products-services/materials/gan-related-iii-n-materials/499-algan-templates.

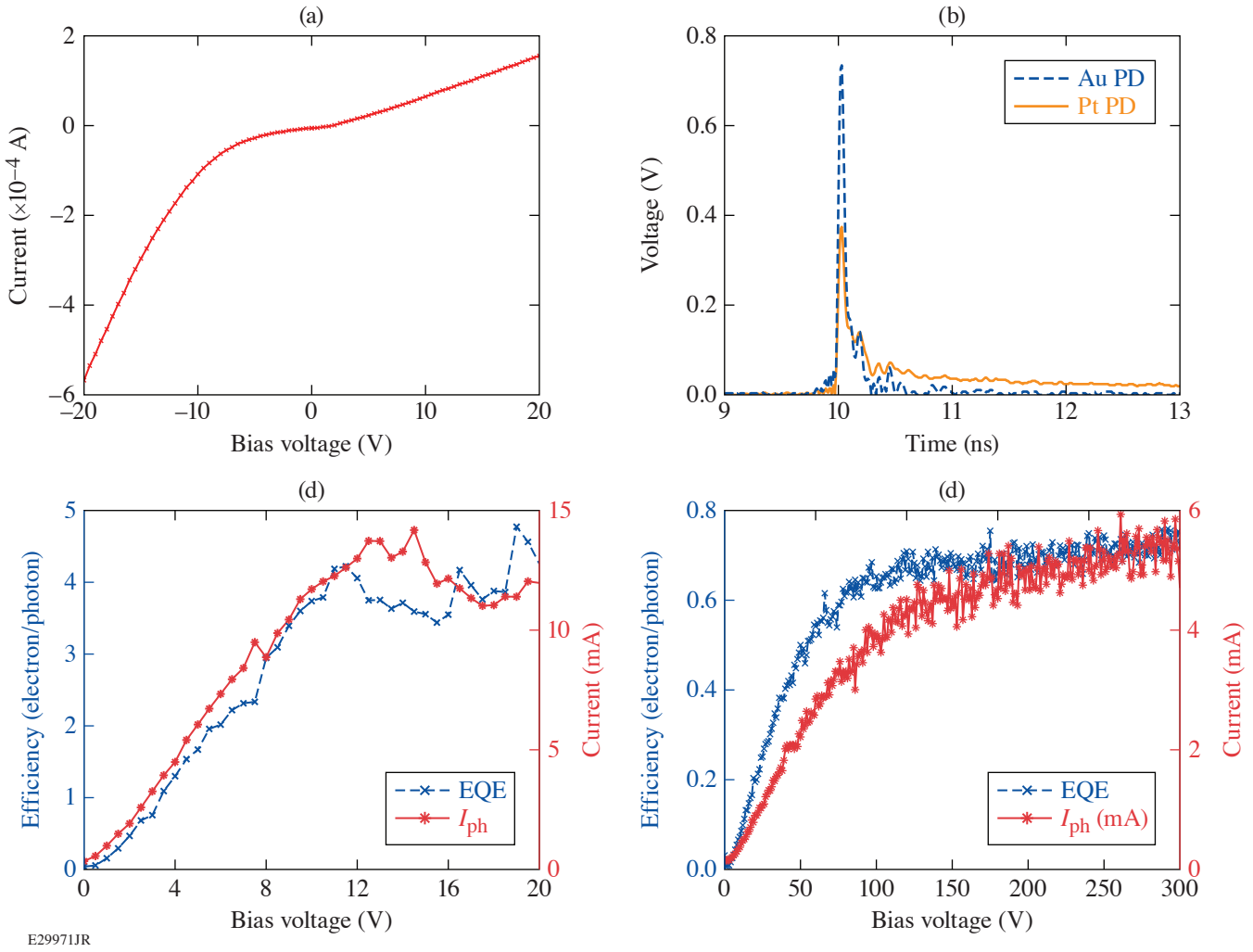

Figure 3

(a) Pt intrinsic $Al_{0.2}Ga_{0.8}N$ MSM UV photodiode I–V curve under dark conditions. (b) Au $Al_{0.1}Ga_{0.9}N$ and Pt $Al_{0.2}Ga_{0.8}N$ intrinsic MSM UV photodiodes' impulse response function at 20-V bias voltage. The Au PD yielded a 29-ps rise time with 62-ps pulse duration, while the Pt PD produced a 34-ps rise time and 72-ps pulse width. External quantum efficiency and photocurrent as a function of bias voltage. (c) Pt $Al_{0.1}Ga_{0.9}N$ *n*-doped CA device (saturation began at 10 V). (d) Pt $Al_{0.2}Ga_{0.8}N$ intrinsic RA device (saturation began at 60 V).

Impact of the Optical Parametric Amplification Phase on Laser Pulse Compression

J. Musgrave[1] and J. Bromage[2]

[1]Institute of Optics, University of Rochester
[2]Laboratory for Laser Energetics, University of Rochester

Optical parametric chirped-pulse amplification (OPCPA) has been widely used to provide high gain over broad bandwidths suitable for sub-20-fs pulses with multijoule energies, corresponding to petawatt peak powers.[1–3] Precise control and measurement of a system's spectral and spatial phases are required for Fourier transform–limited pulse compression and diffraction-limited focusing, respectively. Phase accumulated during optical parametric amplification (OPA) can degrade the compressibility and focusability of the pulse, reducing peak intensity. OPA is a three-wave mixing process where energy is transferred from a strong pump wave to a weak signal wave with the production of a third wave, called the "idler," to conserve energy and momentum. For efficient energy transfer, this process must be phase matched. Significant phase mismatch leads to reduction in gain and, as shown by Bahk,[4] can lead to signal phase accumulation. In this summary, we investigate signal phase accumulation from pump wavefront errors and evaluate the potential impact on signal pulse compression.

Broadband phase matching can be achieved by matching the group velocity of the signal and idler pulses using the amplifier material's birefringence and a noncollinear angle between the pump and signal.[5,6] Figure 1 shows relative orientation of the pump, signal, and idler k vectors to the crystal axis (O), with a noncollinear angle α.

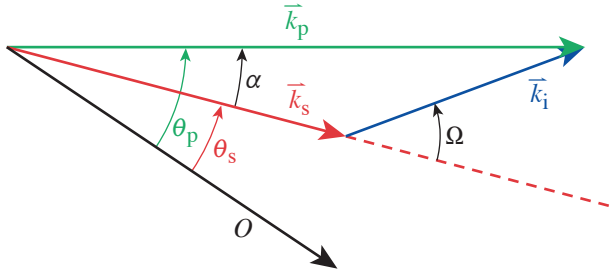

Figure 1
Phase matching between the wave vectors of the three beams: pump, signal, and idler. O is the optical axis of the nonlinear crystal.

The phase mismatch in the z direction is given by Eq. (1):

$$\Delta k = k_p \cos(\alpha) - k_s - \sqrt{k_p^2 \cos^2(\alpha) - k_p^2 + k_i^2}\,. \tag{1}$$

The sensitivity to pointing, caused either by global angular errors or local from wavefront aberrations, is given by the derivatives with respect to θ_p or θ_s for the pump and signal, respectively.[7] The resulting signal phase errors can be expressed analytically for the small-signal case or calculated numerically for higher-efficiency amplifiers.[7] In particular, modification of the signal spectral phase $\phi_s(\omega)$, an important parameter for determining pulse compression, can be evaluated for a range of pump and signal angular deviations from the optimum phase-matched condition.

As a test case, we chose the final amplifier of the Multi-Terawatt optical parametric amplifier line (MTW-OPAL), all-OPCPA system.[3] This amplifier uses 70% deuterated potassium dihydrogen phosphate (DKDP) crystals pumped by the second harmonic

of MTW to amplify 1.5-ns pulses centered at 920 nm with 140-nm bandwidths up to 11 J before recompression to sub-20 fs. For amplification, the pulse is chirped before the amplifier to 100,000× the Fourier transform limit; therefore, the interaction between the pump and the 140-nm-wide signal at a given time is essentially monochromatic. The sensitivity of the signal phase for this amplifier for a given angular error of the signal or pump is shown in Figs. 2(a) and 2(b), respectively. Curves for deuteration levels ranging from 70% to 100% are shown—the maximum range suitable for this system; they can be adjusted during the crystal growth with the relative amounts of hydrogen and deuterium. Changing the deuteration level requires changing the noncollinear angle α for optimum phase matching.[8] This, in turn, affects the phase-mismatch sensitivity and therefore the sensitivity of the signal phase to angular deviation. In the case of pump deviation [Fig. 2(a)], reducing the deuteration level causes an increase in pump-deviation sensitivity; for signal deviation [Fig. 2(b)], the opposite holds.

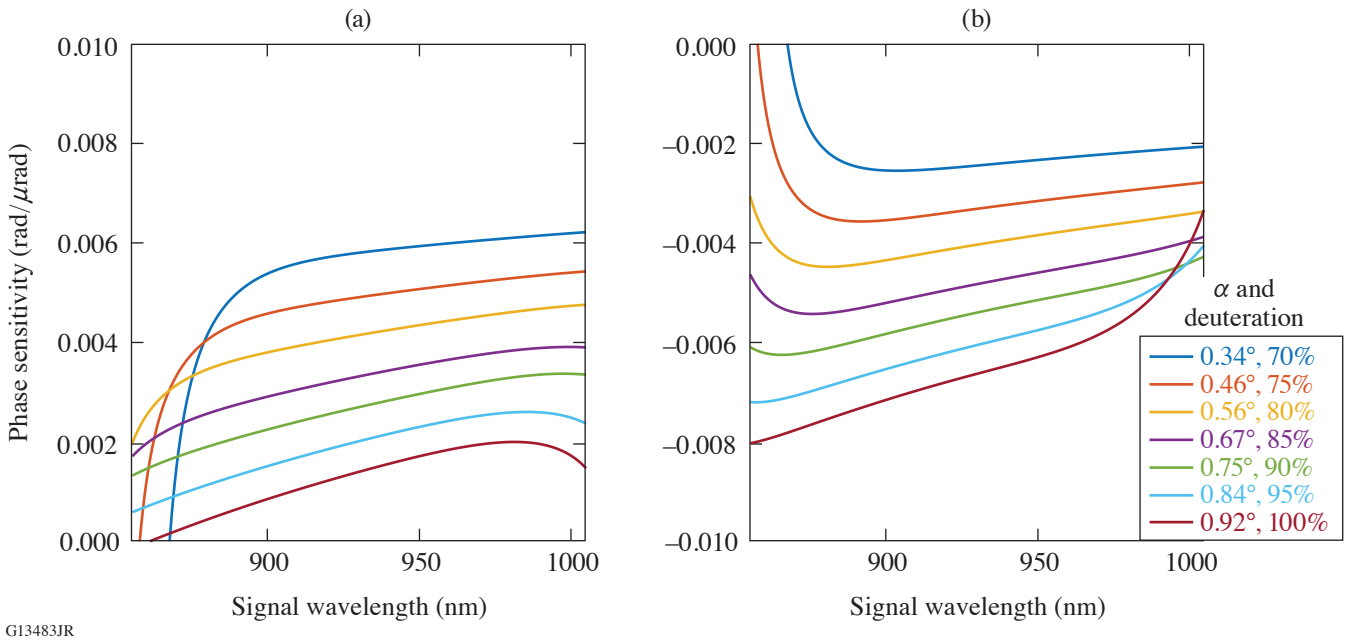

Figure 2
(a) Pump and (b) signal phase sensitivity across the signal wavelength for different deuteration levels and corresponding noncollinearity.

One point to note is that the phase sensitivity (in units of radians per microradian) is small but not zero and, in particular, can vary significantly across the signal bandwidth from 830 to 1010 nm. This variation in phase—a spectral phase error—can be problematic when it also has a spatially varying component, as would happen if the pump or signal angles vary locally. A number of cases were evaluated,[7] one of which is shown in Fig. 3, where the pump wavefront produces a local angular error of 500 μrad. This would produce a reduction in gain by ~50%, leading to local beam profile distortion. It would also change the local pulse (as shown in Fig. 3) with a shift of ~5 fs that, averaged over the beam profile, could cause a pulse broadening in the focal plane. Thankfully, in the case of the MTW-OPAL Laser System, wavefront slopes of this magnitude are not present and phase plates must be added to produce these effects.[9] Nonetheless, this analysis is valuable in determining the suitability of a given pump laser to ensure there are no spatiotemporal pulse-broadening effects that degrade the peak intensity achieved by the laser.

This material is based upon work supported by the Department of Energy National Nuclear Security Administration under Award Number DE-NA0003856, the University of Rochester, and the New York State Energy Research and Development Authority.

1. A. Dubietis, G. Jonusauskas, and A. Piskarskas, Opt. Commun. **88**, 437 (1992).
2. V. V. Lozhkarev *et al.*, Laser Phys. Lett. **4**, 421 (2007).
3. J. Bromage *et al.*, High Power Laser Sci. Eng. **9**, e63 (2021).
4. S. W. Bahk, Opt. Lett. **46**, 5368 (2021).

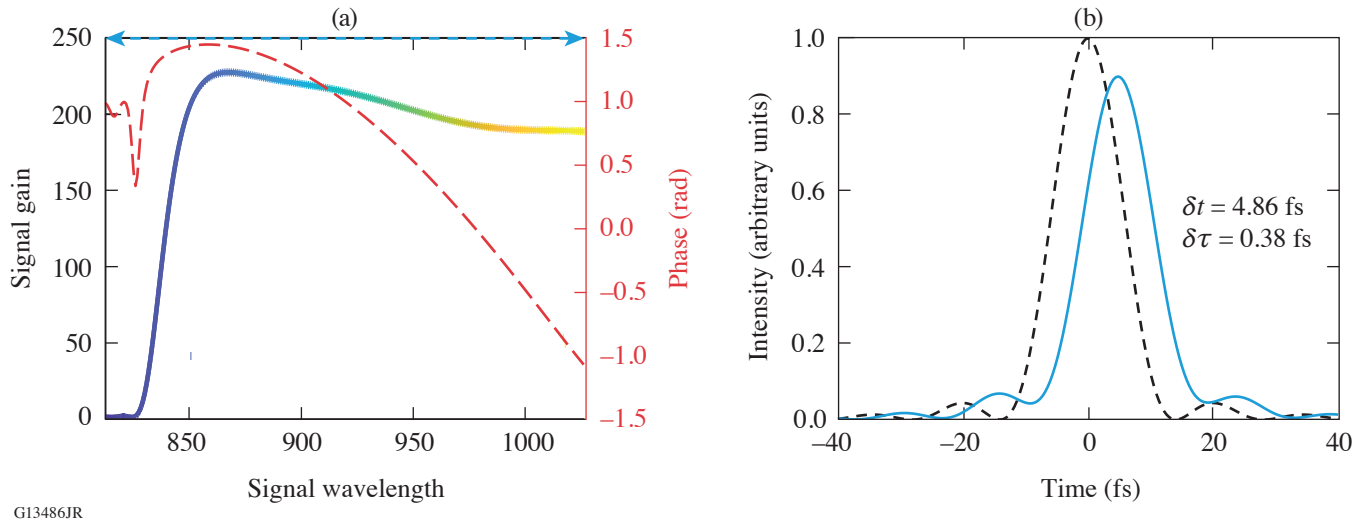

Figure 3
(a) Impact of angular error on signal gain and spectral phase. (b) Impact on the compressed pulse assuming equivalent gain across the spectrum (to show spectral phase effects). δt is the temporal shift of the peak, and $\delta\tau$ is the change in pulse full width at half maximum from the nominal 13 fs.

5. G. M. Gale *et al.*, Opt. Lett. **20**, 1562 (1995).
6. G. Cerullo and S. De Silvestri, Rev. Sci. Instrum. **74**, 1 (2003).
7. J. Musgrave and J. Bromage, Appl. Opt. **61**, 3838 (2022).
8. K. Fujioka *et al.*, J. Appl. Phys. **117** (9), 093103 (2015); **119**, 249902(E) (2016).
9. S. W. Bahk *et al.*, Opt. Express **30**, 12,995 (2022).

Simultaneous Contrast Improvement and Temporal Compression Using Divided-Pulse Nonlinear Compression

G. W. Jenkins,[1,2] C. Feng,[1] and J. Bromage[1]

[1]Laboratory for Laser Energetics, University of Rochester
[2]Institute of Optics, University of Rochester

Temporal contrast is an increasingly important specification for high-energy, ultrafast lasers because prepulses with only a fraction of a percent of the main pulse's energy can ionize the laser's target and modify experimental conditions before the main pulse arrives. To remove the prepulses, many temporal contrast improvement methods have been developed. We are particularly interested in methods such as nonlinear ellipse rotation (NER)[1] that allow simultaneous contrast improvement and spectral broadening.[2,3] Yb laser technology suffers from relatively long pulses (of the order of hundreds of femtoseconds to picoseconds) and requires temporal compression to efficiently pump many applications of interest. With NER, both contrast improvement and temporal compression can be accomplished in a single step.

In this summary, we demonstrate a new method of contrast improvement that allows both contrast improvement and temporal compression in a single step—divided-pulse nonlinear compression (DPNLC). In DPNLC, a high-energy pulse is divided into multiple low-energy pulses that are spectrally broadened through self-phase modulation (SPM) in gas, as illustrated in Fig. 1. After spectral broadening, the low-energy pulses are coherently recombined back into a high-energy pulse and the recombined pulse is compressed to its new transform limit. We have been developing DPNLC to overcome gas-ionization problems encountered at high energies but have found that the ability to apply an unequal nonlinear phase to the low-energy divided pulses allows us to use the method for contrast improvement as well.

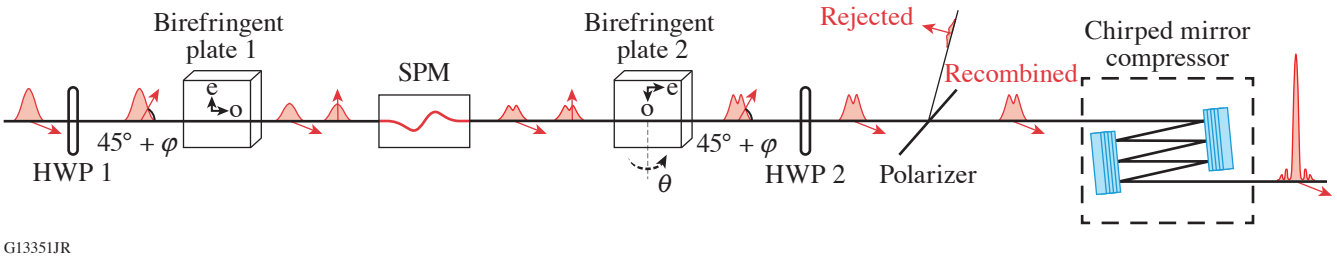

Figure 1
Apparatus for DPNLC. Birefringent plates with extraordinary axis "e" and ordinary axis "o" are used to divide one pulse into two low-energy, orthogonally polarized pulses. Red arrows indicate the pulse's polarization, and the distorted pulse shape after the SPM stage indicates an arbitrary reshaping by nonlinear processes in the SPM stage. After recombination, the polarization is cleaned with a polarizer and the pulse is compressed to a shorter duration with chirped mirrors. The angles φ and θ represent angular alignment errors in polarization and crystal angle of incidence, respectively. HWP: half-wave plate.

In our previous work,[4] we analyzed the alignment tolerances for DPNLC. The final result of our analysis was an expression for the pulse power in each polarization after the recombination step. The output is written as a Jones vector, where the top row is the power in the $\hat{p} = 45° + \varphi$ polarization and the bottom row is the power in the $\hat{m} = 45° + \varphi$ polarization:

$$\bar{P}_{\text{out}} = \frac{e^{-T^2}}{2\sqrt{\pi}} \begin{bmatrix} 1 + \sin^2(2\varphi) + \cos^2(2\varphi)\cos\left[2\phi_{\text{NL}}\sin(2\varphi)e^{-T^2} + \Delta\phi(\theta)\right] \\ \cos^2(2\varphi)\left\{1 - \cos\left[2\phi_{\text{NL}}\sin(2\varphi)e^{-T^2} + \Delta\phi(\theta)\right]\right\} \end{bmatrix}, \tag{1}$$

where we have normalized the expression so integrating over time gives a total energy of 1. In Eq. (1), the two most important alignment angles are the incoming polarization error (φ) and the angle of incidence (AOI, θ) on the second birefringent plate. The nonlinear phase accumulated in the SPM stage is represented by ϕ_{NL}, and $\Delta\phi(\theta) = \phi_2(\theta) - \phi_1$ is the difference in retardance between the two calcite plates. We developed a similar equation that describes a typical prepulse after recombination:

$$\bar{P}_{\text{pre}} = \frac{e^{-T^2}}{2\sqrt{\pi}} \begin{bmatrix} 1 + \sin^2(2\varphi) + \cos^2(2\varphi)\cos\left[\Delta\phi(\theta)\right] \\ \cos^2(2\varphi)\left\{1 - \cos\left[\Delta\phi(\theta)\right]\right\} \end{bmatrix}. \tag{2}$$

These equations indicate a simple method to improve the temporal contrast of the pulse train. Equation (2) shows that if the retardance difference $[\Delta\phi(\theta)]$ is set to zero, the entire prepulse will be found in the $\hat{p}$ polarization. Then we can apply a polarization alignment error (φ) to rotate the main pulse into the $\hat{m}$ polarization. Finally, we use a polarizer to pass the $\hat{m}$ polarization and reject the $\hat{p}$ polarization, thereby rejecting all of the prepulses.

We successfully demonstrated and quantified contrast improvement using these steps. Our laser system is a homebuilt Yb-doped, thin-disk regenerative amplifier that emits 1.2-ps pulses at a wavelength of 1030 nm, a repetition rate of 1 kHz, and an average power of 10 W. The pulses are coupled into a 1.8-m-long, 500-μm-inner-diam, hollow-core fiber (HCF) filled with 1.7 bar of argon for spectral broadening. The pulses accumulate 8.4 rad of nonlinear phase in the HCF. A 12-mm-thick, x-cut calcite plate divides the pulses in two before the HCF, and an identical plate recombines the pulses after the HCF, as previously illustrated in Fig. 1. A half-wave plate (HWP1) is placed before the first birefringent plate to carefully control the incoming polarization error φ, and a second HWP (HWP2) is placed after the last birefringent plate to select either the $\hat{p}$ or $\hat{m}$ polarization for transmission through the recombination polarizer.

First, we measured the original contrast of the laser system. The apparatus in Fig. 1 was aligned with zero alignment errors and measured near-perfect recombination into the $\hat{p}$ polarization (97.3% limited by a 2.5% p-polarization reflection on the polarizer). With this alignment, both the main pulse and prepulses are transmitted by the polarizer with maximum efficiency. The original contrast of the laser was measured by attenuating the beam with a set of neutral-density (ND) filters and then focusing it onto a photodiode. On the photodiode, both the main pulse and prepulses could clearly be seen, as shown in Fig. 2. The maximum prepulse height is 1.9 mV, while the main pulse is 2.3 V; therefore, the initial contrast of the laser is $\sim 10^{-3}$.

Next, we applied a polarization angle error to improve the contrast. We rotated HWP1 until the energy of the main pulse in the $\hat{m}$ was maximized (found at a HWP angle of 3°). Then we rotated HWP2 to transmit the $\hat{m}$ polarization and reject the $\hat{p}$ on the polarizer. We made the same photodiode measurement and found that the prepulses were rejected to below our measurement sensitivity, as shown in Fig. 2. The main pulse was transmitted with high efficiency and measured at 1.7 V.

To quantify the contrast improvement, we removed the ND filters until the prepulses became visible again. We removed 3.5 optical density of the ND filters; we then made fine adjustments to the AOI of calcite plate 2 and the angle of HWP2 to minimize the prepulses and measured a prepulse signal of 0.7 mV. This puts the new contrast of the pulse train at $\sim 10^{-7}$—an improvement of four orders of magnitude.

Finally, we compressed the contrast-improved pulse using a series of chirped mirrors (–43,000-fs group-delay dispersion) and measured the compressed pulse in a second-harmonic frequency-resolved optical gating system. The measured pulse was excellent, compressed with a FWHM pulse duration of 187 fs, close to its transform limit of 180 fs. The compressed pulse with-

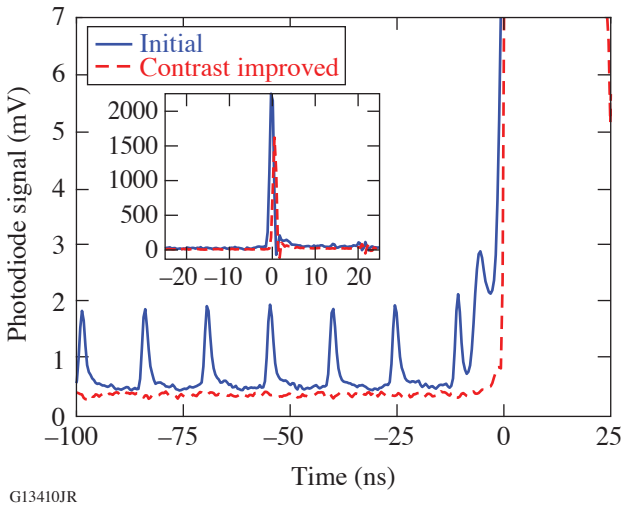

Figure 2
Captured photodiode signals from the pulse train. A train of prepulses with a maximum signal of 1.9 mV is clearly seen before the main pulse, which starts at time = 0. After the HWP's are rotated to improve the contrast, the prepulses are rejected and completely unmeasurable. At the same time, the height of the main pulse is reduced only from 2.3 V to 1.7 V, as shown in the inset.

out contrast improvement was compressible to a similar duration (186 fs with a transform limit of 185 fs) with the same chirped mirrors. Therefore, the contrast improvement method enables temporal compression equivalent to standard HCF operation.

In conclusion, we demonstrated a new method for temporal contrast improvement—divided-pulse nonlinear compression. By slightly misaligning the calcite plates used for pulse division and recombination, we rotated the polarization of the main pulse and rejected problematic prepulses on a polarizer. We measured four-orders-of-magnitude temporal contrast improvement and 72% efficiency for the main pulse, values comparable with other state-of-the-art temporal contrast improvement methods. Simultaneously, we compressed the pulse from 1.2 ps to 187 fs.

This material is based upon work supported by the Department of Energy National Nuclear Security Administration under Award Number DE-NA0003856, the University of Rochester, and the New York State Energy Research and Development Authority.

1. D. Homoelle *et al.*, Opt. Lett. **27**, 1646 (2002).
2. N. Smijesh *et al.*, Opt. Lett. **44**, 4028 (2019).
3. N. G. Khodakovskiy *et al.*, Laser Phys. Lett. **16**, 095001 (2019).
4. G. W. Jenkins, C. Feng, and J. Bromage, J. Opt. Soc. Am. B **38**, 3199 (2021).

Analysis of Pump-to-Signal Noise Transfer in Two-Stage Ultra-Broadband Optical Parametric Chirped-Pulse Amplification

C. Feng, C. Dorrer, C. Jeon, R. G. Roides, B. Webb, and J. Bromage

Laboratory for Laser Energetics, University of Rochester

Optical parametric chirped-pulse amplification (OPCPA) provides the most viable route for the development of tens to hundreds of petawatt peak-power laser systems.[1] In OPCPA, different mechanisms introduce either isolated pulses or a slowly varying pedestal before the main pulse, therefore degrading its temporal contrast, which is defined as the ratio of the peak power of the main pulse to the power of the light in some predetermined temporal range. When the laser beam is focused to interact with the target, the intensity of the light present before the main pulse can exceed a threshold for irreversible modification of the target (e.g., ~10^{12} W/cm^2) and have a detrimental effect on laser–matter interaction. Therefore, understanding the origins of contrast degradation and maximizing the temporal contrast are essential for the development of ultrahigh-peak-power laser facilities.

Pump temporal modulation is one mechanism that can degrade the temporal contrast of the recompressed signal because it induces high-frequency spectral modulation on the chirped signal spectrum during parametric amplification.[2] Pump modulation is commonly introduced by the interference between the main pump pulse and the amplified spontaneous emission (ASE). This modulation is broadband with its bandwidth proportional to the spectral bandwidth of the ASE. Spectrally filtering the ASE of the pump pulse using a narrowband filter is an effective way to reduce the high-frequency pump noise and, therefore, the pump-induced contrast degradation.[3]

In this work, we have investigated, for the first time to our knowledge, the pump-to-signal noise transfer in a two-stage ultra-broadband OPCPA and demonstrated a novel mechanism based on pump-seed delay optimization to reduce the pump-induced temporal contrast degradation by as much as 15 dB (Ref. 4). The results are widely applicable to support the design and development of OPCPA-based ultrahigh-peak-power systems, for which maximizing the temporal contrast is a high priority.

The experimental demonstration was performed in a two-stage ultra-broadband OPCPA system (Fig. 1), which is a subsystem of the Multi-Terawatt–pumped optical parametric amplifier line (MTW-OPAL), i.e., a 0.5-PW, 20-fs, all-OPCPA system.[5] The subsystem consists of an ultra-broadband front end (UFE), two noncollinear optical parametric amplifiers (NOPA4a and NOPA4b), a single pump laser for pumping both NOPA stages, and a grating compressor. In high-power OPCPA systems, it is common to use a single laser to pump several optical parametric amplification stages to reduce experimental complexity and cost. In such a system, the signal amplified in the first stage carries the pump modulations, and amplification in the second stage occurs with a pump pulse having the same modulations. The temporal modulations of the amplified chirped signal and the temporal contrast of the compressed signal pulse, therefore, depend on the difference in pump-seed delay t in different stages, as illustrated in Fig. 1.

We investigated pump pulses with two types of dominating noise, either a 30-GHz sinusoidal modulation or a broadband ASE modulation with ~40-GHz-bandwidth full width at half-maximum (FWHM). Figure 2 plots the experimental and simulation results obtained when NOPA4a and NOPA4b were in the linear amplification regime. The sinusoidally modulated pump pulse represents the case of a multilongitudinal-mode pump laser and was used to facilitate the identification and analysis of the pump-induced contrast degradation. As shown in Fig. 2(a), when the pump-seed delay τ at NOPA4b was equal to zero or to the sinusoidal modulation period T (i.e., T = 33.3 ps), and therefore the pump and seed modulations were in phase, the pump sinusoidal modulation introduced an isolated prepulse (postpulse) at –(+)0.64 ps in the cross-correlation signals of the NOPA4b

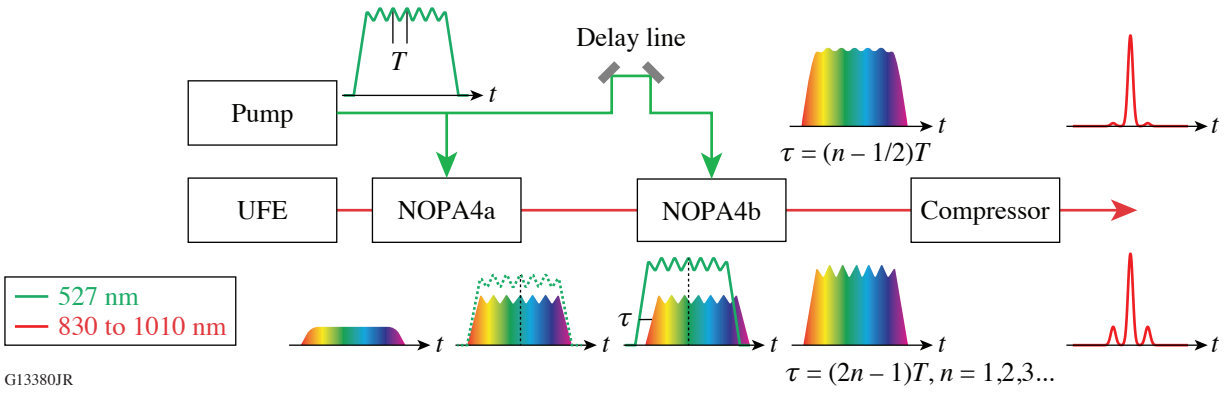

Figure 1
Experimental layout of the two-stage ultra-broadband OPCPA together with the illustrative pump and signal pulses propagating through the system. The delay line controls the pump-seed delay τ with <50-fs temporal resolution.

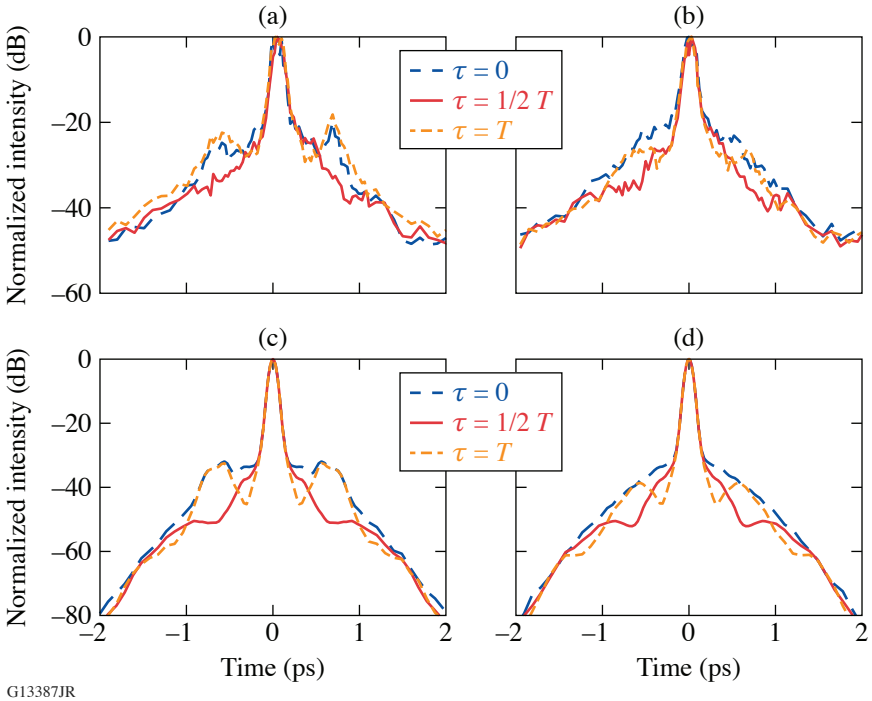

Figure 2
The [(a),(b)] measured and [(c),(d)] simulated cross-correlation signals of the compressed NOPA4b pulses at different pump-seed delays, when both NOPA4a and NOPA4b were operated in the linear regime. T = 33.3 ps corresponds to a modulation frequency equal to 30 GHz. [(a),(c)] The case of a pump pulse with both ASE and 30-GHz sinusoidal modulations; [(b),(d)] the case of a pump pulse with ASE modulation only.

compressed pulses. When the pump-seed delay was set to half the modulation period (i.e., 1/2 T = 16.7 ps) such that the pump and seed modulations had a π phase shift, the pre- and postpulse were strongly suppressed, resulting in the reduction of contrast degradation up to 15 dB. In the more-general case of a pump with broadband ASE modulation, a slowly varying broad pedestal was observed in the compressed pulse and a 10-dB reduction of the contrast degradation at τ = 1/2 T [Fig. 2(b)] was obtained. The simulated cross-correlation signals [Figs. 2(c) and 2(d)] well reproduced the pump-seed-delay–dependent effect.

When NOPA4a and NOPA4b were operated closer to saturation, the measured cross-correlation signals [Fig. 3(a)] showed negligible dependence on the pump-seed delay, which was reproduced by the simulations [Fig. 3(b)] where the limitations in spectral acceptance of the second- and third-harmonic generations in the high-dynamic-range scanning third-order cross-correlator (SEQUOIA®, Amplitude Technologies) were taken into account. These simulations also confirmed, however, that the negligible dependence on pump-seed delay is due to the limited spectral acceptance of the cross-correlator. In the absence of spectral band-

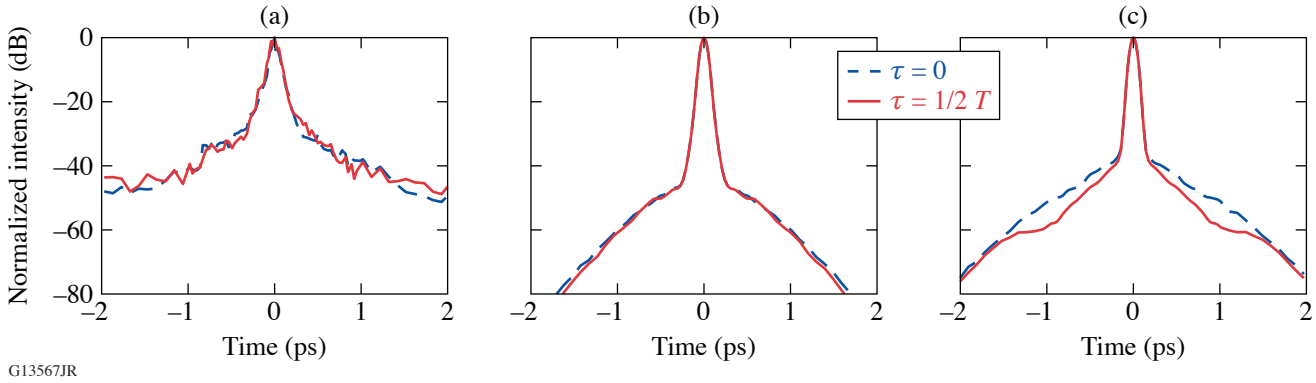

Figure 3
The (a) measured and [(b),(c)] simulated cross-correlation signals of the compressed NOPA4b pulses, when both NOPA4a and NOPA4b were operated closer to saturation and with pump ASE modulation. The spectral acceptance of the third-order harmonic generation in the cross-correlator was limited to 90-nm FWHM using a tenth-order super-Gaussian spectral filter to obtain the results in (b) or kept at >180 nm for the full signal bandwidth for getting the results in (c). Results obtained with only two, instead of three, pump-seed delays are presented for easier visualization of the delay-dependent contrast effect.

width limitation, both cross-correlation signals [Fig. 3(c)] and compressed pulses (simulation not shown) from simulations revealed the delay-dependent contrast effect. Therefore, the pump-seed delay can serve as a simple and cost-effective tool to minimize the pump-induced contrast degradation in a multi-stage OPCPA, even when parametric amplifiers are operated in saturation.

This material is based upon work supported by the Department of Energy National Nuclear Security Administration under Award Number DE-NA0003856, the University of Rochester, and the New York State Energy Research and Development Authority.

1. C. N. Danson *et al.*, High Power Laser Sci. Eng. **7**, e54 (2019).
2. N. Forget *et al.*, Opt. Lett. **30**, 2921 (2005).
3. C. Dorrer *et al.*, Opt. Lett. **32**, 2378 (2007).
4. C. Feng *et al.*, Opt. Express **29**, 40,240 (2021).
5. J. Bromage *et al.*, High Power Laser Sci. Eng. **7**, e4 (2019).

Spectral and Temporal Shaping of Spectrally Incoherent Pulses in the Infrared and Ultraviolet

C. Dorrer and M. Spilatro

Laboratory for Laser Energetics, University of Rochester

Laser–plasma instabilities (LPI's) hinder the interaction of high-energy laser pulses with targets. Simulations show that broadband, spectrally incoherent pulses can mitigate these instabilities. Optimizing laser operation and target interaction requires controlling the properties of these optical pulses. We demonstrate closed-loop control of the spectral density and pulse shape of nanosecond, spectrally incoherent pulses after optical parametric amplification in the infrared (~1053 nm) and sum–frequency generation to the ultraviolet (~351 nm) using spectral and temporal modulation in the fiber front end.[1] The high versatility of the demonstrated approaches can support the generation of high-energy, spectrally incoherent pulses by future laser facilities for improved LPI mitigation.

Temporal and spectral shaping are demonstrated on the fourth-generation laser for ultrabroadband experiments (FLUX) test bed, which is composed of a fiber front end, an optical parametric amplification (OPA) stage, a sum–frequency generation (SFG) stage, and a frequency-doubled Nd:YLF laser system generating the pump pulse for the OPA and SFG stage (Fig. 1). The fiber front end generates the broadband spectrally incoherent OPA seed and the coherent seed for the pump laser using a single high-bandwidth arbitrary waveform generator. The pump laser generates a sequence of two pulses to pump the OPA stage (second pulse) and the SFG stage (first pulse), with a relative delay set to compensate for the optical path difference at 1ω and 2ω between these two stages. Spectral shaping is implemented using a programmable filter (WaveShaper, II-VI). Temporal shaping is implemented using a Mach–Zehnder modulator (MZM) driven by a programmable arbitrary waveform generator (AWG70001, Tektronix).

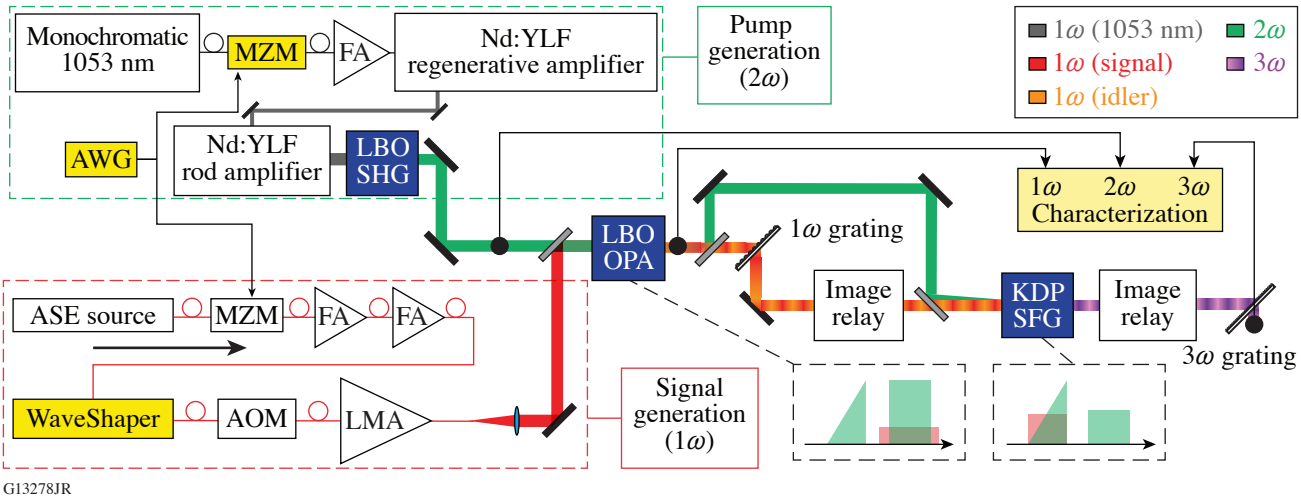

Figure 1
Experimental setup showing the signal generation at 1ω, pump generation at 2ω, amplification in the LBO OPA stage, and frequency conversion in the KDP SFG stage. The properties of the 1ω, 2ω, and 3ω pulses are measured after the OPA, SHG, and SFG stages, respectively. The insets represent the timing configuration for the 1ω pulse (in red) and the 2ω pulses (in green) within the OPA and SFG stages. SFG: sum frequency generation; SHG: sum-harmonic generation; ASE: amplified spontaneous emission; FA: fiber amplifier; AOM: acousto-optic modulator; LMA: large mode area.

The spectrum of the amplified signal measured after the OPA is shaped by controlling the spectrum of the input seed using the programmable spectral filter in the front end. Such shaping can precompensate the wavelength-dependent gain variations in the Yb-doped fiber amplifiers and OPA, although the latter are not expected to be significant, considering that a lithium triborate (LBO) OPA with that length has a bandwidth larger than 100 nm. Without spectral shaping, the OPA output spectrum peaks at ~1032 nm and has a full width at half maximum equal to 7 nm. The wavelength-dependent filter transmission is iteratively modified to decrease the error between the measured spectrum and target spectrum S_{target} (both peak-normalized to 1) using closed-loop control following

$$T_{n+1}(\lambda) = T_n(\lambda) + \eta\left[S_n(\lambda) - S_{\text{target}}(\lambda)\right], \tag{1}$$

where T_n and S_n are the transmission and spectrum as a function of wavelength λ at iteration n, respectively. For stability, the feedback is implemented with η typically equal to –0.1. Initial conditions correspond to a fully transmissive spectral filter [$T_0(\lambda) = 1$] and the resulting spectrum $S_0(\lambda)$. The wavelength axes of the spectral filter and spectrometer are precisely mapped by generating and measuring narrow Gaussian spectra. Figure 2 presents spectral-shaping examples for which S_{target} has been set to a 10-nm flattop profile with a central wavelength ranging from 1032 to 1044 nm [Figs. 2(a)–2(d)] and to the same flattop profiles modulated by a parabolic term [Figs. 2(e)–2(h)]. This simulates spectral shaping for operation at different central wavelengths with precompensation of spectral gain narrowing in subsequent amplifiers.

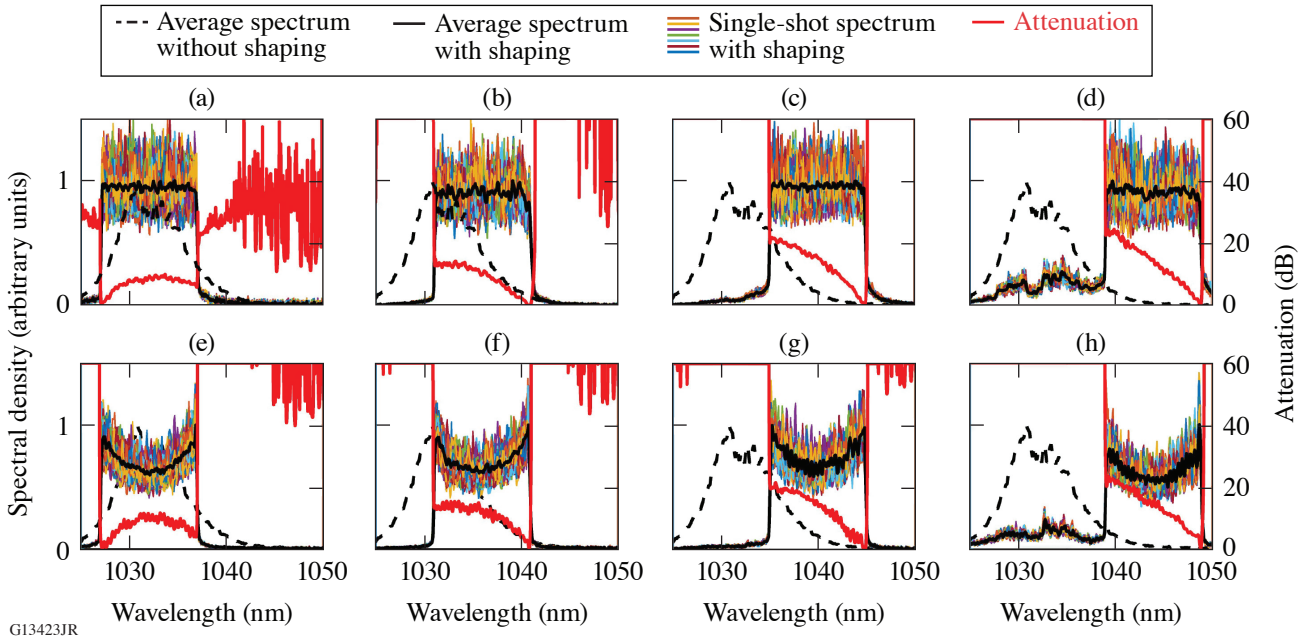

Figure 2
Spectral shaping of the OPA output signal. In the first row, S_{target} is a 10-nm flattop spectrum centered at (a) 1032, (b) 1036, (c) 1040, and (d) 1044 nm. In the second row [(e)–(h)], S_{target} is set to a 10-nm flattop spectrum with parabolic modulation centered at the same wavelengths. In all plots, the spectra averaged over 100 acquisitions without and with shaping are plotted using a dashed black line and solid black line, respectively. The spectra acquired over 100 successive shots are plotted with thin colored lines. The transmission of the spectral filter, in dB, is plotted with a thick red line.

The spectrally shaped 1ω pulses from the OPA are converted to spectrally shaped 3ω pulses using SFG with a narrowband 2ω pulse in a noncollinear angularly dispersed geometry.[2] SFG with a monochromatic field translates the input field along the frequency axis; i.e., it leads to identical spectral features for the input 1ω wave and output 3ω waves if the spectral acceptance is large enough. Figure 3 compares the 1ω and 3ω spectra, where the two wavelength ranges have been set to cover the same frequency range. For Fig. 3(a), the spectral-filter transmission is constant, whereas closed-loop control with various target spectra

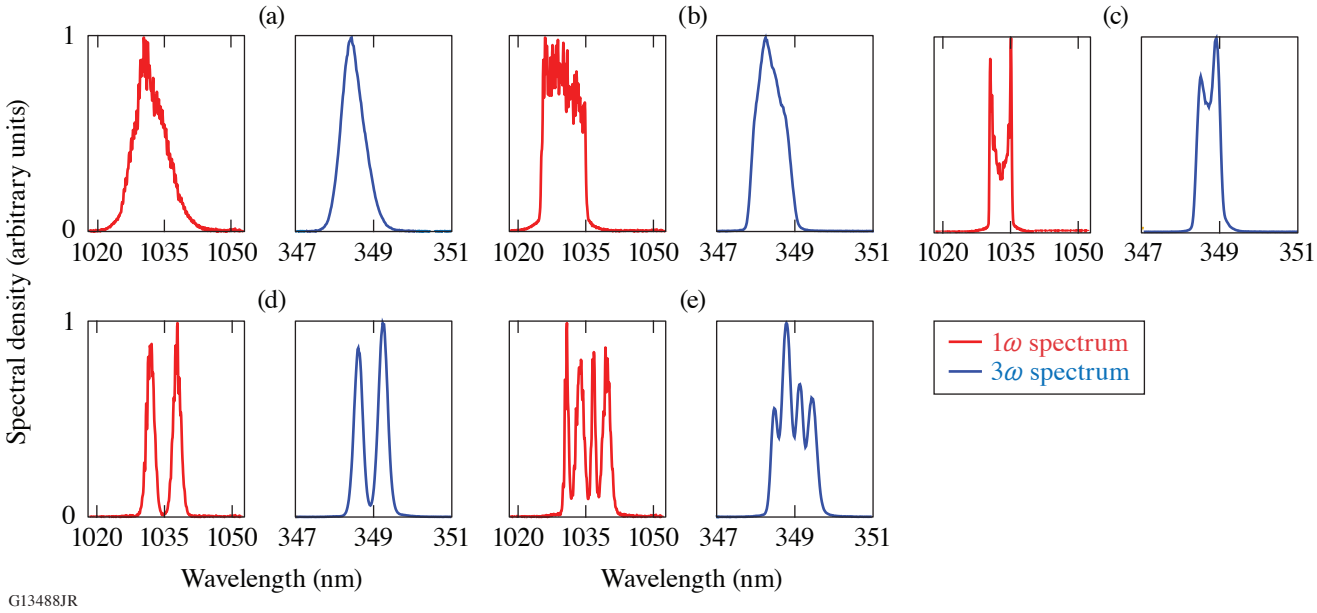

Figure 3
Spectral shaping of the SFG output signal corresponding to a shaped OPA output signal. Plots (a)–(e) show the 1ω spectrum (red line) and the 3ω spectrum (blue line), which are plotted over wavelength ranges that correspond to the same frequency span (10 THz).

was used for the results shown in Figs. 3(b)–3(e). There is generally good agreement between the measured spectral shapes at 1ω and 3ω, although the latter have broader features because of the lower resolution of the UV spectrometer compared to the IR spectrometer (0.25 THz versus 0.05 THz).

Closed-loop pulse shaping has been implemented between the AWG-driven MZM in the fiber front end and the 2ω pulse shape after SHG. A preliminary calibration based on the generation of short Gaussian pulses at different times within the injection window of the regenerative amplifier maps out the linear relation between the time base of the AWG and oscilloscope. Saturation in the fiber amplifiers and Nd:YLF amplifiers leads to significant square-pulse distortion; i.e., the gain at earlier times is significantly higher than at later times within the pump pulse, while the gain observed at a given time depends on the energy that has been extracted at earlier times. Square-pulse distortion in the laser amplifiers, the nonlinear transfer function of the MZM relative to its drive voltage, and the nonlinear second-harmonic generation makes the temporal shaping of the output pulse a complex task. Closed-loop control to generate the pulse shape P_{target} is implemented as follows:

$$W_{n+1}(t) = W_n(t) + \eta\left[P_n(t) - P_{\text{target}}(t)\right], \tag{2}$$

where W_n and P_n are the time-dependent waveform and power at iteration n, respectively. The AWG and MZM are set to implement a monotonic relation between voltage and transmission, while operation at a reference voltage corresponds to the null transmission of the MZM. The shaped pulses, composed of the high-order super-Gaussian OPA pump pulse and the user-defined SFG pump pulse, are routed after convergence to the OPA and SFG stage. Figure 4 displays the shaped 2ω pulse and the resulting 3ω pulse for various user-defined profiles. A super-Gaussian OPA pump pulse (second pulse) is consistently obtained, allowing for temporally uniform OPA saturation. This leads to a flat-in-time amplified 1ω signal, and transfer of the SFG pump pulse shape (first pulse) from 2ω to 3ω via SFG.

This material is based upon work supported by the Department of Energy National Nuclear Security Administration under Award Number DE-NA0003856, the University of Rochester, and the New York State Energy Research and Development Authority.

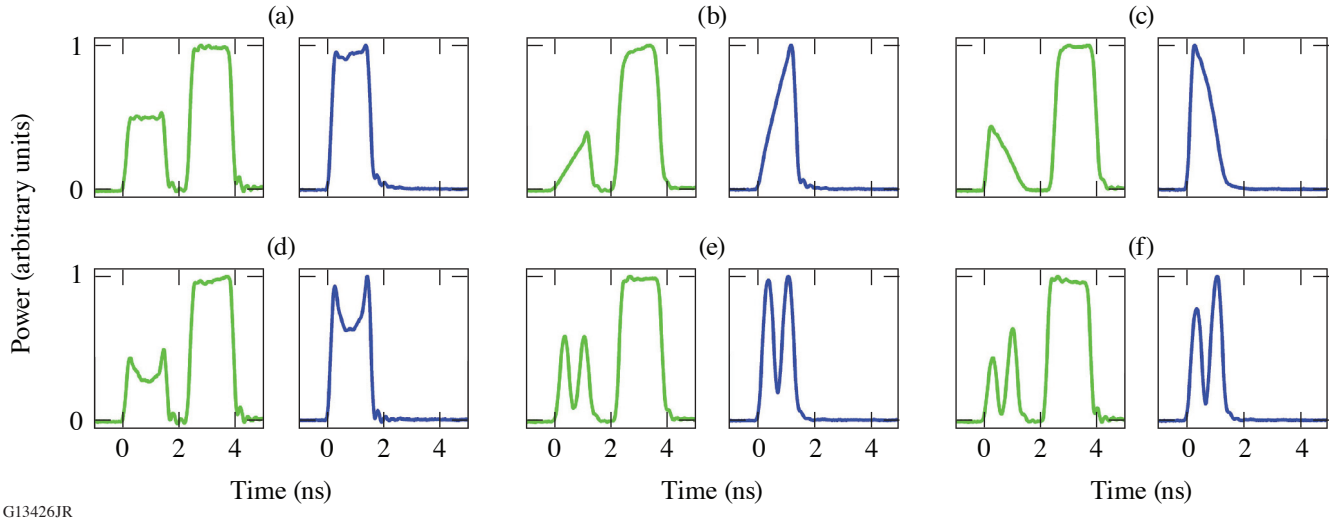

Figure 4
Temporal shaping of the 2ω pump pulse (solid green line) and resulting 3ω pulse shape (solid blue line) for target profiles equal to (a) a super-Gaussian pulse, (b) a positive ramp, (c) a negative ramp, (d) a modulated super-Gaussian pulse, (e) a pair of short pulses with identical amplitudes, and (f) a pair of short pulses with unequal amplitudes. The 2ω pulse is composed of the SFG pump pulse (first pulse) and the OPA pump pulse (second pulse).

1. C. Dorrer and M. Spilatro, Opt. Express **30**, 4942 (2022).
2. C. Dorrer *et al.*, Opt. Express **29**, 16,135 (2021).

Effect of the Pump-Beam Profile and Wavefront on the Amplified Signal Wavefront in Optical Parametric Amplifiers

S.-W. Bahk, I. A. Begishev, R. G. Roides, C. Mileham, R. Cuffney, C. Feng, B. M. Webb, C. Jeon, M. Spilatro, S. Bucht, C. Dorrer, and J. Bromage

Laboratory for Laser Energetics, University of Rochester

Optical parametric chirped-pulse amplification (OPCPA) is known to have advantages over conventional chirped-pulse amplification based on population inversion gain medium.[1] The bandwidth can be extended more than 100 nm without being limited by gain narrowing. The angle between pump and signal beams can be adjusted to provide an even-broader gain bandwidth than collinear geometry. The thermal effect is minimal due to instantaneous energy transfer from pump to signal. The temporal contrast is, in general, better because fewer amplifiers are required and the parametric fluorescence is confined within the pump pulse duration. The OPCPA scheme is a practical way to amplify ultra-broadband pulses to kilojoule energies using commercially available large potassium dihydrogen phosphate (KDP) crystals and existing high-energy nanosecond driver lasers in laser fusion facilities.[2] Deuterated potassium dihydrogen phosphate (DKDP)-based OPCPA systems have been demonstrated on the PEARL laser at the Institute of Applied Physics in Russia[3] and LLE's Multi-Terawatt optical parametric amplifier line (MTW-OPAL).[4] OPCPA lasers based on lithium triborate (LBO)[5,6] or yttrium calcium oxyborate (YCOB)[7] crystals show promising performance at the 800-nm central wavelength seeded by a Ti:sapphire oscillator.

The amplified signal intensity in an optical parametric amplifier (OPA) is a nonlinear function of pump intensity. In general, a flattop pump profile at a fixed intensity is optimal for good conversion efficiency from the pump to signal. In this regime, the amplified signal-beam profile and spectrum are saturated following the pump-beam profile and the pulse shape. The amplification-induced signal phase or "OPA phase" exhibits a phase shift similar to the one observed in a population inversion system.[8] Several authors have investigated the effect of pump on the OPA phase. Ross *et al*. concluded that the OPA phase is a function of pump intensity. They have formally shown that the pump-beam phase impacts the idler phase but does not affect the signal phase.[9] Li *et al*. have experimentally shown that astigmatism in the pump beam is transferred to the idler beam.[10]

Others, however, found that the OPA phase is affected by the pump phase as well. Wei *et al*. have numerically shown that the pump-beam walk-off introduces phase transfer from pump to signal and suggested a walk-off–compensated geometry to mitigate this effect.[11] The same group later experimentally demonstrated the mitigation effect.[12] Chen *et al.* gave a qualitative description of the pump-to-signal phase transfer effect being proportional to the pump wavefront derivative.[13]

Authors in Refs. 10–13 studied the effect of input beam wavefronts on the OPA phase using wave equations and numerical simulations. We analyze this effect using the analytic OPA phase solution and the wave-vector picture. The phase solutions of the three waves in an OPA process have been studied by several researchers[9,14] and were recently presented in closed form in Ref. 15. The main results for the case of zero idler input are summarized here for convenience:

$$\phi_s(L) = \phi_s(0) + \psi_s\left[\Delta k, I_s(0), I_p(0), L\right], \tag{1}$$

$$\phi_i(L) = \pi/2 - \phi_s(0) + \phi_p(0) - \Delta kL/2. \tag{2}$$

The function ψ_s is an additional phase introduced in the signal beam by the OPA process and will be equivalently called the "OPA phase." The ψ_s is a function determined by four independent parameters and has a term made of the incomplete elliptic integral of the third kind [for the detailed expression of ψ_s, refer to Eq. (17) of Ref. 15]. I and ϕ denote intensity and phase with the subscripts "s, i, p" indicating signal, idler, and pump, respectively; L is the crystal thickness. The OPA phase is determined by the input signal and pump intensities, the wave-vector mismatch (Δk), and the crystal thickness (L). The dependence on the input signal's intensity is weak for the normal OPA regime, where $I_s(0) \ll I_p(0)$.

Equation (2) shows that the phases of the input signal [$\phi_s(0)$] and input pump [$\phi_p(0)$] are all directly transferred to the output idler phase. Although this is mostly true, the OPA phase ψ_s is not entirely immune to input phase aberrations. The subtlety lies in the fact that the wave vector is normal to the input phase front in a spatially coherent beam; therefore, the spatial phase variation is accompanied by variation in Δk, which in turn impacts ψ_s. (We assume here a regime where diffraction is negligible over the length of the crystal.) The OPA phase also depends on the input pump intensity independently from the input phase.

The OPA phase is linear with respect to Δk within amplification bandwidth. The OPA phase in the linear regime can be approximated as

$$\psi_s \sim -\frac{\Delta k}{2} L\left\{1 - \frac{1}{a\sqrt{I_p(0)L}} \tanh\left[a\sqrt{I_p(0)L}\right]\right\}, \tag{3}$$

where $a\left(d_{\text{eff}}/c\right)\sqrt{2\eta_0\omega_s\omega_i/n_s n_i n_p}$ (Ref. 15). One can numerically show that $a\sqrt{I_p(0)}L \sim 1.16\log_{10}(\text{gain}) + 1.36$ in the depletion regime with perfect phase matching, where gain is defined as the ratio of output to input signal intensities [$I_s(L)/I_s(0)$]. For a 20-dB gain, $a\sqrt{I_p(0)}L \sim 3.68$, and Eq. (3) in terms of relative phase can be further approximated to

$$\Delta\psi_s \sim -0.36\Delta(\Delta k)L. \tag{4}$$

The local wave vectors of pump and signal waves are normal to their phase front. The wave-vector mismatch is a function of pump and signal phase slopes or derivatives. $\Delta(\Delta k)$ can be written as

$$\Delta(\Delta k) = \left(-\rho_{p,x} + \frac{k_{s,0}}{n_i k_{i,0}} a_{x,0}\right)\frac{\partial\phi_{p,0}}{\partial x} + \left(-\frac{k_{p,0}}{n_i k_{i,0}} a_{x,0}\right)\frac{\partial\phi_{s,0}}{\partial x} + \left(\frac{k_{s,0}}{n_i k_{i,0}} a_{y,0}\right)\frac{\partial\phi_{p,0}}{\partial y} + \left(-\frac{k_{p,0}}{n_i k_{i,0}} a_{y,0}\right)\frac{\partial\phi_{s,0}}{\partial y}. \tag{5}$$

The Δ notation in the above equations denotes relative change across two points in space. The incident pump and signal phase terms here are residual phases that do not include tilt terms corresponding to the incidence angles. Equation (5) shows that the noncollinear interaction angle allows both seed and pump-beam wavefront gradients to be transferred to the OPA phase. On the other hand, the birefringence term ($\rho_{p,x}$) always enables the pump wavefront transfer-to-OPA phase even with the collinear geometry. It is possible to mitigate the birefringence-induced OPA phase by choosing the sign of the noncollinear angle in order to cancel the coefficient of the pump phase gradient, which is the first term in Eq. (5). This was attempted by Wei and Yuan,[11,12] but the cancellation of the pump gradient term increases the signal gradient term, only shifting the problem from the pump to the signal side. Such cancellation is also a trade-off with other considerations that typically constrain the relative angle between pump and signal, e.g., bandwidth requirements and mitigation of parasitic second-harmonic generation.

Equations (4) and (5) show good agreement with the wave-equation approach of Refs. 10–13 in the absence of diffraction except that the small spatial positions shift in the beams coming from birefringence and the noncollinear angle does not appear in the wave-vector approach.

The spatial variation of the pump-beam amplitude can also affect the OPA phase. Figure 1 shows the OPA phase variation with respect to pump intensity using the more-accurate OPA phase expression in Eq. (17) of Ref. 15. Equation (4) is not accurate enough at pump intensities below what is required for depletion or at comparable signal and pump intensities. These plots were

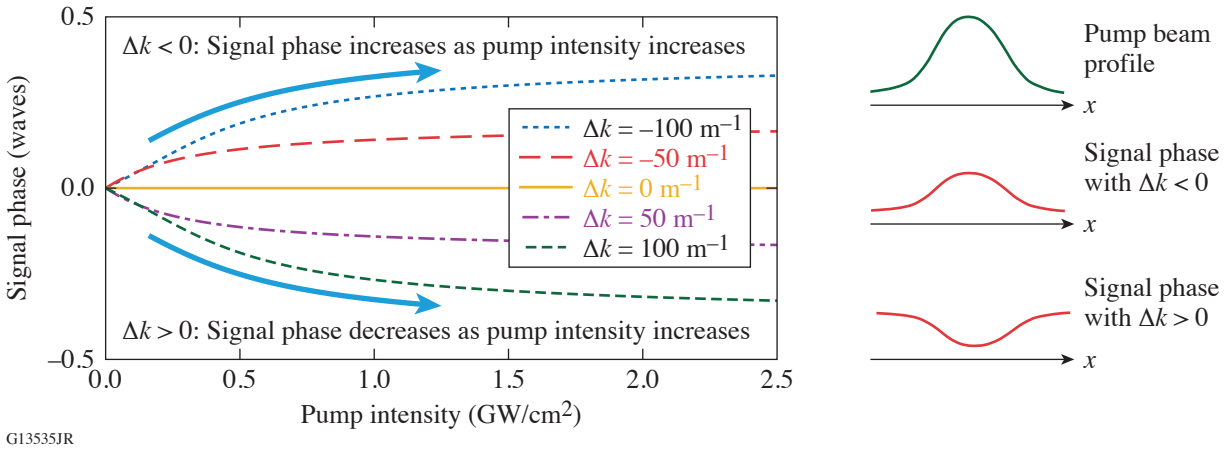

Figure 1
Effect of pump-beam intensity on the signal phase at different wave-vector mismatches.

generated using a 1-MW/cm^2 signal at 920 nm and a pump intensity at 527 nm from 0 GW/cm^2 to its depletion intensity, which is 2.5 GW/cm^2 for a 52-mm-long crystal. Unlike the phase effect, the amplitude effect depends on the sign of Δk. With positive Δk, the signal phase decreases with increasing pump intensity, whereas the trend is the opposite for negative Δk. When the phase mismatch is not equal to 0, the pump-beam shape is imprinted onto the signal phase. This qualitative behavior is illustrated on the right-hand side of Fig. 1 for a Gaussian-like pump beam.

It is interesting to note that this is similar to the intensity-dependent nonlinear effect with a sign dependency on phase matching as in cascaded nonlinearity.[15,16] The sign and amplitude change for spectral variations in Δk implies chromatic aberrations depend on the way Δk varies across the spectrum. Wang *et al*. described the chromatic effects in more detail.[17] With the linear dependence of Δk on frequency and a Gaussian-profile pump beam, this results in a radial group delay. The relative strength of the dispersion terms of Δk can easily change, depending on the phase-matching conditions and may exhibit more-complicated spatiotemporal coupling. On the other hand, chromatic effects induced by the pump phase are not significant because the signal phase's response is linear with the same slope wherever Δk is within the amplification bandwidth.

We conducted experiments to verify the prediction of pump wavefront and amplitude effect on the OPA phase in the final amplifier of the MTW-OPAL laser. Details about the MTW-OPAL system and the final pump laser are provided in Refs. 4 and 18. We specifically study the pump phase's effect in a collinear amplification geometry and the pump amplitude's effect. The amplifier, called NOPA5 being the fifth noncollinear OPA in the system, is based on a 52-mm-long, 70%-deuterated KDP crystal. The pump-signal angle for an optimum amplification bandwidth depends on the deuteration level.[19] The amplifier is currently configured in a collinear geometry because this configuration is optimal for the 70% DKDP crystal. The seed beam is a 100-mJ, 42-mm square beam. The seed pulse has a 150-nm bandwidth stretched to 1.2 ns. The pump beam is a 50-J, 40-mm square beam with a 1.7-ns pulse width. Beam size, pulse width, and bandwidth are estimated at 20% of the peak. The pump and signal are combined with a broadband dichroic mirror. The input pump wavefront and the output signal wavefront were sampled through leaky mirrors and measured with wavefront sensors after down-collimation and imaging. The signal wavefront was measured with a 930-nm bandpass filter. The inherent aberrations in the signal beam imaging system are estimated to be 0.16 waves peak to valley (p–v) based on a double-pass retro measurement. The design aberrations in the pump beam's imaging system are 0.2 waves p–v but no special effort was taken to measure the pump beam's diagnostic aberrations. The spectra of the input and output pulses are sampled by fiber-coupled diffusers and transported to a multichannel spectrometer. The energies of the pump and signal pulses are either measured directly with calorimeters or indirectly in the diagnostics beam path with calibration factors. The crystal is angle tuned using a precision rotation stage. We induce specific phase modulations on the pump beam using a phase plate after the main pump amplifiers or specific amplitude modulation upstream before the amplifiers using a programmable beam-shaping system.[20]

A high-order phase plate with ~2.5 waves (p–v) transmitted wavefront at 526 nm was inserted in the pump-beam path to introduce a more-complex phase profile, as shown in Fig. 2(a). The resulting signal intensity and wavefront, with bandpass filtration at 930 nm, are shown in Fig. 2(b); the calculated counterparts are shown in Fig. 2(c). The measured wavefront is a relative wavefront referenced against the amplified signal wavefront without the phase plate. The amplitude and overall shape of the measured and calculated wavefronts, in particular local extrema, are in excellent agreement.

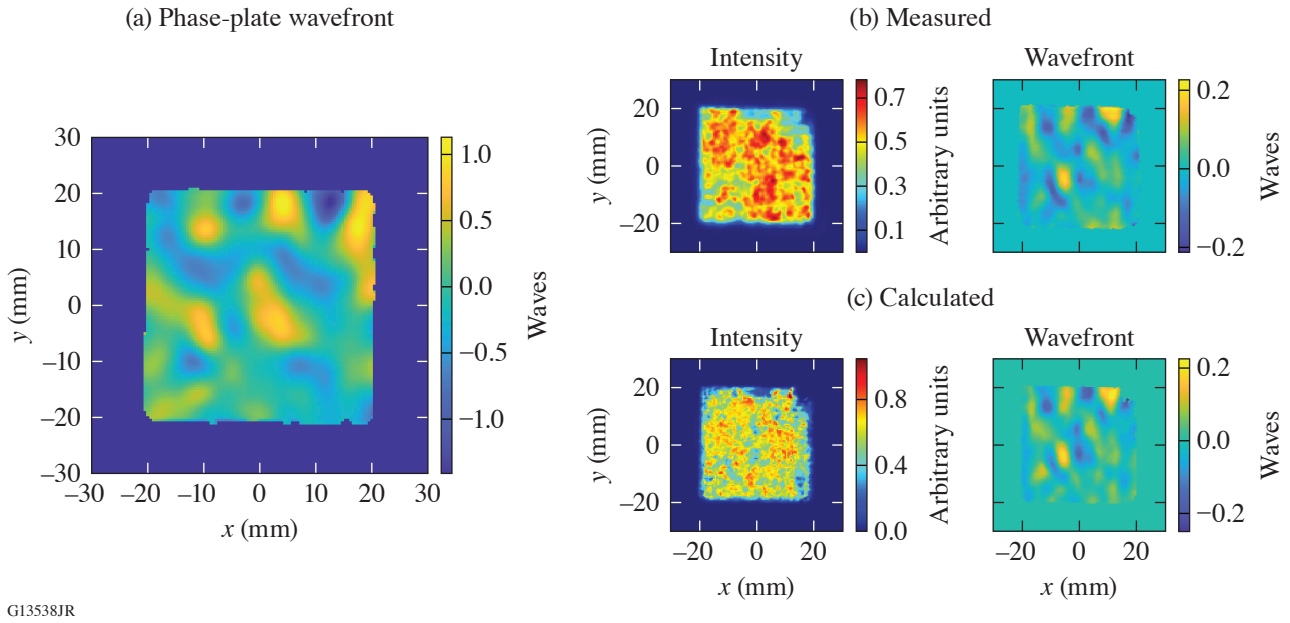

Figure 2
(a) Transmitted wavefront of the phase plate, (b) measured intensity and wavefront, and (c) calculated intensity and wavefront at 930 nm.

To investigate the amplitude effect, the beam-shaping system[20] for the pump beam was used to produce a cylindrical Gaussian-like beam as shown in Fig. 3(a). The crystal angle was detuned ±0.017° to change the sign of Δk and demonstrate its sign sensitivity on the induced wavefront. The lineouts of the measured and calculated wavefronts at 930 nm are shown in Fig. 3(b) as solid and dashed lines, as shown in the legend. The lineouts are averaged over 80% of the central region of the beam in the y direction. This comparison shows a good agreement in the overall quadratic shape following from the pump-beam profile. We also measured the wavefronts at three wavelengths (890 nm, 930 nm, and 990 nm) using bandpass filters installed in front of three separate wavefront sensors as shown in Fig. 3(c), which directly show chromatic effect.

We presented a detailed theory of the OPA phase produced by the pump and signal wavefronts and measured the OPA phase from the pump wavefront. The main theoretical result is that the OPA phase is proportional to the derivative of the pump and signal wavefronts in the phase-matching direction. The birefringent walk-off and noncollinear interaction geometry couple the phase derivative terms to phase mismatch and therefore to the OPA phase. The effect of the pump-beam profile has also been investigated. Our expressions showed the OPA phase depends on the pump intensity and the sign of the phase mismatch. The signal wavefront modulation caused by the pump-intensity modulation is more sensitive at a lower pump intensity. A small amount of chromatic aberrations following the shape of the pump profile is expected.

We performed experiments demonstrating both the phase and amplitude effect of the pump beam on the OPA phase using a broadband OPA amplifier in a collinear geometry. The pump wavefront effect was investigated by adding a high-order phase plate in the pump beam. The experiment confirmed that the induced signal phase is related to the pump phase gradient in the phase-matching direction. The OPA phase due to the pump beam profile was measured for different phase-matching conditions

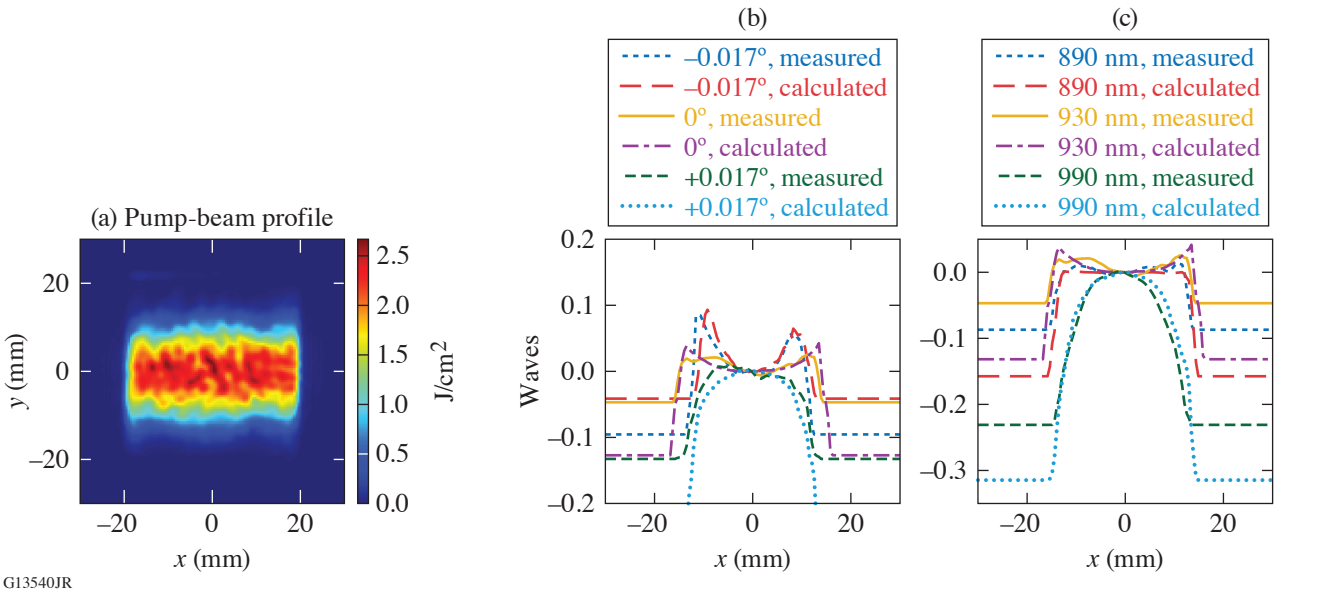

Figure 3
(a) Vertically nonuniform pump-beam profile; (b) measured and calculated wavefront-averaged vertical lineouts at different crystal tuning angles; (c) measured and calculated wavefront averaged lineouts at three wavelengths at 0°.

obtained by slightly detuning the crystal. The measurements confirmed that the amplitude-induced OPA phase depends on the sign of the phase mismatch and the pump-beam profile.

The traditional understanding of the general behavior of the pump-beam wavefront being transferred to the idler beam is, in general, correct in the sense that the OPA phase introduced by the pump-beam wavefront is generally an order of magnitude smaller than the pump wavefront directly transferred to the idler beam. The transfer to the signal beam can be non-negligible, however, for a larger system with large wavefront errors. The experimental verification of the pump and signal phase effect for noncollinear geometry will be discussed in subsequent publications. We expect the considerations presented in this summary will play an important role for future construction of a scaled-up high-energy broadband OPCPA system, where the wavefront becomes difficult to control as the beam size increases.

This material is based upon work supported by the Department of Energy National Nuclear Security Administration under Award Number DE-NA0003856, the University of Rochester, and the New York State Energy Research and Development Authority.

1. G. A. Mourou, T. Tajima, and S. V. Bulanov, Rev. Mod. Phys. **78**, 309 (2006).
2. C. N. Danson *et al.*, High Power Laser Sci. Eng. **7**, e54 (2019).
3. V. V. Lozhkarev *et al.*, Opt. Express **14**, 446 (2006).
4. J. Bromage *et al.*, High Power Laser Sci. Eng. **9**, e63 (2021).
5. L. Xu *et al.*, Opt. Lett. **38**, 4837 (2013).
6. M. Galletti *et al.*, High Power Laser Sci. Eng. **8**, e31 (2020).
7. S. Yang *et al.*, Opt. Express **28**, 11,645 (2020).
8. R. S. Nagymihaly *et al.*, Opt. Express **27**, 1226 (2019).
9. I. N. Ross *et al.*, J. Opt. Soc. Am. B **19**, 2945 (2002).
10. W. Li *et al.*, Appl. Phys. B **123**, 37 (2016).
11. X. Wei *et al.*, Opt. Express **16**, 8904 (2008).
12. P. Yuan *et al.*, High Power Laser Sci. Eng. **2**, e30 (2014).
13. Y. Chen *et al.*, Adv. Condens. Matter Phys. **2018**, 5731938 (2018).

14. H. J. Bakker *et al.*, Phys. Rev. A **42**, 4085 (1990).
15. S. W. Bahk, Opt. Lett. **46**, 5368 (2021).
16. R. DeSalvo *et al.*, Opt. Lett. **17**, 28 (1992).
17. Y. Wang *et al.*, Opt. Lett. **46**, 5743 (2021).
18. I. A. Begishev *et al.*, Appl. Opt. **60**, 11,104 (2021).
19. K. Ogawa *et al.*, Opt. Express **17**, 7744 (2009).
20. S.-W. Bahk, I. A. Begishev, and J. D. Zuegel, Opt. Commun. **333**, 45 (2014).

Evaluation of Transverse Raman Scattering in KDP and DKDP in Geometries Suitable for Beam Polarization Control

T. Z. Kosc, H. Huang, T. J. Kessler, and S. G. Demos

Laboratory for Laser Energetics, University of Rochester

KDP and DKDP are particularly suitable materials for polarization control due to their ability to grow in large sizes and their inherent birefringence. However, their performance in large-aperture, high-fluence systems at 351 nm is hindered by the generation of transverse stimulated Raman scattering (TSRS)[1,2] seeded by the strong symmetric A_1 Raman mode. This process transfers energy to parasitic transverse beams and thereby limits the maximum power output in order to avoid damage to the optic and its mount. The intensity of the TSRS signal is governed by the propagation length (optic size) L; the laser intensity I_{pump}; and the Raman-gain coefficient g, where the latter is directly proportional to the spontaneous Raman-scattering cross section, $\mathrm{d}\sigma/\mathrm{d}\Omega$:

$$I_{\text{TSRS}} \sim \exp\left(gI_{\text{pump}}L\right), \text{ where } g = \left(8\pi cM \big/ \hbar\omega_s^3 n^2 \Delta\bar{\nu}\right) \cdot \left(\mathrm{d}\sigma \big/ \mathrm{d}\Omega\right).$$

The strength of the Raman-scattering cross section in a given orientation is related to the mode's Raman polarizability tensor which was only recently ascertained with high accuracy (due to the presence of numerous measurement artifacts mainly arising from depolarization of the pump beam and Raman signal during propagation in these birefringent materials) for both KDP and 70% DKDP.[3]

The goal of this work is to develop a modeling capability to evaluate the TSRS risk and its directional dependence in geometries relevant to polarization control. This ability, in turn, will enable optimization of the design (such as the crystal-cut orientation) of KDP or DKDP polarization control optics and guide the design of future laser systems. To support this modeling effort, a detailed experimental study of the transverse Raman scattering was conducted to validate the model accuracy. Experiments were performed using a novel setup detailed in Ref. 4 that utilized spherical samples to enable accurate measurements at relevant excitation geometries. A complete set of data was acquired by varying three parameters: (1) the angular position θ of the optic axis (OA) with respect to the vertical pump beam between 0° and 90°, (2) the angular alignment α of the pump-laser polarization relative to the vertical plane containing the OA, and (3) the transmission axis of the signal analyzer (parallel and orthogonal with respect to the beam-propagation direction). The data shown in Fig. 1 were obtained for an excitation and signal collection geometry suitable for polarization control (angle between OA projection on transverse plane and laser polarization $\alpha = 45°$). The signal intensity is normalized to the signal corresponding to the orientation that produces the maximum spontaneous Raman-scattering cross section in each material. The signal detected using the parallel analyzer arises mainly from polarization artifacts, which also cause the complex peak and valley features detected when using the orthogonal analyzer. As Fig. 1(c) demonstrates, the model is capable of reproducing the experimental results fairly accurately when considering the experimental conditions (a 32-mm-diam sphere, an ~0.5° incident half-angle, and a 5.7° collection half-angle).

The ray-tracing model tracks the spontaneous Raman emission using geometrical optics. Rays are generated from each point source (with initial intensity determined according to the relevant tensor products) and propagate in all directions as either ordinary (o) or extraordinary (e) components acquiring different phases. In the cross-section simulations, the source volume contains a large number of such source points and the collected Raman o and e photons are considered mutually incoherent. The corresponding experimental results (with the analyzer parallel and perpendicular to the pump laser) are estimated as the sums of the projections of the o and e components.

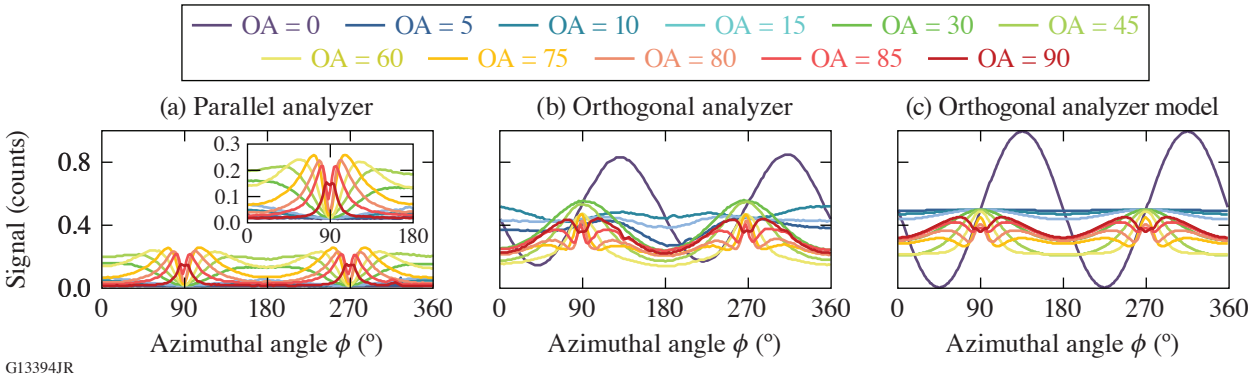

Figure 1
Data acquired using the KDP spherical sample with the Raman signal analyzer aligned (a) parallel and (b) perpendicular to the pump laser. (c) Ray-trace modeling reproduced experimental data, including polarization rotation artifacts. The pump polarization was set at $\alpha = 45°$ with respect to the vertical plane containing the crystal OA, whose position is varied between 0° and 90° with respect to the beam-propagation direction.

The ray-trace modeling also confirmed that the polarization rotation artifacts decrease as the collection aperture size is reduced. If we assume a collimated beam propagating though the crystal and the Raman scattering detected over an infinitely small collection angle, the signal with the analyzer perpendicular to the pump beam will converge the shape of the total signal (sum of the two analyzer positions). This behavior is shown in Fig. 2, which includes the (a) experimental and (b) modeling results.

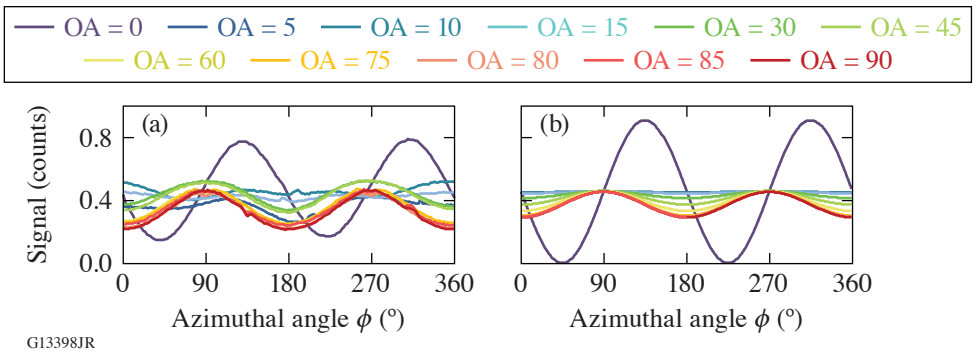

Figure 2
The sum of the parallel and perpendicular polarizations is shown as the total Raman signal for (a) experimental data and (b) the model. The polar angle varied between 0° and 90°, and the profile color coding is the same as in Fig. 1.

The results discussed above can be directly applied for the assessment of the TSRS risk in large-aperture laser systems. The validation of the model and methodology by the experimental results provides confidence on its use to guide crystal-cut optimization needed to minimize TSRS gain, to predict maximum operational fluence, or to help develop novel designs with complex polarization control properties in large-aperture optics. Future work will consider the design of specialized optics and include the ray paths contained by total internal reflection or retroreflected conditions that introduce longer gain paths.

This material is based upon work supported by the Department of Energy National Nuclear Security Administration under Award Number DE-NA0003856, the University of Rochester, and the New York State Energy Research and Development Authority.

1. C. E. Barker *et al.*, Proc. SPIE **2633**, 501 (1995).
2. S. N. Dixit *et al.*, J. Phys. IV France **133**, 717 (2005).
3. T. Z. Kosc *et al.*, Sci. Rep. **10**, 16283 (2020).
4. T. Z. Kosc *et al.*, Rev. Sci. Instrum. **91**, 015101 (2020).

LLE BEST Student and Teacher Research Program: Broad Exposure to Science and Technology

T. J. Kessler

Laboratory for Laser Energetics, University of Rochester

The primary goal of the Broad Exposure to Science and Technology (BEST) Research Program is to engage underrepresented high school students and their teachers in various aspects of science and technology that support LLE's laser science and applications research. This broad exposure helps guide students in their pursuit of STEM fields and encourages them to explore the next generation of related jobs and careers. Teacher participation equips educators with knowledge and experience that can be brought back to their schools to enhance science and technology curricula during the school year. The BEST program was carried out at East High School within the Rochester City School District (RCSD) during the summer of 2021. Four high school students and two teachers participated in the pilot program (Fig. 1). This research experience occurred over a six-week period during the months of July and August.

I3044JR

Figure 1
The participants of the BEST program in 2021 included (from left to right) East High teachers Trent Russell and Gavin Jenkins, East High students Yusuf Gazali, Reganae Walters, Taiasia Gibson, and Ramir Wearen, and program coordinator Terry Kessler, LLE Diversity Manager.

The teachers and students were exposed to different areas of science and technology research such as optical microscopy, optical testing and design, holography, liquid crystals, the Omega Laser Facility, and technical communications. The importance of engineering support for research, including chemical, electrical, mechanical, optical, computer, and workspace engineering, were emphasized to highlight the extensive teamwork required to make advancements in these fields. Students and teachers were given tours of LLE's laser science and technology laboratories during the program period.

The BEST team attended LLE Zoom presentations and discussions each week. They carried out science and technology research at East High School using temporarily relocated LLE equipment including microscopy, interferometry, and holography systems. Some examples of the many experimental activities are shown on the screen located in the middle of the white board (Fig. 1). The white board or "Google Board" displays each day's goals and the many questions generated by the students and teachers during lectures, demonstrations, and laboratory investigations.

Large scientific institutions, such as UR/LLE, employ many different types of professionals to carry out their research activities. Each of the many research and support activities requires teams consisting of these professionals. This matrix relationship shown in Fig. 2 is what allows LLE to maintain a successful research program. Exposure to this science and technology matrix provided the students and teachers with an understanding of the broad diversity of research activities as well as the rich diversity of individual professionals that enable the research to flourish.

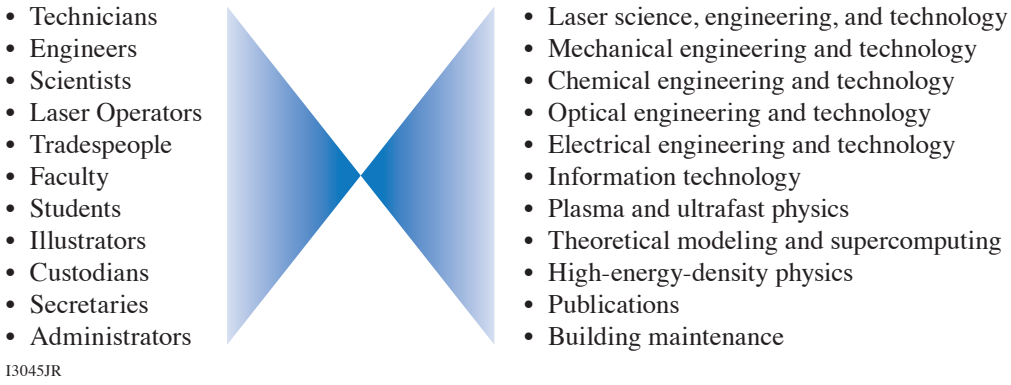

Figure 2
The BEST students and teachers were introduced to the many employment positions (left) that constitute the workforce at LLE. These positions support the wide variety of activities (right) needed to maintain the thriving science and technology research at LLE. Exposure to the LLE workforce provides guidance for students to choose their education and training experiences.

A team of LLE volunteers worked with the BEST students and teachers in a variety of science and technology fields (see Fig. 3). Each volunteer spent between one and four days at East High school over a six-week period. The program coordinator provided backup in order for the team members to maintain a flexible schedule during the summer months. Each volunteer, being an expert in their research field, was able to bring detailed information, coupled with hands-on opportunities, into the high school laboratory environment. For future summer programs, it is envisioned that the students and teachers will be exposed to additional fields of science and technology including laboratory operations, light–matter interaction, publications, and the technology trades that support all research activities at LLE.

LLE mentors exposed the students and teachers in the BEST Program to various technologies that are critical to the design and operation of the OMEGA 60 and OMEGA EP Laser Systems (see Fig. 4). Circuit board technologies were explored by dissecting computer systems, studying hardware design, and practicing the microsoldering techniques used to assemble electronic components. Laser hardware, such as alignment lasers and laser amplifier materials, were brought into the classroom for demonstration and exhibition. In addition, the phase transitions of liquid crystal materials were investigated, while optical components used to control the polarization and color of light were manufactured. This broad exposure highlighted the technologies that connect electronics, optics, and chemistry to laser systems.

I3046JR1

Figure 3
A team of nine LLE participants [(shown left to right) Terry Kessler, lasers/holography; Karen Cera, laboratory safety; Stavros Demos, spectroscopy/microscopy; Tanya Kosc, light polarization; Mike Krowl, electronics technology; Ken Marshall and Nate Urban, liquid crystals; Brian Kruschwitz, grating applications; and Nickolaos Savidis, optical design] worked with the BEST students and teachers in a variety of science and technology fields including laboratory safety, holography, spectroscopy, microscopy, light polarization, mechanical systems, electronics technology, liquid crystals, chemistry, diffraction gratings, and optical system design and prototyping.

(a)

(b)

(c)

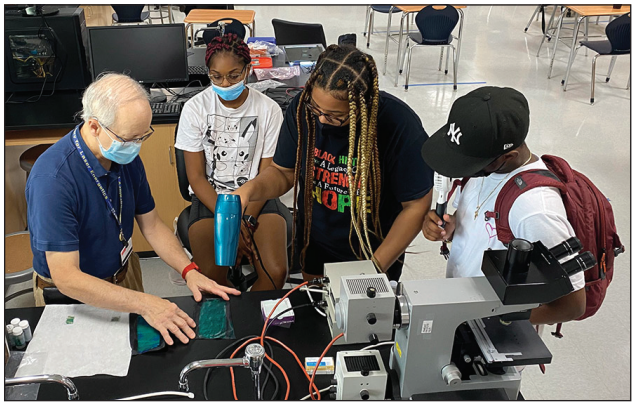

I3047JR

Figure 4
(a) Tanya Kosc, Optical Materials Technology Group Scientist, is shown exhibiting a neodymium-doped laser amplifier rod. (b) Mike Krowl, Electronics Group Technician, is shown instructing the students and teachers in circuit board technology including computer components and microsoldering techniques. (c) Ken Marshall, Optical Materials Technology Senior Research Engineer, is shown working with students on techniques to apply layers of liquid crystal to flexible fabrics.

A holographic interferometer was constructed at East High to record array-generating diffraction gratings. The number of reconstructed spots (orders) was plotted as a function of the development time in seconds (Fig. 5). Students view the multicolor orders by looking through the diffraction grating at a white-light source. The array of multicolor spots was photographed showing the characteristic blue to red angular shift for each order. This activity provided the hands-on experience to understand how gratings and grating spectrometers work. LLE mentors built on this experience to instruct the students and teachers on the basic concepts of chirped-pulse amplification and smoothing by spectral dispersion, two important laser schemes to produce high-intensity short pulses and uniform focal spots, respectively.

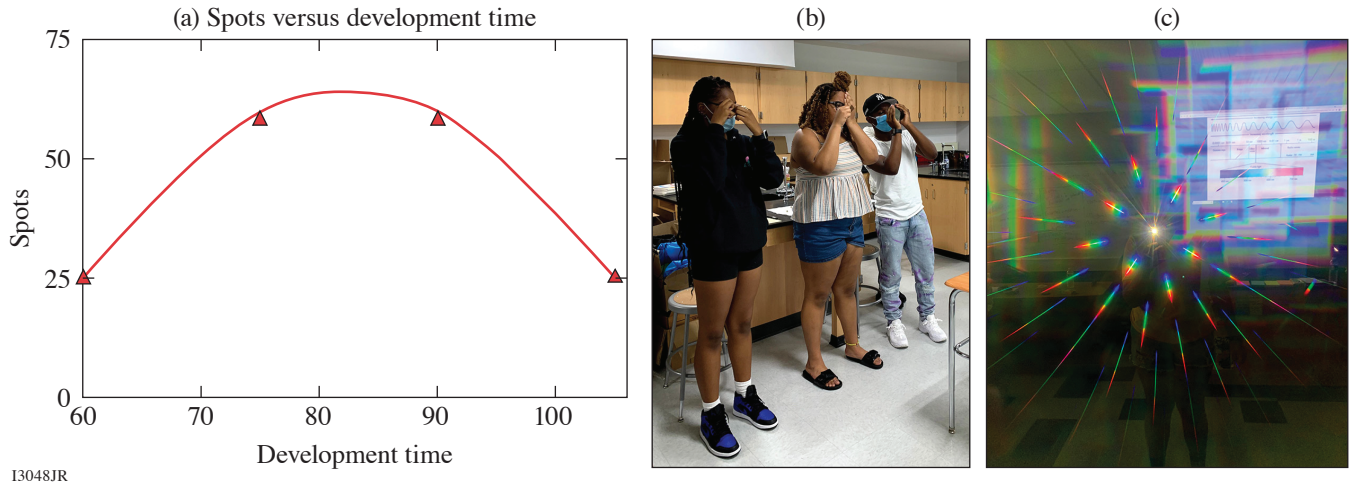

Figure 5
(a) The number of reconstructed spots from a multi-order diffraction grating was plotted as a function of the development time in seconds. (b) Students view the multicolor orders by looking through the diffraction grating at a white-light source. (c) The array of multicolor spots shows the characteristic blue to red angular shift for each order.

Spectroscopy is the study of the absorption and emission of light and other radiation by matter. There are numerous applications of spectroscopy at LLE including optical material composition analysis, light-scattering investigations, and the study of laser–matter interaction. Brian Kruschwitz, Group Leader of OMEGA System Science, worked with students to construct a grating spectrometer in a chemistry classroom at East High School. Stavros Demos, Group Leader of Optical Materials Technology, brought a spectrometer into the classroom to measure the wavelength transmission of optical filter glass. Using a color scale on a large classroom monitor, the students were able to make visual assessments of the filters' transmissions in order to compare objective and subjective spectral analyses (Fig. 6).

Due to COVID 19, the BEST participants visited LLE for only one day during the last week of the summer program to tour the OMEGA and OMEGA EP lasers, optical manufacturing facilities, and other support laboratories (Fig. 7). Together, the students and teachers were exposed to elements of science and technology that underscored the importance of their normal high school curricula. In addition, this group participated in tours of optics and imaging-related departments at Monroe Community College, the Rochester Institute of Technology, and the University of Rochester.

An important aspect of the BEST program involves the students' roles as ambassadors for outreach to other students enrolled at East High and other RCSD high schools. Two projects were completed for this purpose. First, the students and teachers created a PowerPoint presentation showing the broad range of science and technology topics included in the program. Second, a photomontage video was created to show the relationship between the BEST program and the work carried out at LLE. This video was accepted as an Innovative Spotlight in the 2022 University of Rochester Equity, Diversity, and Inclusion Leadership Summit. In planning for the 2022 BEST program, students from several RCSD high schools including East High, Young Women's College Prep, Monroe Upper High, and Rochester Early College others are being invited to participate.

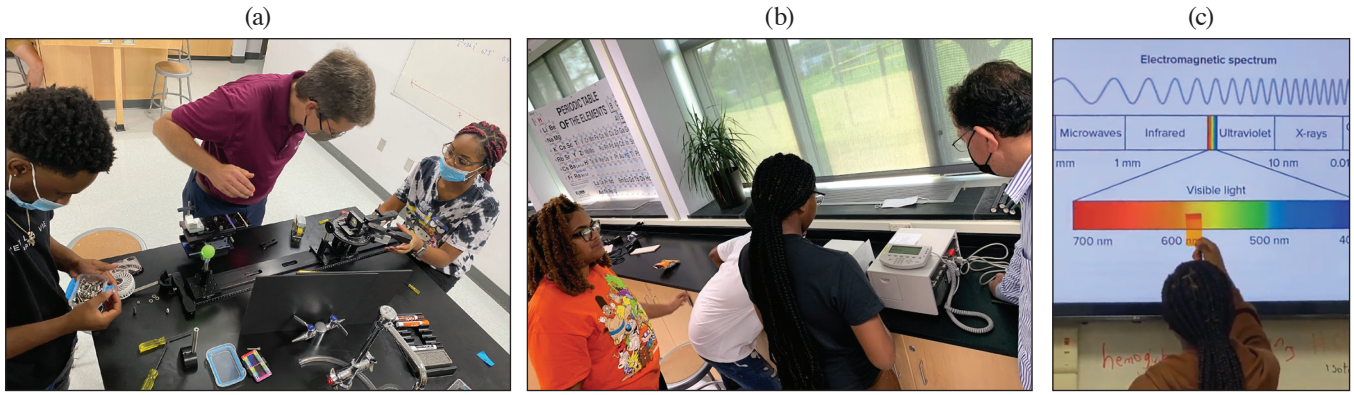

Figure 6
(a) Brian Kruschwitz, System Science Group Leader, is shown working with Ramir Wearen and Taiasia Gibson to construct a grating spectrometer. (b) Stavros Demos, Optical Materials Technology Group Leader, is shown demonstrating the procedure for operating a spectrometer to measure the wavelength transmission of optical filter glass. (c) Taiasia is shown visually comparing a glass filter to a large spectral scale.

Figure 7
The BEST students and teachers visited various LLE laboratories. (a) Amy Rigatti, Optical Manufacturing Group Leader, explains the work carried out in the coating facility. (b) Mike Campbell, LLE Director, discusses science and education with East High students Reganae Walters and Taiasia Gibson.

FY22 Q1 Laser Facility Report

J. Puth, M. Labuzeta, D. Canning, and R. T. Janezic

Laboratory for Laser Energetics, University of Rochester

During the first quarter of FY22, the Omega Facility conducted 233 target shots on OMEGA and 207 target shots on OMEGA EP for a total of 440 target shots (see Tables I and II). OMEGA averaged 10.4 target shots per operating day, averaging 91.3% Availability and 88.9% Experimental Effectiveness. OMEGA EP averaged 9.0 target shots per operating day, averaging 95.3% Availability and 94.9% Experimental Effectiveness.

Table I: OMEGA Laser System target shot summary for Q1 FY22.

Program	Laboratory	Planned Number of Target Shots	Actual Number of Target Shots
ICF	LLE	104.5	104
	LANL	11	12
	LLNL	11	6
ICF Subtotal		126.5	122
HED	LLE	11	8
	LANL	11	9
	LLNL	22	23
HED Subtotal		44	40
LBS	LLNL	22	21
LBS Subtotal		22	21
AIBS		22	17
APL		11	14
NLUF		22	19
Grand Total		247.5	233

AIBS: Academic and Industrial Basic Science
APL: Applied Physics Labs (Johns Hopkins University)
NLUF: National Laser Users Facility

Table II: OMEGA EP Laser System target shot summary for Q1 FY22.

Program	Laboratory	Planned Number of Target Shots	Actual Number of Target Shots
ICF	LLE	14	13
	LLNL	21	26
	NRL	7	9
ICF Subtotal		42	48
HED	LLE	14	16
	LANL	7	8
	LLNL	21	27
HED Subtotal		42	51
LBS	LLNL	10.5	18
	LLE	7	14
	PPPL	7	6
LBS Subtotal		24.5	38
CMAP		7	10
CEA		7	8
NLUF		31.5	39
Calibration	LLE	0	13
Grand Total		154	207

CMAP: Center for Matter at Atomic Pressures
CEA: Commissariat à l'énergie atomique et aux énergies alternatives

Publications and Conference Presentations

Publications

S.-W. Bahk, "Analytic Phase Solutions of Three-Wave Interactions," Opt. Lett. **46**, 5368 (2021).

I. A. Begishev, V. Bagnoud, S.-W. Bahk, W. A. Bittle, G. Brent, R. Cuffney, C. Dorrer, D. H. Froula, D. Haberberger, C. Mileham, P. M. Nilson, A. V. Okishev, J. L. Shaw, M. J. Shoup III, C. R. Stillman, C. Stoeckl, D. Turnbull, B. Wager, J. D. Zuegel, and J. Bromage, "Advanced Laser Development and Plasma-Physics Studies on the Multiterawatt Laser," Appl. Opt. **60**, 11,104 (2021).

M. D. Bergkoetter, B. E. Kruschwitz, S.-W. Bahk, and J. R. Fienup, "Measurement of Chromatic Aberrations Using Phase Retrieval," J. Opt. Soc. Am. A **38**, 1853 (2021).

A. F. A. Bott, L. Chen, G. Boutoux, T. Caillaud, A. Duval, M. Koenig, B. Khiar, I. Lantuéjoul, L. Le-Deroff, B. Reville, R. Rosch, D. Ryu, C. Spindloe, B. Vauzour, B. Villette, A. A. Schekochihin, D. Q. Lamb, P. Tzeferacos, G. Gregori, and A. Casner, "Inefficient Magnetic-Field Amplification in Supersonic Laser-Plasma Turbulence," Phys. Rev. Lett. **127**, 175002 (2021).

J. Bromage, S.-W. Bahk, M. Bedzyk, I. A. Begishev, S. Bucht, C. Dorrer, C. Feng, C. Jeon, C. Mileham, R. G. Roides, K. Shaughnessy, M. J. Shoup III, M. Spilatro, B. Webb, D. Weiner, and J. D. Zuegel, "MTW-OPAL: A Technology Development Platform for Ultra-Intense Optical Parametric Chirped-Pulse Amplification Systems," High Power Laser Sci. Eng. **9**, e63 (2021).

Y.-Y. Chang, X. Cheng, A. Hannasch, M. LaBerge, J. M. Shaw, K. Weichman, J. Welch, A. C. Bernstein, W. Henderson, R. Zgadzaj, and M. C. Downer, "Faraday Rotation Study of Plasma Bubbles in GeV Wakefield Accelerators," Phys. Plasmas **28**, 123105 (2021).

A. Colaïtis, I. Igumenshchev, J. Mathiaud, and V. Goncharov, "Inverse Ray Tracing on Icosahedral Tetrahedron Grids for Non-Linear Laser Plasma Interaction Coupled to 3D Radiation Hydrodynamics," J. Comput. Phys. **443**, 110537 (2021).

C. Feng, C. Dorrer, C. Jeon, R. Roides, B. Webb, and J. Bromage, "Analysis of Pump-to-Signal Noise Transfer in Two-Stage Ultra-Broadband Optical Parametric Chirped-Pulse Amplification," Opt. Express **29**, 40,240 (2021).

P. Franke, D. Ramsey, T. T. Simpson, D. Turnbull, D. H. Froula, and J. P. Palastro, "Optical Shock-Enhanced Self-Photon Acceleration," Phys. Rev. A **104**, 043520 (2021).

V. Gopalaswamy, R. Betti, J. P. Knauer, A. Lees, D. Patel, A. R. Christopherson, I. V. Igumenshchev, D. Cao, K. S. Anderson, A. Shvydky, D. H. Edgell, O. M. Mannion, C. Thomas, W. Theobald, C. Stoeckl, S. P. Regan, V. N. Goncharov, R. C. Shah, and E. M. Campbell, "Using Statistical Modeling to Predict and Understand Fusion Experiments," Phys. Plasmas **28**, 122705 (2021).

S. Heidtfeld, R. Adam, T. Kubota, K. Takanashi, D. Cao, C. Schmitz-Antoniak, D. E. Bürgler, F. Wang, C. Greb, G. Chen, I. Komissarov, H. Hardtdegen, M. Mikulics, R. Sobolewski, S. Suga, and C. M. Schneider, "Generation of Terahertz Transients from $CO_2Fe_{0.4}Mn_{0.6}Si$-Heusler-Alloy/Normal-Metal Nanobilayers Excited by Femtosecond Optical Pulses," Phys. Rev. Research **3**, 043025 (2021).

J. Jeet, A. B. Zylstra, M. Rubery, Y. Kim, K. D. Meaney, C. Forrest, V. Glebov, C. J. Horsfield, A. M. McEvoy, and H. W. Herrmann, "Inertial-Confinement Fusion-Plasma-Based Cross-Calibration of the Deuterium-Tritium γ-to-Neutron Branching Ratio," Phys. Rev. C **104**, 054611 (2021).

G. W. Jenkins, C. Feng, and J. Bromage, "Alignment Tolerance Analysis for Divided-Pulse Nonlinear Compression," J. Opt. Soc. Am. B **38**, 3199 (2021).

V. V. Karasiev, J. Hinz, S. X. Hu, and S. B. Trickey, "On the Liquid–Liquid Phase Transition of Dense Hydrogen," Nature **600**, E12 (2021).

D. I. Mihaylov, V. V. Karasiev, S. X. Hu, J. R. Rygg, V. N. Goncharov, and G. W. Collins, "Improved First-Principles Equation-of-State Table of Deuterium for High-Energy-Density Applications," Phys. Rev. B **104**, 144104 (2021).

S. F. Nwabunwanne and W. R. Donaldson, "Boosting the External Quantum Efficiency of AlGaN-Based Metal–Semiconductor–Metal Ultraviolet Photodiodes by Electrode Geometry Variation," IEEE J. Quantum Electron. **57**, 4000608 (2021).

A. M. Saunders, C. V. Stan, K. K. Mackay, B. Morgan, J. A. K. Horwitz, S. J. Ali, H. G. Rinderknecht, T. Haxhimali, Y. Ping, F. Najjar, J. Eggert, and H.-S. Park, "Experimental Observations of Laser-Driven Tin Ejecta Microjet Interactions," Phys. Rev. Lett. **127**, 155002 (2021).

A. Shvydky, A. V. Maximov, V. V. Karasiev, D. Haberberger, S. X. Hu, and V. N. Goncharov, "Ionization State and Dielectric Constant in Cold Rarefied Hydrocarbon Plasmas of Inertial Confinement Fusion," Phys. Rev. E **104**, 045207 (2021).

A. Tentori, A. Colaïtis, W. Theobald, A. Casner, D. Raffestin, A. Ruocco, J. Trela, E. Le Bel, K. Anderson, M. Wei, B. Henderson, J. Peebles, R. Scott, S. Baton, S. A. Pikuz, R. Betti, M. Khan, N. Woolsey, S. Zhang, and D. Batani, "Experimental Characterization of Hot-Electron Emission and Shock Dynamics in the Context of the Shock Ignition Approach to Inertial Confinement Fusion," Phys. Plasmas **28**, 103302 (2021).

W. Trickey, V. N. Goncharov, I. V. Igumenshchev, A. Shvydky, T. J. B. Collins, and E. M. Campbell, "Central Density and Low-Mode Perturbation Control of Inertial Confinement Fusion Dynamic-Shell Targets," Front. Phys. **9**, 784258 (2021).

C. A. Williams, R. Betti, V. Gopalaswamy, and A. Lees, "High Yields in Direct-Drive Inertial Confinement Fusion Using Thin-Ice DT Liner Targets," Phys. Plasmas **28**, 122708 (2021).

Forthcoming Publications

P. T. Campbell, C. A. Walsh, B. K. Russell, J. P. Chittenden, A. Crilly, G. Fiksel, L. Gao, I. V. Igumenshchev, P. M. Nilson, A. G. R. Thomas, K. Krushelnick, and L. Willingale, "Measuring Magnetic Flux Suppression in High-Power Laser–Plasma Interactions," to be published in Physics of Plasmas.

T. J. B. Collins, C. Stoeckl, R. Epstein, W. A. Bittle, C. J. Forrest, V. Yu. Glebov, V. N. Goncharov, D. R. Harding, S. X. Hu, D. W. Jacobs-Perkins, T. Z. Kosc, J. A. Marozas, C. Mileham, F. J. Marshall, S. F. B. Morse, P. B. Radha, S. P. Regan, B. Rice, T. C. Sangster, M. J. Shoup III, W. T. Shmayda, C. Sorce, W. Theobald, and M. D. Wittman, "Causes of Fuel–Ablator Mix Inferred from Modeling of Monochromatic Time-Gated Radiography in OMEGA Cryogenic Implosions," to be published in Physics of Plasmas.

M. F. Kasim, D. Watson-Parris, L. Deaconu, S. Oliver, P. Hatfield, D. H. Froula, G. Gregori, M. Jarvis, S. Khatiwala, J. Korenaga, J. Topp-Mugglestone, E. Viezzer, and S. M. Vinko, "Building High-Accuracy Emulators for Scientific Simulations with Deep Neural Architecture Search," to be published in Machine Learning: Science and Technology.

R. G. Kraus, R. J. Hemley, S. J. Ali, J. L. Belof, L. X. Benedict, J. Bernier, D. Braun, R. E. Cohen, G. W. Collins, F. Coppari, M. P. Desjarlais, D. Fratanduono, S. Hamel, A. Krygier, A. Lazicki, J. Mcnaney, M. Millot, P. C. Myint, M. G. Newman, J. R. Rygg, D. M. Sterbentz, S. T. Stewart, L. Stixrude, D. C. Swift, C. Wehrenberg, and J. H. Eggert, "Measuring the Melting Curve of Iron at Super-Earth Core Conditions," to be published in Science.

N. R. Shaffer and C. E. Starrett, "Dense Plasma Opacity via the Multiple-Scattering Method," to be published in Physical Review E.

R. Sobolewski, "Optical Detectors and Sensors," to be published in the Handbook of Superconducting Materials.

G. F. Swadling and J. Katz, "Novel Design for a Polarizing DUV Spectrometer Using a Wollaston Prism and Its Application as a Diagnostic for Measuring Thomson Scattering Data in the Presence of Strong Self-Emission Backgrounds," to be published in the Review of Scientific Instruments.

W. Theobald, D. Cao, R. C. Shah, C. A. Thomas, I. V. Igumenshchev, K. A. Bauer, R. Betti, M. J. Bonino, E. M. Campbell, A. R. Christopherson, K. Churnetski, D. H. Edgell, C. J. Forrest, J. A. Frenje, M. Gatu Johnson, V. Yu. Glebov, V. N. Goncharov, V. Gopalaswamy, D. R. Harding, S. X. Hu, S. T. Ivancic, D. W. Jacobs-Perkins, R. T. Janezic, T. Joshi, J. P.

Knauer, A. Lees, R. W. Luo, O. M. Mannion, F. J. Marshall, Z. L. Mohamed, S. F. B. Morse, D. Patel, J. L. Peebles, R. D. Petrasso, P. B. Radha, H. G. Rinderknecht, M. J. Rosenberg, S. Sampat, T. C. Sangster, W. T. Shmayda, C. M. Shuldberg, A. Shvydky, C. Sorce, C. Stoeckl, M. D. Wittman, and S. P. Regan, "Enhanced Laser-Energy Coupling with Small-Spot Distributed Phase Plates (SG5-650) in OMEGA DT Cryogenic Target Implosions," to be published in Physics of Plasmas.

D. Zhao, R. Betti, and H. Aluie, "Scale Interactions and Anisotropy in Rayleigh–Taylor Turbulence," to be published in the Journal of Fluid Mechanics.

Conference Presentations

The following presentations were made at Advanced Solid-State Lasers, Ontario, Canada, 3–7 October 2021:

C. Dorrer, I. A. Begishev, S.-W. Bahk, and J. Bromage, "Spatially Resolved Characterization of Partially Deuterated KDP Crystals for Parametric Amplification."

G. W. Jenkins, C. Feng, and J. Bromage, "Simultaneous Spectral Broadening and Contrast Improvement Using Divided-Pulse Nonlinear Compression."

M. Spilatro and C. Dorrer, "Versatile Spectral Shaping of Spectrally Incoherent Pulses in the IR and UV."

A. K. Schwemmlein, C. Fagan, W. T. Shmayda, M. Sharpe, C. Stoeckl, C. J. Forrest, S. P. Regan, and W. U. Schröder, "First Demonstration of a Triton Beam Using Target Normal Sheath Acceleration," presented at the American Physical Society Division of Nuclear Physics, Boston, MA, 10–14 October 2021.

D. A. Chin, P. M. Nilson, D. T. Bishel, E. Smith, X. Gong, M. K. Ginnane, B. J. Henderson, D. N. Polsin, T. R. Boehly, J. R. Rygg, G. W. Collins, D. Trail, A. Amouretti, M. Harmand, O. Mathon, R. Torchio, J. J. Ruby, F. Coppari, A. Coleman, and Y. Ping, "XANES and EXAFS Progress Studying Compressed Iron Oxides on OMEGA," presented at Matter in Extreme Conditions from Material Science to Planetary Physics, virtual, 12–13 October 2021.

The following presentations were made at Laser Damage, virtual, 12–15 October 2021:

D. Broege, S. G. Demos, C. Dorrer, K. R. P. Kafka, and M. Spilatro, "The Impact of Intensity Fluctuations on Laser Damage."

R. Dent, B. N. Hoffman, A. A. Kozlov, N. Liu, A. L. Rigatti, S. G. Demos, and A. A. Shestopalov, "Embedded Contamination Induced by Etching in E-Beam-Deposited Silica: A Possible Precursor to Laser Damage."

S. Elhadj, C. Gavin, A. Bayramian, W. Clauson, M. Murachver, J. Jarboe, D. Kissinger, C. LeBlanc, N. Urban, J. Wallace, S. Demos, and K. L. Marshall, "Large-Area, Multi-Pulse Laser Lifetime of Purified Nematic Liquid Crystals at Near-Infrared Wavelengths."

R. Jia, B. N. Hoffman, A. A. Kozlov, S. G. Demos, and A. A. Shestopalov, "Monolayer Organic Thin Films as Contamination-Resistant Coatings in Optical Elements."

K. R. P. Kafka, T. Z. Kosc, and S. G. Demos, "Methods and Apparatus for Laser Damage and Functional Performance Characterization of Ultrafast Laser Optics."

T. Z. Kosc, S. G. Demos, T. J. Kessler, H. Huang, A. Maltsev, R. Negres, and J. C. Lambropoulos, "Minimizing Risk for Laser Damage Due to Transverse Stimulated Raman Scattering in Large-Aperture KDP/DKDP Plates for Polarization Control at 3ω."

K. L. Marshall, K. R. P. Kafka, N. D. Urban, J. U. Wallace, and S. G. Demos, "The Effect of Incident Polarization Handedness and Ellipticity on the Laser-Damage Resistance of Oriented Liquid Crystals in the Nanosecond Regime."

P. Tzeferacos, "Big Computers and Big Lasers: How Concerted Numerical Simulations and Laser-Driven Laboratory Experiments Can Shed Light on Fundamental Astrophysical Processes in Turbulent Magnetized Plasmas," presented at CIRC Symposium, Rochester, 15 October 2021.

The following presentations were made at the Industrial Associates Meeting, Rochester, NY, 20–22 October 2021:

G. Chen, R. Adam, D. E. Bürgler, J. Cheng, D. Chaktraborty, I. Komissarov, S. Heidtfeld, D. Cao, H. Hardtdegen, M. Mikulics, A. Alostaz, F. Wang, M. Büscher, C. M. Schneider, L. Gladczuk, P. Przysłupki, and R. Sobolewski, "Ultrabroadband Spintronic THz Emitters Excited by Femtosecond Laser Pulse."

G. W. Jenkins, C. Feng, and J. Bromage, "Simultaneous Spectral Broadening and Contrast Improvement Using Divided-Pulse Nonlinear Compression."

E. M. Campbell, "A Vision for the Future for High-Power Laser Research and Applications," presented at OPTICSMEET 2021, Nice, France, 1–3 November 2021.

The following presentations were made at the 42nd Tritium Focus Group, Los Alamos, NM, 2–3 November 2021:

M. Sharpe and W. T. Shmayda, "Measurement of Palladium Hydride Isotherms Using H_2, D_2, and H_2/D_2 Mixtures."

W. T. Shmayda, H. Mutha, and K. Ryan, "The SPARC Tritium Fuel Cycle."

The following presentations were made at the 63rd Annual Meeting of the American Physical Society Division of Plasma Physics, Pittsburgh, PA, 8–12 November 2021:

M. B. P. Adams, P.-A. Gourdain, P. Tzeferacos, S. Feister, J. J. Pilgram, C. G. Constantin, and C. Niemann, "Exploration of Magnetic-Field Generation via Biermann Battery Using the *FLASH* Code to Model Experiments Performed at UCLA's Phoenix Laboratory."

M. V. Ambat, R. Boni, J. L. Shaw, P. Franke, K. R. McMillen, M. VanDusen-Gross, H. G. Rinderknecht, D. Ramsey, T. T. Simpson, J. P. Palastro, S.-W. Bahk, J. Bromage, and D. H. Froula, "Effects of Chromatic Aberration in a Dephasingless Laser Wakefield Accelerator."

K. S. Anderson, E. C. Hansen, J. A. Marozas, T. J. B. Collins, V. N. Goncharov, M. M. Marinak, and S. Sepke, "Computational Modeling of the Target Mounting Stalk in Direct-Drive Implosions."

A. Armstrong, A. Reyes, M. B. P. Adams, P. Farmakis, E. C. Hansen, Y. Lu, D. Michta, K. Moczulski, D. Q. Lamb, and P. Tzeferacos, "Implementation and Verification of Braginskii Viscosity in the *FLASH* Code."

J. Baltazar, R. C. Shah, D. Cao, V. Gopalaswamy, R. Betti, D. Patel, C. Stoeckl, W. Theobald, K. M. Woo, and S. P. Regan, "Diagnosing Low-Mode ($\ell \leq 6$) and Mid-Mode ($6 < \ell \leq 40$) Asymmetries in the Explosion Phase of Laser-Direct-Drive DT Cryogenic Implosions on OMEGA."

D. H. Barnak, R. Betti, V. Gopalaswamy, A. Lees, and A. Shvydky, "Understanding Shock-Release Experiments Using a Numerical Simulation of VISAR."

D. T. Bishel, P. M. Nilson, D. A. Chin, J. J. Ruby, E. Smith, S. X. Hu, J. R. Rygg, G. W. Collins, and E. V. Marley, "Utilizing Implosions to Constrain Atomic Physics of Gbar Materials."

G. Bruhaug, H. G. Rinderknecht, M. S. Wei, D. T. Bishel, G. W. Collins, J. R. Rygg, Y. E, K. Garriga, X. C. Zhang, R. Smith, A. Necas, and K. Zhai, "High-Power, High-Energy THz Generation with Joule and Kilojoule-Class Lasers."

M. Burns, R. K. Follett, A. Bowman, S. Zhai, A. Poudel, S. Dwarkadas, S. Pai, and A. B. Sefkow, "Heterogeneous Plasma Physics Codes in TriForce: Progress and Next Steps."

D. Cao, R. C. Shah, C. A. Thomas, A. Lees, V. Gopalaswamy, R. Betti, D. Patel, W. Theobald, J. P. Knauer, P. B. Radha, C. Stoeckl, S. P. Regan, W. Scullin, T. J. B. Collins, and V. N. Goncharov, "Understanding Origins of Observed Fusion-Yield Dependencies for Direct-Drive Implosions on OMEGA."

S. H. Cao, R. Betti, V. Gopalaswamy, H. Huang, D. Patel, C. Ren, M. J. Rosenberg, A. Shvydky, C. Stoeckl, and H. Wen, "Predicting Hot-Electron Generation in Inertial Confinement Fusion with Particle-in-Cell Simulations."

A. Casner, V. Bouffetier, L. Ceurvorst, G. Perez Callejo, T. Goudal, H. W. Sio, J. L. Peebles, P. Tzeferacos, V. Smalyuk, and O. A. Hurricane, "Mitigation of the Kelvin–Helmholtz Instability in HED Conditions by a Strong External Magnetic Field."

L. Ceurvorst, L. Masse, S. Khan, D. A. Martinez, N. Izumi, V. A. Smalyuk, T. Goudal, V. Bouffetier, A. Casner, B. Canaud, V. N. Goncharov, and I. V. Igumenshchev, "Effects of Ablation and Mode Coupling on the Deeply Nonlinear Stages of the Rayleigh–Taylor Instability."

D. A. Chin, P. M. Nilson, D. T. Bishel, E. Smith, R. S. Craxton, J. R. Rygg, G. W. Collins, J. J. Ruby, F. Coppari, A. Coleman, and Y. Ping, "Characterization of X-Ray Emission from Spherical Shells for X-Ray Absorption Spectroscopy Experiments on OMEGA 60."

S. Chowdry, S. Zhang, S. X. Hu, and G. Kagan, "Incorporating Quantum Electronics in Classical Calculations for Dense Plasmas."

K. Churnetski, K. M. Woo, W. Theobald, P. B. Radha, R. Betti, V. Gopalaswamy, I. V. Igumenshchev, S. T. Ivancic, M. Michalko, R. C. Shah, C. Stoeckl, C. A. Thomas, and S. P. Regan, "Three-Dimensional Hot-Spot Reconstruction from Cryogenic DT Polar-Direct-Drive Implosions on OMEGA."

A. Colaïtis, D. H. Edgell, I. V. Igumenshchev, D. Turnbull, J. P. Palastro, R. K. Follett, V. N. Goncharov, and D. H. Froula, "Low-Mode Asymmetry Induced by Polarized Cross-Beam Energy Transfer Interaction in Laser-Direct-Drive Spherical Implosions on OMEGA."

T. J. B. Collins, P. M. Nilson, R. Epstein, D. T. Bishel, D. A. Chin, J. J. Ruby, J. Kendrick, D. Guy, S. T. Ivancic, F. J. Marshall, C. Stoeckl, V. N. Goncharov, and D. H. Froula, "Theory and Modeling of Blast-Wave–Driven Interfacial Hydrodynamic Instability in OMEGA Planar Experiments."

R. S. Craxton, W. Y. Wang, M. A. Marangola, and E. M. Campbell, "A Dual Laser-Beam Configuration Compatible with Both Symmetric Direct Drive and Spherical Hohlraums."

J. R. Davies, D. H. Barnak, E. C. Hansen, P. V. Heuer, L. S. Leal, J. L. Peebles, and A. Birkel, "Evaluation of Direct Inversion of Proton Radiographs in the Context of Cylindrical Implosions."

A. Diaw, N. M. Cook, S. Coleman, J. P. Edelen, E. C. Hansen, and P. Tzeferacos, "Resistivity and Heat Conduction Modeling in Capillary Discharges."

D. H. Edgell, A. Colaitis, R. S. Craxton, R. K. Follett, M. J. Guardalben, A. Kalb, J. Katz, J. Kwiatkowski, O. M. Mannion, P. B. Radha, A. Shvydky, C. Stoeckl, D. Turnbull, and D. H. Froula, "Nonuniformity in Direct-Drive Implosions Caused by Polarization Smoothing" (invited).

R. Ejaz, V. Gopalaswamy, and R. Betti, "A Deep Learning Approach to Design Inertial Confinement Fusion Experiments."

R. Epstein, V. N. Goncharov, S. X. Hu, D. Cao, A. Shvydky, P. W. McKenty, G. W. Collins, D. Haberberger, J. L. Kline, and S. M. Finnegan, "Assessment of Radiation Trapping in Inertial Confinement Fusion Implosion Experiments with High-*Z*–Lined, Single-Shell Targets."

P. Farmakis, M. McMullan, A. Reyes, J. Laune, M. B. P. Adams, A. Armstrong, E. C. Hansen, Y. Lu, D. Michta, K. Moczulski, D. Lamb, and P. Tzeferacos, "Expanding the Tabulated Equation-of-State Implementations in the *FLASH* Code for the *SESAME* Database."

R. K. Follett, H. Wen, J. G. Shaw, D. H. Froula, A. V. Maximov, A. A. Solodov, D. Turnbull, J. P. Palastro, J. F. Myatt, and J. W. Bates, "A Local-Field Approach to Understanding Multibeam Laser–Plasma Instabilities."

C. J. Forrest, D. Cao, V. N. Glebov, V. N. Goncharov, V. Gopalaswamy, J. P. Knauer, O. M. Mannion, Z. L. Mohamed, S. P. Regan, R. C. Shah, C. Stoeckl, and K. M. Woo, "Inference of Isotropic and Anisotropic Flow in Laser Direct-Drive Cryogenic DT Implosions on OMEGA."

P. Franke, D. Ramsey, T. T. Simpson, D. Turnbull, D. H. Froula, and J. P. Palastro, "Optical Shock-Enhanced Self-Photon Acceleration."

F. García-Rubio, R. Betti, J. Sanz, and H. Aluie, "Magneto-hydrodynamic Instabilities in Ablation Fronts and Coronal Plasmas" (invited).

M. Gatu Johnson, P. J. Adrian, J. A. Frenje, T. M. Johnson, N. Kabadi, B. G. Lahmann, R. Petrasso, W. J. Garbett, R. S. Craxton, M. Hohenberger, H. D. Whitley, C. B. Yeamans, and A. B. Zylstra, "Measurement of Hot-Electron-Driven Fast Ions in Polar-Direct-Drive Exploding-Pusher Implosions on the NIF."

M. K. Ginnane, D. N. Polsin, X. Gong, M. C. Marshall, T. R. Boehly, J. R. Rygg, G. W. Collins, A. Lazicki, R. Kraus, J. H. Eggert, D. E. Fratanduono, J. P. Davis, C. A. McCoy, C. Seagle, and S. Root, "X-Ray Diffraction Measurements of Shocked and Shock-Ramped Platinum."

V. N. Goncharov, I. V. Igumenshchev, W. Trickey, N. Shaffer, K. M. Woo, T. J. B. Collins, E. M. Campbell, and Y. Lawrence, "Mitigating Deceleration Rayleigh–Taylor Growth in Inertial Confinement Fusion Designs."

X. Gong, D. N. Polsin, R. Paul, M. C. Marshall, M. K. Ginnane, B. J. Henderson, J. R. Rygg, G. W. Collins, and J. H. Eggert, "X-Ray Diffraction of Ramp-Compressed Silicon."

V. Gopalaswamy, R. Betti, J. P. Knauer, D. Patel, A. Lees, K. M. Woo, C. A. Thomas, D. Cao, O. M. Mannion, R. C. Shah, C. J. Forrest, Z. L. Mohamed, C. Stoeckl, V. N. Glebov, S. P. Regan, D. H. Edgell, M. J. Rosenberg, I. V. Igumenshchev, P. B. Radha, K. S. Anderson, J. R. Davies, T. J. B. Collins, V. N. Goncharov, K. Churnetski, W. Theobald, E. M. Campbell, R. T. Janezic, D. R. Harding, M. J. Bonino, S. Sampat, K. A. Bauer, S. F. B. Morse, M. Gatu Johnson, R. D. Petrasso, C. K. Li, and J. A. Frenje, "Advances Toward Hydro-Equivalent Ignition in OMEGA Direct-Drive Implosions" (invited).

D. Haberberger, A. Shvydky, S. T. Ivancic, V. N. Goncharov, C. Stoeckl, and D. H. Froula, "Schlieren Refraction Measurements of Implosion Density Profiles."

E. C. Hansen, M. B. P. Adams, A. Armstrong, J. R. Davies, P. Farmakis, F. García-Rubio, Y. Lu, D. Michta, K. Moczulski, C. Ren, A. C. Reyes, A. Sefkow, H. Wen, P. Tzeferacos, S. Langendorf, P. Ney, H. Rahman, and E. Ruskov, "Extended Magnetohydrodynamics in the *FLASH* Code."

B. J. Henderson, M. C. Marshall, J. R. Rygg, D. N. Polsin, L. E. Hansen, M. K. Ginnane, and G. W. Collins, "Thermal Emission and Reflectivity of Shocked SiO_2 Aerogel for Broadband Optical Probing."

P. V. Heuer, L S. Leal, J. R. Davies, E. C. Hansen, D. H. Barnak, J. L. Peebles, and A. Birkel, "Proton Radiography of Self-Generated Magnetic Fields in Laser-Driven Cylindrical Implosions."

P. V. Heuer, Y. Zhang, C. Ren, J. R. Davies, D. B. Schaeffer, M. S. Weidl, C. Niemann, W. Fox, and D. Caprioli, "Studying Quasi-Parallel Collisionless Shocks in the Laboratory."

S. X. Hu, P. M. Nilson, D. T. Bishel, D. A. Chin, V. V. Karasiev, I. E. Golovkin, M. Gu, T. Walton, and S. B. Hansen, "Probing Extreme Atomic Physics at Petapascal Pressures."

M. Huff, J. R. Rygg, G. W. Collins, T. R. Boehly, D. N. Polsin, M. Nakajima, B. J. Henderson, M. C. Marshall, T. A. Suer, D. E. Fratanduono, M. Millot, R. F. Smith, C. A. McCoy, and L. E. Hansen, "Measurements of Sound Speed in Iron Shock-Compressed Iron to ~3000 GPa."

I. V. Igumenshchev, V. N. Goncharov, E. M. Campbell, T. J. B. Collins, M. J. Rosenberg, N. Shaffer, W. Theobald, W. Trickey, R. C. Shah, A. Shvydky, A. Colaïtis, S. Atzeni, and L. Savino, "Dynamic Shell Stability to Low-Mode Perturbations."

S. T. Ivancic, W. Theobald, K. Churnetski, M. Michalko, R. Spielman, S. P. Regan, A. Raymond, J. D. Kilkenny, A. Carpenter, C. Trosseille, D. K. Bradley, J. D. Hares, A. K. L. Dymoke Bradshaw, G. Rochau, M. Sanchez, and D. Garand, "Design of the Third X-Ray Line of Sight for OMEGA."

T. R. Joshi, R. C. Shah, W. Theobald, I. V. Igumenshchev, J. Baltazar, D. Cao, and S. P. Regan, "Analysis of Modulations Observed in X-Ray Self-Emission Images of OMEGA Direct-Drive Inertial Confinement Fusion Implosions."

V. V. Karasiev, D. I. Mihaylov, S. X. Hu, S. B. Trickey, and J. W. Dufty, "Advancing the Accuracy of DFT Simulations for High-Energy-Density Plasmas by Developing Temperature-Dependent Exchange-Correlation Functionals" (invited).

J. Katz, A. L. Milder, D. Turnbull, S. T. Ivancic, D. H. Froula, M. Sherlock, P. Michel, L. Divol, D. Strozzi, and W. Rozmus, "Direct Measurements of Laser Absorption in Undersense Plasmas on OMEGA."

A. Kish, J. G. Shaw, M. Lavell, A. Sexton, and A. B. Sefkow, "Software Architecture Design for Modular Multiphysics Simulations."

J. P. Knauer, C. J. Forrest, Z. L. Mohamed, K. M. Woo, O. M. Mannion, I. V. Igumenshchev, R. Betti, V. Gopalaswamy, P. B. Radha, S. P. Regan, W. Theobald, M. Gatu Johnson, J. A. Frenje, A. J. Crilly, and B. D. Appelbe, "Effect of Mode-1 Perturbations on OMEGA Areal-Density Measurements."

M. J. Lavell, J. G. Shaw, A. Kish, A. Sexton, A. Srinivasan, S. Sikorski, and A. B. Sefkow, "Coulomb Collision Models for PIC Simulations of Field Reversed Configurations and Beam-Plasma Interactions."

Y. Lawrence, V. N. Goncharov, W. Trickey, I. V. Igumenshchev, K. Woo, and J. Carroll-Nellenback, "Deceleration Phase Rayleigh–Taylor Growth in Dynamic Shell ICF Designs."

Y. Lawrence, R. D. McBride, and A. B. Sefkow, "Transport Coefficient Sensitivities in a Semi-Analytic Model for MagLIF."

L. S. Leal, J. L. Peebles, D. H. Barnak, J. R. Davies, A. V. Maximov, E. C. Hansen, P. V. Heuer, A. B. Sefkow, and R. Betti, "Simulations of Ti-Layered Magnetized Liner Inertial Fusion Implosions on OMEGA Investigating the Effect of Mix."

A. Lees, D. Barnak, R. Betti, V. Gopalaswamy, A. Shvydky, and Z. K. Sprowal, "Measurements of Shock-Release Dynamics in Polystyrene Foils."

Y. Lu, S. Feister, J. Meinecke, F. Miniati, G. Gregori, A. Bott, A. Reyes, E. C. Hansen, J. T. Laune, B. Reville, J. S. Ross, D. Q. Lamb, and P. Tzeferacos, "Numerical Modeling of Laser-Driven Plasma Experiments Aiming to Study Turbulent Dynamo and Thermal Conduction at the National Ignition Facility."

O. M. Mannion, C. J. Forrest, V. Yu. Glebov, J. P. Knauer, P. W. McKenty, Z. L. Mohamed, S. P. Regan, C. Stoeckl, B. D. Appelbe, A. J. Crilly, W. T. Taitano, B. Keenan, P. Adrian, J. A. Frenje, N. Kabadi, and M. Gatu Johnson, "Fusion Neutron Energy Spectrum Measurements in Kinetic Plasmas."

M. J.-E. Manuel, M. Ghosh, R. Jonnalagadda, F. N. Beg, M. B. Adams, P. Tzeferacos, C. M. Huntington, B. Remington, J. S. Ross, D. D. Ryutov, H. W. Sio, G. F. Swadling, S. Wilks, and H.-S. Park, "Experimental Evidence of Early-Time Linear-Saturation of the Ion-Weibel Instability in Counter-streaming Plasmas."

J. A. Marozas, P. W. McKenty, T. J. B. Collins, M. J. Rosenberg, H. G. Rinderknecht, S. P. Regan, E. M. Campbell, C. B. Yeamans, B. E. Blue, L. Divol, G. E. Kemp, and H. D. Whitley, "National Ignition Facility Polar-Direct-Drive Exploding-Pusher Experiments—Improving Performance via Imprint Mitigation."

A. V. Maximov, D. Turnbull, R. K. Follett, D. H. Edgell, J. G. Shaw, H. Wen, D. H. Froula, and J. P. Palastro, "Absorption of Laser Light by Coupling to Incoherent Plasma Waves at Quarter-Critical Density."

P. W. McKenty, J. A. Marozas, T. J. B. Collins, M. J. Rosenberg, G. E. Kemp, C. B. Yeamans, and L. Divol, "Examining the Role of Cross-Beam Energy Transfer in NIF Direct-Drive Exploding-Pusher Experiments."

B. McLellan, S. Zhang, and S. X. Hu, "Revealing the Atomic Motion Composing the B1–B2 Structural Transformation of MgO Under High Pressures."

K. R. McMillen, M. V. Ambat, Z. Barfield, J. Pigeon, D. Haberberger, D. H. Froula, and J. L. Shaw, "Plasma Characterization for Raman Amplification."

D. Michta, P. Tzeferacos, F. Graziani, and G. W. Hammett, "A Many-Body Extension to Madelung Quantum Hydrodynamics."

D. I. Mihaylov, V. V. Karasiev, S. X. Hu, J. R. Rygg, V. N. Goncharov, and G. W. Collins, "Improved First-Principles Equation-of-State Table of Deuterium for High-Energy-Density Science Applications."

A. L. Milder, J. Katz, J. P. Palastro, D. H. Edgell, A. M. Hansen, D. Turnbull, D. H. Froula, M. Sherlock, and W. Rozmus, "Measurements of the Return-Current Instability with Ion-Acoustic Thomson Scattering."

S. C. Miller, V. N. Goncharov, T. J. B. Collins, and A. Shvydky, "Internal Perturbation Evolution and Amplification During the Early Phase of Inertial Confinement Fusion Implosions."

K. Moczulski, A. Reyes, M. B. P. Adams, A. Armstrong, P. Farmakis, E. C. Hansen, Y. Lu, D. Michta, D. Lamb, and P. Tzeferacos, "Implementation and Verification of LC Circuit for Z-Pinch *FLASH* Simulations."

Z. L. Mohamed, J. P. Knauer, A. Sorce, R. B. Brannon, R. T. Janezic, W. T. Shmayda, Y. H. Kim, K. Meaney, H. Geppert-Kleinrath, N. M. Hoffman, M. S. Rubery, A. B. Zylstra, and J. Jeet, "S-Factor Measurements for Gamma-Channel Fusion Reactions."

K. L. Nguyen, L. Yin, B. J. Albright, A. M. Hansen, D. Turnbull, R. K. Follett, D. H. Froula, and J. P. Palastro, "Cross-Beam Energy Transfer Saturation by Ion-Trapping–Induced Detuning."

K. Nichols, A. J. White, L. A. Collins, and S. X. Hu, "Investigating the Stopping Power of Warm Dense Plasmas Using Time-Dependent Mixed Density-Functional Theory."

P. M. Nilson, F. J. Marshall, T. J. B. Collins, R. Epstein, D. T. Bishel, D. A. Chin, J. J. Ruby, J. Kendrick, D. Guy, S. T. Ivancic, C. Stoeckl, V. N. Goncharov, and D. H. Froula, "High-Resolution X-Ray Imaging of Shock-Driven Interface Instabilities."

R. W. Paddock, R. H. Scott, W. J. Garbett, B. M. Haines, A. B. Zylstra, T. J. B. Collins, R. S. Craxton, and P. A. Norreys, "A Pathway Toward Burning Plasmas Through Low-Convergence-Ratio Direct-Drive ICF Implosions."

J. P. Palastro, P. Franke, D. H. Froula, L. Nguyen, D. Ramsey, and T. T. Simpson, "High Harmonic Generation Driven by a Flying Focus."

H. Pantell, L. E. Hansen, G. Tabak, M. F. Huff, G. Bruhaug, J. R. Rygg, and G. W. Collins, "Isotope Effects on High-Pressure Water."

D. Patel, R. Betti, C. Stoeckl, M. J. Rosenberg, V. Gopalaswamy, J. P. Knauer, S. P. Regan, W. Theobald, V. Yu. Glebov, and A. R. Christopherson, "Analysis of Hot-Electron Preheat of High-Performing OMEGA Cryogenic Implosions."

J. L. Peebles, J. R. Davies, D. H. Barnak, P. V. Heuer, L. S. Leal, F. J. Marshall, V. Yu. Glebov, and R. Betti, "Measurements of Laser-Preheat–Induced Mix in Scaled Magnetized Liner Inertial Fusion (MagLIF) Implosions."

D. N. Polsin, X. Gong, M. F. Huff, L. E. Hansen, B. J. Henderson, R. Paul, S. Burns, G. W. Collins, J. R. Rygg, A. Lazicki, F. Coppari, R. Smith, M. Millot, J. H. Eggert, M. I. McMahon, X. Wang, K. Hilleke, and E. Zurek, "Probing a New Regime of Extreme Chemistry at High-Energy-Density Conditions: Na as a Prototypical Example" (invited).

H. Poole, D. Cao, R. Epstein, I. Golovkin, T. Walton, S. X. Hu, M. Kasim, S. Vinko, J. R. Rygg, V. N. Goncharov, G. Gregori, and S. P. Regan, "A Feasibility Study of Using X-Ray Thomson Scattering to Diagnose the In-Flight Plasma Conditions of DT Cryogenic Implosions."

P. B. Radha, C. Stoeckl, W. Theobald, M. J. Rosenberg, M. Porcelli, R. Betti, E. M. Campbell, D. H. Edgell, V. N. Goncharov, J. P. Knauer, S. P. Regan, A. Shvydky, and A. A. Solodov, "Validation of Energy Coupling Models from kJ to MJ Scale."

D. Ramsey, P. Franke, D. H. Froula, T. T. Simpson, K. Weichman, J. P. Palastro, B. Malaca, M. Pardal, J. Vieira, A. Di Piazza, and M. Formanek, "Nonlinear Thomson Scattering with Ponderomotive Control."

S. P. Regan, O. M. Mannion, C. J. Forrest, H. McClow, Z. L. Mohamed, A. Kalb, J. Kwiatkowski, J. P. Knauer, C. Stoeckl, R. C. Shah, V. Yu. Glebov, W. Theobald, K. Churnetski, R. Betti, V. Gopalaswamy, H. G. Rinderknecht, I. V. Igumenshchev, P. B. Radha, V. N. Goncharov, D. H. Edgell, J. Katz, D. Turnbull, D. H. Froula, M. J. Bonino, D. R. Harding, C. M. Shuldberg, R. W. Luo, M. Hoppe, A. Colaïtis, and E. M. Campbell, "Systematic Trends of Hot-Spot Flow Velocity in Laser-Direct-Drive Implosions on OMEGA."

C. Ren, H. Wen, E. C. Hansen, S. J. Langendorf, D. Michta, and P. Tzeferacos, "PIC Simulations of Colliding Plasma Jets in Plasma Liner Experiment."

A. Reyes, M. B. P. Adams, A. Armstrong, K. Moczulski, P. Farmakis, E. C. Hansen, Y. Lu, D. Michta, P. Tzeferacos, J. Grove, and D. Q. Lamb, "Implementation of a 2-D Unsplit Volume of Fluid Interface—Capturing Method for Multifluid Compressible Flows in the *FLASH* Code."

H. G. Rinderknecht, M. S. Wei, G. Bruhaug, K. Weichman, J. P. Palastro, J. D. Zuegel, A. Arefiev, T. Wang, T. Toncian, A. Laso Garcia, D. Doria, K. Spohr, H. J. Quevedo, T. Ditmire, J. Williams, A. Haid, and D. Stutman, "Relativistically Transparent Magnetic Filament: A Laser-Plasma Platform for Efficient Electron Acceleration and MeV Photon Radiation."

M. J. Rosenberg, A. A. Solodov, A. R. Christopherson, R. Betti, P. B. Radha, C. Stoeckl, C. J. Forrest, V. Yu. Glebov, F. J. Marshall, S. P. Regan, T. J. B. Collins, D. H. Froula, J. P. Palastro, V. N. Goncharov, M. Hohenberger, B. Bachmann, G. N. Hall, P. Michel, and C. Krauland "Hot-Electron Preheat in Hydrodynamically Scaled Direct-Drive Implosions at the National Ignition Facility and OMEGA."

J. R. Rygg, G. W. Collins, and P. M. Celliers, "Plasma Waves and the Compressibility of Warm Dense Hydrogen."

M. J. Schmitt, B. S. Scheiner, D. Schmidt, L. Kot, B. Keenan, M. J. Rosenberg, P. W. McKenty, and R. S. Craxton, "Ablative Energetics of Large-Capsule, Low-Intensity Direct-Drive Implosions at the National Ignition Facility."

A. K. Schwemmlein, C. E. Fagan, W. T. Shmayda, M. Sharpe, C. Stoeckl, C. J. Forrest, S. P. Regan, and W. U. Schröder, "First Demonstration of a Triton Beam Using Target Normal Sheath Acceleration."

A. B. Sefkow, J. G. Shaw, A. Kish, M. Lavell, R. Masti, A. Sexton, S. Borve, A. Bowman, M. Burns, J. Carroll-Nellenback, S. Cohen, J. R. Davies, S. Dwarkadas, E. Evans,

R. K. Follett, M. Haddad, K. Hemsley, A. Kokash, Y. Lawrence, B. G. Logan, R. L. McCrory, A. Nahar, J. H. Nuckolls, S. Pai, A. Poudel, T. Seabourne, W. Scullin, S. Sikorski, A. Srinivasan, H. Stojkovic, A. Velberg, K. Yanik, and S. Zhai, "Overview of TriForce: Projects, Progress, and Plans."

N. R. Shaffer, A. V. Maximov, V. N. Goncharov, and M. Sherlock, "Impact of Bandwidth on the Electron Distribution Functions of Laser-Produced Plasmas."

R. C. Shah, D. Cao, R. Epstein, M. J. Rosenberg, W. Theobald, V. Gopalaswamy, R. Betti, S. P. Regan, P. Volegov, and B. Bachmann, "Mix, Temperature, and Compression of Statistical Model Optimized Cryogenic Implosions."

J. L. Shaw, G. Bruhaug, M. Freeman, F. Merrill, V. Geppert-Kleinrath, and C. Wilde, "Electron Radiography Based on Electron Beams from Laser-Plasma Accelerators."

A. Shvydky, J. L. Peebles, M. J. Rosenberg, A. V. Maximov, K. S. Anderson, V. N. Goncharov, J. A. Marozas, P. W. McKenty, P. B. Radha, S. P. Regan, T. C. Sangster, M. Hohenberger, J. M. Di Nicola, J. M. Koning, M. M. Marinak, L. Masse, M. Karasik, and L. Antonelli, "National Ignition Facility Planar Imprint Experiments."

T. T. Simpson, D. Ramsey, P. Franke, M. V. Ambat, K. Weichman, D. Turnbull, D. H. Froula, and J. P. Palastro, "Spatiotemporal Control of Laser Intensity Through Cross-Phase Modulation."

A. A. Solodov, M. J. Rosenberg, M. Stoeckl, R. Betti, W. Seka, R. Epstein, C. Stoeckl, R. K. Follett, P. B. Radha, S. P. Regan, D. H. Froula, J. P. Palastro, V. N. Goncharov, A. R. Christopherson, B. Bachmann, M. Hohenberger, P. Michel, and J. F. Myatt, "Hot-Electron Preheat and Mitigation in Polar-Direct-Drive Experiments at the National Ignition Facility."

Z. K. Sprowal, L. E. Hansen, M. Zaghoo, J. R. Rygg, T. R. Boehly, D. N. Polsin, M. Huff, G. W. Collins, D. G. Hicks, and P. M. Celliers, "Accessing High Density States in D_2 Using Double Shock."

C. Stoeckl, W. Theobald, P. B. Radha, T. Filkins, and S. P. Regan, "Energy-Coupling Experiments Using Solid Spheres in the Polar-Direct-Drive Configuration on OMEGA."

G. Tabak, M. A. Millot, S. Hamel, T. Ogawa, P. M. Celliers, D. E. Fratanduono, A. Lazicki, D. Swift, S. Brygoo, P. Loubeyre, T. R. Boehly, N. Dasenbrock-Gammon, R. Dias, L. E. Hansen, B. J. Henderson, M. Zaghoo, S. Ali, R. Kodama, K. Miyanishi, N. Ozaki, T. Sano, R. Jeanloz, D. G. Hicks, G. W. Collins, J. H. Eggert, and J. R. Rygg, "Equation of State and Metallization of Methane Shock Compressed to 400 GPa."

W. Theobald, M. J. Rosenberg, P. B. Radha, S. P. Regan, C. Stoeckl, L. Ceurvorst, R. Betti, K. S. Anderson, J. A. Marozas, V. N. Goncharov, E. M. Campbell, C. M. Shuldberg, R. W. Luo, W. Sweet, D. N. Kaczala, B. Bachmann, T. Döppner, M. Hohenberger, R. Scott, and A. Colaïtis, "Laser-Direct-Drive Energy Coupling at 4×10^{14} W/cm^2 to 1.2×10^{15} W/cm^2 from Spherical Solid-Plastic Implosions at the National Ignition Facility."

C. A. Thomas, W. Theobald, J. P. Knauer, C. Stoeckl, T. J. B. Collins, V. N. Goncharov, R. Betti, E. M. Campbell, K. S. Anderson, K. A. Bauer, D. Cao, R. S. Craxton, D. H. Edgell, R. Epstein, C. J. Forrest, V. Yu. Glebov, V. Gopalaswamy, I. V. Igumenshchev, S. T. Ivancic, D. W. Jacobs-Perkins, R. T. Janezic, T. Joshi, J. Kwiatkowski, A. Lees, F. J. Marshall, M. Michalko, Z. L. Mohamed, D. Patel, J. L. Peebles, P. B. Radha, S. P. Regan, H. G. Rinderknecht, M. J. Rosenberg, S. Sampat, T. C. Sangster, R. C. Shah, K. L. Baker, A. L. Kritcher, M. Tabak, M. C. Herrmann, A. R. Christopherson, and O. M. Mannion, "Laser-Direct-Drive Cryogenic Implosion Performance on OMEGA Versus Target and Laser-Spot Radius."

W. Trickey, V. N. Goncharov, E. M. Campbell, T. J. B. Collins, M. J. Rosenberg, N. Shaffer, W. Theobald, R. C. Shah, A. Shvydky, I. V. Igumenshchev, A. Colaïtis, S. Atzeni, and L. Savino, "Optimization of Beam-Port Configurations to Minimize Low-Mode Perturbations in High-Yield Inertial Confinement Fusion Targets."

W. Trickey, R. H. H. Scott, and N. Woolsey, "Shock-Augmented Ignition Using Indirect Drive."

P. Tzeferacos, A. Reyes, Y. Lu, A. Armstrong, K. Moczulski, G. Gregori, J. Meinecke, H. Poole, L. Chen, T. Campbell, A. Bell, S. Sarkar, F. Miniati, A. Schekochihin, D. Lamb, D. H. Froula, J. Katz, D. Haberberger, D. Turnbull, S. Fess, H.-S. Park, J. S. Ross, T. Doeppner, J. Emig, C. Goyon, D. Ryutov, B. Remington, A. Zylstra, C.-K. Li, A. Birkel, R. D. Petrasso, H. Sio, F. H. Séguin, A. F. A. Bott, C. Palmer, B. Khiar, S. Feister, A. Casner, D. Ryu, B. Reville, C. J. Forrest, J. Foster, Y. Sakawa, F. Fiuza, E. Churazov, R. Bingham, T. White, and E. Zweibel, "Strong Suppression of Heat Conduction in Laser-Driven Magnetized Turbulent Plasmas."

M. VanDusen-Gross, K. Weichman, D. R. Harding, A. Arefiev, J. Williams, A. Haid, and H. G. Rinderknecht, "Design of Experiments to Study Relativistically Transparent Magnetic Filaments Using OMEGA EP."

K. Weichman, A. V. Arefiev, H. Mao, F. N. Beg, J. P. Palastro, A. P. L. Robinson, M. Murakami, S. Fujioka, J. J. Santos, T. Toncian, T. Ditmire, H. Quevedo, Y. Shi, and V. V. Ivanov, "Effects of Kilotesla-Level Applied Magnetic Fields on Relativistic Laser–Plasma Interactions" (invited).

H. Wen, R. K. Follett, A. V. Maximov, and J. P. Palastro, "Mitigation of Inflationary Stimulated Raman Scattering with Laser Bandwidth."

C. A. Williams, R. Betti, V. Gopalaswamy, A. Lees, J. P. Knauer, C. J. Forrest, D. Patel, S. Sampat, R. T. Janezic, D. Cao, O. M. Mannion, P. B. Radha, S. P. Regan, R. C. Shah, C. A. Thomas, W. Theobald, and K. M. Woo, "Improving Performance and Understanding of Direct-Drive Inertial Fusion Implosions Using Statistical Modeling of Experimental Data."

K. M. Woo, R. Betti, C. A. Thomas, C. Stoeckl, K. Churnetski, C. J. Forrest, Z. L. Mohamed, B. Zirps, S. P. Regan, T. J. B. Collins, W. Theobald, R. C. Shah, O. M. Mannion, D. Patel, D. Cao, J. P. Knauer, V. N. Goncharov, P. B. Radha, H. G. Rinderknecht, R. Epstein, V. Gopalaswamy, and F. J. Marshall, "Three-Dimensional Hot-Spot Reconstruction in Inertial Fusion Implosions."

S. Zhang, M. C. Marshall, J. R. Rygg, A. Shvydky, D. Haberberger, V. N. Goncharov, T. R. Boehly, G. W. Collins, S. X. Hu, D. E. Fratanduono, and A. Lazicki, "Species Separation in Polystyrene Shock Release Evidenced by Molecular-Dynamics Simulations and Laser-Drive Experiments."

Y. Zhang, P. V. Heuer, J. R. Davies, and C. Ren, "Magnetized Collisionless Shock Formation Mediated by the Modified-Two-Stream Instability."

D. E. Keller and V. V. Karasiev, "VASP 6.2.1 Runtime Comparison for Extreme Thermodynamic Condition Simulations Using Graphics-Processing Units," presented at the 12th IEEE Workshop on Performance Modeling, Benchmarking, and Simulation of High-Performamce Computer Systems, virtual, 14–19 November 2021.

C. Deeney, "The Laboratory for Laser Energetics: An Overview," presented at the L3Harris visit, Rochester, NY, 15 November 2021.

E. M. Campbell, "Inertial Fusion Energy: Opportunities and Challenges," presented at the Inertial Fusion Energy Workshop, Livermore, CA, 16 November 2021.

C. Deeney, "The Laboratory for Laser Energetics: An Overview," presented at the Danny Lowe visit, Rochester, NY, 16 November 2021.

The following presentations were made at the OES Annual Meeting, virtual, 17–18 November 2021:

E. M. Campbell, "ICF-Facility Operations LLE 10.7."

S. P. Regan, "ICF Diagnostics and Instrumentation: LLE."

T. C. Sangster, "MTE 10.8."

M. Wang and D. R. Harding, "Mechanical Properties of Micrometer-Size Foam-Like Auxetic Structures," presented at the MRS Fall Meeting, Boston, MA, 28 November–3 December 2021.

E. M. Campbell, "Principles of Inertial Confinement Fusion," presented at the NROTC visit, Rochester, NY, 1 December 2021.

The following presentations were made at the Cooperative Agreement Review Meeting, Rochester, NY, 6–7 December 2021:

E. M. Campbell, "The Laboratory for Laser Energetics: An Overview of the FY19–FY23 Cooperative Agreement."

G. W. Collins, "HEDS Curriculum and Mentoring at the University of Rochester."

G. W. Collins, S. X. Hu, and J. R. Rygg, "Laboratory for Laser Energetics Contributions to the Stockpile Stewardship Mission."

C. Deeney and E. M. Campbell, "The Laboratory for Laser Energetics: Our Cooperative Agreement Going Forward."

V. N. Goncharov, "Review of Ignition Science Campaigns."

V. Gopalaswamy, R. Betti, J. P. Knauer, D. Patel, A. Lees, K. M. Woo, C. A. Thomas, D. Cao, O. M. Mannion, R. C. Shah, C. J. Forrest, Z. L. Mohamed, C. Stoeckl, V. Yu. Glebov, S. P. Regan, D. H. Edgell, M. J. Rosenberg, I. V. Igumenshchev, P. B. Radha, K. S. Anderson, J. R. Davies, T. J. B. Collins, V. N. Goncharov, E. M. Campbell, R. T. Janezic, D. R. Harding, M. J. Bonino, S. Sampat, K. A. Bauer, S. F. B. Morse, M. Gatu Johnson, R. D. Petrasso, C. K. Li, and J. A. Frenje, "OMEGA DT Cryogenic Implosion Progress."

D. R. Harding, A. Behlok, M. J. Bonino, T. Cracium, S. Fess, J. Fooks, S. Karim, I. Knudsen, K. Lintz, N. Redden, D. Wasilewski, M. Wittman, Y. Lu, P. Fan, and X. Huang, "Target Production and Development at LLE."

S. X. Hu, "Highlights of Recent Progress in High-Energy-Density Physics Theory/Computation at LLE."

S. F. B. Morse, "Omega Facility Performance FY19–FY23."

S. P. Regan, "DOE Cooperative FY19–FY23 Agreement: Diagnostic Development (10.3)."

J. R. Rygg, D. N. Polsin, X. Gong, M. C. Marshall, G. W. Collins, J.-P. Davis, C. McCoy, C. Seagle, A. Lazicki, R. Kraus, J. H. Eggert, and D. E. Fratanduono, "High-Energy-Density Experiments: Case Studies."

C. Sorce, "Engineering, Information Technology and Cybersecurity, and Safety."

S. Stagnitto, "University of Rochester Support of the Laboratory for Laser Energetics' Research Portfolio."

D. Turnbull, "Laser–Plasma Instabilities: Deep Dive."

M. S. Wei, "Education and User Access."

J. D. Zuegel, "Laser and Materials Technology Division and Major Projects."

The following presentations were made at the National Diagnostic Workshop, virtual, 7–9 December 2021:

S. T. Ivancic, W. Theobald, K. Churnetski, M. Michalko, R. Spielman, S. P. Regan, A. Raymond, J. D. Kilkenny, A. Carpenter, C. Trosseille, D. K. Bradley, J. D. Hares, A. K. L. Dymoke-Bradshaw, G. Rochau, M. Sanchez, and D. Garand, "Design of the Third X-Ray Line of Sight for OMEGA."

A. L. Milder, J. Katz, R. Boni, D. Nelson, J. P. Palastro, P. Franke, J. L. Shaw, S. T. Ivancic, A. M. Hansen, D. Turnbull, I. A. Begishev, K. Daub, Z. Barfield, R. K. Follett, D. H. Froula, M. Sherlock, H. P. Le, T. Chapman, and W. Rozmus, "Measurements of Non-Maxwellian Electron Distribution Functions Using Angularly Resolved Thomson Scattering."

J. P. Palastro, P. Franke, M. Lim Pac Chong, K. L. Nguyen, J. Pigeon, D. Ramsey, H. G. Rinderknecht, J. L. Shaw, T. T. Simpson, D. Turnbull, K. Weichman, D. H. Froula, M. Formanek, A. Di Piazza, B. Malaca, M. Pardal, and J. Vieira, "Advanced Radiation Sources Enabled by Spatiotemporal Control of Laser Intensity."

J. L. Peebles, "Magnetized Target Capabilities and Diagnostic Needs at LLE."

H. G. Rinderknecht, J. P. Knauer, W. Theobald, R. Fairbanks, B. Brannon, V. Kobilansky, R. Peck, J. Armstrong, M. Weisbeck, J. Brown, P. B. Radha, S. P. Regan, J. Kunimune, P. Adrian, M. Gatu Johnson, J. A. Frenje, F. H. Séguin, and B. Bachmann, "An Introduction to Knock-on Deuteron Imaging for Diagnosing the Fuel and Hot Spot in Direct-Drive ICF Implosions."

The following presentations were made at the 2021 IEEE Pulsed Power Conference and Symposium on Fusion Engineering, Denver, CO, 12–16 December 2021:

M. Sharpe, W. T. Shmayda, and J. J. Ruby, "Influence of Heat Treatments on the Near-Surface Tritium Concentration Profiles."

W. T. Shmayda, H. Mutha, and K. Ryan, "Tritium Recovery from SPARC."

C. A. Thomas, E. M. Campbell, and M. Tabak, "Review of Inertial Confinement Fusion: Physics and Engineering Challenges" (invited).

The following presentations were made at the American Geophysical Union Fall Meeting, New Orleans, LA, 13–17 December 2021:

M. Ghosh, S. Zhang, and S. X. Hu, "Mechanism of Cooperative Diffusion in bcc Iron Under Earth and Super-Earth's Inner Core Conditions."

R. Paul, K. Nichols, S. Zhang, S. X. Hu, and V. V. Karasiev, "Melting, Acoustic Properties, and Thermal Conditions of FeO_2 Near Core–Mantle Boundary Conditions."

E. M. Campbell, "ICF Research at the University of Rochester's Laboratory for Laser Energetics," presented at the 42nd Annual Meeting of Fusion Power Associates, virtual, 15–16 December 2021.

E. M. Campbell, "University of Rochester and the Laboratory for Laser Energetics: An Overview," presented at the 3rd INFUSE Workshop, virtual, 16–17 December 2021.

R. Betti, "Thermonuclear Ignition in Laser-Driven Inertial Confinement Fusion," presented at the Centro Ricerche Frascati, Frascati, Italy, 17 December 2021.